

DOT/FAA/TC-23/52

Federal Aviation Administration
William J. Hughes Technical Center
Aviation Research Division
Atlantic City International Airport
New Jersey 08405

Experimental Testing to Characterize Plastic Deformation, Dynamic Response, and Ductile Fracture of Inconel 718 Under Various Loading Conditions

September 2023

Final report



U.S. Department of Transportation
Federal Aviation Administration

NOTICE

This document is disseminated under the sponsorship of the U.S. Department of Transportation in the interest of information exchange. The U.S. Government assumes no liability for the contents or use thereof. The U.S. Government does not endorse products or manufacturers. Trade or manufacturers' names appear herein solely because they are considered essential to the objective of this report. The findings and conclusions in this report are those of the author(s) and do not necessarily represent the views of the funding agency. This document does not constitute FAA policy. Consult the FAA sponsoring organization listed on the Technical Documentation page as to its use.

This report is available at the Federal Aviation Administration William J. Hughes Technical Center's Full-Text Technical Reports page: actlibrary.tc.faa.gov in Adobe Acrobat portable document format (PDF).

Form DOT F 1700.7 (8-72)

Reproduction of completed page authorized

1. Report No. DOT/FAA/TC-23/52		2. Government Accession No.		3. Recipient's Catalog No.	
4. Title and Subtitle Experimental Testing to Characterize Plastic Deformation, Dynamic Response, and Ductile Fracture of Inconel 718 Under Various Loading Conditions				5. Report Date September 2023	
				6. Performing Organization Code	
7. Author(s) Aaron Ressa ¹ , Timothy Liutkus ¹ , Jeremy Seidt ¹ , Amos Gilat ¹ , Daniel Cordasco ²				8. Performing Organization Report No.	
9. Performing Organization Name and Address ¹ The Ohio State University, Dynamic Mechanics of Materials Laboratory (DMML) 201 West 19th Ave. Columbus, OH 43210 ² Federal Aviation Administration, William J. Hughes Technical Center Atlantic City International Airport, NJ 08405				10. Work Unit No. (TRAIS)	
				11. Contract or Grant No. 16-G-007	
12. Sponsoring Agency Name and Address Federal Aviation Administration Aircraft Certification Service Policy and Innovation Division 800 Independence Avenue SW Washington, DC 20591				13. Type of Report and Period Covered Final Report	
				14. Sponsoring Agency Code AIR-600	
15. Supplementary Notes The Federal Aviation Administration William J. Hughes Technical Center Aviation Research Division Technical Monitor was Daniel Cordasco.					
16. Abstract A team consisting of Federal Aviation Administration (FAA) Propulsion Research Program, The Ohio State University (OSU), George Mason University (GMU), and the National Aeronautics and Space Administration Glenn Research Center (NASA-GRC) collaborated to develop a new material model in LS-DYNA for impact applications of Inconel 718, a nickel based superalloy used widely for turbine engine hot section blades, disks, cases, and other components. This report details mechanical testing of the plastic deformation and rupture of precipitate hardened Inconel 718. Specimens were tested in tension, compression, and shear under a wide range of strain rates from 10^{-4} s^{-1} to 5000 s^{-1} and temperatures from $23 \text{ }^{\circ}\text{C}$ to $800 \text{ }^{\circ}\text{C}$. Experiments were conducted on five different plate stocks of thickness 1.27 mm, 2.03 mm, 3.17 mm, 6.35 mm, and 12.7 mm. Specimens were cut in different orientations to examine the directional dependence of the material. Dynamic tests were conducted using split Hopkinson bars. Full field strain measurements were made using digital image correlation (DIC) techniques. Ductile fracture was also examined for different stress states induced by subjecting various specimen geometries to different loading conditions. Fracture tests included tension experiments on notched plane stress, plane strain, and axisymmetric specimens as well as combined loading tension-torsion and compression-torsion experiments of tubular specimens and punch tests on flat specimens. The material test plan, experimental setups and procedures, specimen designs, and results are presented and discussed in detail. The Inconel 718 tested exhibits significant strain hardening and strain rate sensitivity as well as a general decrease in strength with increasing temperature.					
17. Key Words Inconel 718, nickel alloy, engine fragment, containment, plastic deformation, strain rate dependency, temperature dependency, dynamic test, digital image correlation			18. Distribution Statement This document is available to the U.S. public through the National Technical Information Service (NTIS), Springfield, Virginia 22161. This document is also available from the Federal Aviation Administration William J. Hughes Technical Center at actlibrary.tc.faa.gov .		
19. Security Classif. (of this report) Unclassified		20. Security Classif. (of this page) Unclassified		21. No. of Pages 156	19. Security Classif. (of this report) Unclassified

Contents

1	Introduction.....	1
1.1	Purpose.....	2
1.2	Background	3
1.3	Literature review of plastic deformation and failure of Inconel 718	4
2	Materials and test plan.....	5
2.1	Materials.....	6
2.2	Plastic deformation test plan	7
2.3	Ductile fracture test plan	12
3	Experimental methods.....	15
3.1	Digital image correlation techniques.....	15
3.2	Plastic deformation specimen design	18
3.2.1	Tension specimen.....	18
3.2.2	Compression specimen	20
3.2.3	Torsion specimen	21
3.3	Low strain rate room temperature test methods	22
3.3.1	Tension at low strain rates	23
3.3.2	Compression at low strain rates	26
3.3.3	Torsion at low strain rates.....	28
3.4	Elevated temperature low strain rate test methods.....	29
3.4.1	Tension at elevated temperatures.....	30
3.4.2	Compression at elevated temperatures.....	32
3.4.3	Torsion at elevated temperatures	33
3.5	High strain rate (Split Hopkinson Bar) test methods	34
3.5.1	Tension at high strain rates	34
3.5.2	Compression at high strain rates	37
3.5.3	Torsion at high strain rates.....	40
3.6	Ductile fracture experimental methods	43

3.6.1	Fracture specimen design.....	44
3.6.2	Combined loading test setup.....	51
3.6.3	Punch experiment setup	53
4	Results and discussion	58
4.1	Strain rate sensitivity test series	59
4.1.1	Tension strain rate sensitivity	59
4.1.2	Compression strain rate sensitivity	61
4.1.3	Torsion strain rate sensitivity.....	63
4.1.4	Comparison of strain rate sensitivity in tension and compression.....	64
4.2	Temperature sensitivity test series	66
4.2.1	Tension temperature sensitivity	66
4.2.2	Compression temperature sensitivity.....	69
4.2.3	Torsion temperature sensitivity.....	70
4.2.4	Comparison of temperature sensitivity in tension and compression	72
4.3	Anisotropy.....	73
4.3.1	Tension anisotropy.....	73
4.3.2	Compression anisotropy.....	74
4.3.3	Comparison of tension and compression anisotropy	75
4.4	Plate thickness experiments	77
4.4.1	Tension experiments for various plate stock thickness.....	77
4.4.2	Compression experiments for various plate stock thickness	80
4.5	Ductile fracture results	82
4.5.1	Plane stress experiments	83
4.5.2	Axisymmetric experiments	84
4.5.3	Plane strain experiments	85
4.5.4	Combined loading experiments	85
4.5.5	Ductile fracture discussion.....	87
4.6	Punch experiments	89

5	Summary and conclusions.....	93
6	References	95
A	Strain rate sensitivity test results.....	A-1
B	Temperature sensitivity test results	B-1
C	Anisotropy test results	C-1
D	Plate thickness test results.....	D-1
E	DIC strain field immediately prior to fracture	E-1

Figures

Figure 1. Tension, compression, and torsion specimen orientations cut from plate P4	11
Figure 2. Fracture test specimens fabricated from plate P4.....	12
Figure 3. 4mm extensometer used for tension. (a) initial length (b) length prior to failure	17
Figure 4. (a) 2mm extensometer (b) platen area data used in compression DIC measurements ..	17
Figure 5. High strain rate tension specimen geometry	19
Figure 6. Low rate tension test specimen geometry	19
Figure 7. Elevated temperature tension test specimen geometry.....	20
Figure 8. Compression specimen geometry.....	20
Figure 9. Torsion specimen geometry	22
Figure 10. Instron 1321 servo-hydraulic biaxial load frame equipped with hydraulic wedge grips	23
Figure 11. Low rate room temperature tension test setup.....	24
Figure 12. Low strain rate tension setup.....	25
Figure 13. Low strain rate compression setup	27
Figure 14. Attachment of torsion specimen to the hydraulic machine	28
Figure 15. High temperature testing experimental setup	29
Figure 16. Close-up of elevated temperature setup	30
Figure 17. Diagram of elevated temperature tension test adapters	30
Figure 18. Tension specimen fixture and high temperature DIC camera setup.....	31
Figure 19. The initial frame of a compression test with the specimen and platen virtual extensometers.....	32
Figure 20. High temperature torsional specimen fixture	33
Figure 21. Initial and final frame of DIC used in torsional test to measure rotation in the section	34
Figure 22. Schematic of tension split-Hopkinson bar.....	35
Figure 23. Initial Y position with the extensometer and failure point (left) and e_1 at the final frame (right)	36
Figure 24. Diagram of split-Hopkinson compression pressure bar	37
Figure 25. Specimen and bar contact setup (left). Camera and light setup (right)	38
Figure 26. (Left) Initial Extensometer and Averaging Box with the Y[mm] coordinate plot and (Right) the final frame with the extensometer and averaging box overlaid on the first principal strain plot	39
Figure 27. Schematic representation of the Kolsky bar at the DMML.....	40
Figure 28. Torsional specimen setup (left). DIC acquisition system setup (right)	42

Figure 29. Initial (left) and final (right) selected DIC measurement points	42
Figure 30. Comparison of strain measurements from wave and DIC at 500s^{-1} and 2000s^{-1}	43
Figure 31. Representative meshes for plane stress (left), plane strain (center), and axisymmetric (right)	44
Figure 32. Meshed geometries with arrows highlighting the location from which data is extracted in fracture specimen design process	45
Figure 33. Necked sample geometry as used in Bridgman's equation (Bridgman, 1964)	48
Figure 34. (Left) Axisymmetric tension and combined loading setup. (Right) Initial combined loading measurement points	51
Figure 35. (Left) Stress ratios vs time and (Right) shear strain rate vs time in combined loading tests	52
Figure 36. Punch geometries. Blunt Punch (0.79mm radius) Sharp Punch (6.35mm radius) Hemispherical Punch (12.17mm radius).....	53
Figure 37. Drawing of punch specimen dimensioned in mm	54
Figure 38. Hemispherical punch test setup in LS-Dyna	54
Figure 39. Triaxiality of the elements plotted at the last time step before failure	55
Figure 40. Quasi static punch fixture and DIC setup.....	56
Figure 41. (Left) Areas of capture for each camera system along with approximate edge of fixture support. (Right) Plot of first principal strain where the failure is shown occurring outside central camera system.....	57
Figure 42. Dynamic punch setup	58
Figure 43. True stress-strain strain rate sensitivity in tension	60
Figure 44. True stress at 5% strain versus strain rate in tension.....	60
Figure 45. Compression stress-strain curves from tests at different strain rates at room temperature	62
Figure 46. Engineering stress versus strain rate at 5% strain for all strain rates tested in compression	62
Figure 47. Shear stress-strain curves from tests at different strain rates at room temperature	63
Figure 48. Shear stress versus log scale strain rate for all the torsion strain rate sensitivity experiments at 2.5%, 7.5%, and 12.5% strain	64
Figure 49. Comparison of rate sensitivity data for tension and compression. True stress at 10% true strain versus strain rate	65
Figure 50. Effective stress versus equivalent plastic strain data for the tension and compression loading conditions at the 1.0 s^{-1} strain rate	65
Figure 51. Stress vs. strain at a strain rate of 0.001 s^{-1} over a range of temperatures.....	66
Figure 52. Tensile stress strain curves at different temperatures at a strain rate of 1 s^{-1}	67

Figure 53. Serrated flow in tension tests at 600°C.....	69
Figure 54. True stress versus true strain for compression specimens for all temperatures conducted at a strain rate of 0.001 s ⁻¹	69
Figure 55. Effective stress versus equivalent strain for torsion experiments at various temperatures and a strain rate of 0.001 s ⁻¹	72
Figure 56. True stress versus true strain curves at each temperature for both the tension (solid line) and compression (dashed line)	73
Figure 57. Stress strain curves from tensile tests at different orientations (strain rate 1 s ⁻¹)	74
Figure 58. Stress strain curves from compression tests at different orientations (strain rate 1 s ⁻¹)	75
Figure 59. Effective stress versus equivalent plastic strain data for specimens with various plate orientations.....	76
Figure 60. Effective stress at 10% equivalent plastic strain and specimen orientation with 95% confidence intervals	77
Figure 61. Representative true stress versus true strain curve for each plate conducted at a strain rate of 0.001 s ⁻¹	78
Figure 62. Representative true stress versus true strain curve for each plate conducted at a strain rate of 500 s ⁻¹	78
Figure 63. Average ultimate stress for each case in tension at both static and dynamic strain rates with error bars representing the 95th% confidence interval	79
Figure 64. True failure strain from 4mm gage section extensometer for each plate at a strain rate of 0.001 s ⁻¹ (Solid Line) and 500s ⁻¹ (Dotted Line).....	80
Figure 65. Representative true stress versus true strain curve for each plate in compression conducted at a strain rate of 0.001 s ⁻¹	81
Figure 66. Representative true stress versus true strain curve for each plate in compression conducted at a strain rate of 500 s ⁻¹	81
Figure 67. True stress at 5% true strain for each plate stock with error bars showing the 95th% confidence interval.....	82
Figure 68. Engineering stress versus engineering strain for plane stress ductile fracture specimens.....	83
Figure 69. Engineering stress versus engineer strain measured from a 4mm extensometer for the various axisymmetric notched specimens.....	84
Figure 70. Engineering stress versus engineering strain for various notched radius plane specimens.....	86
Figure 71. (Top left) Axial force versus displacement for tension-torsion experiments (Top right) Axial force versus displacement for compression-torsion experiments (Bottom left) Torque	

versus rotation for tension-torsion experiments (Bottom right) Torque versus rotation for compression-torsion experiments	87
Figure 72. Equivalent plastic failure strain versus Lode. Lode parameter for each ductile fracture case.	88
Figure 73. Equivalent plastic failure strain versus stress triaxiality for each ductile fracture case.	89
Figure 74. Blunt punch force versus specimen center point displacement for the dynamic (blue) and static (red) experiments	90
Figure 75. Sharp (6.35mm radius) punch force versus specimen center point displacement for the dynamic (blue) and static (red) experiments.....	91
Figure 76. Hemispherical punch force versus specimen center point displacement for the static (red) experiments	91
Figure 77. First principal strain at the failure point versus the punch stroke displacement for the quasi-static -blunt, sharp radius, and hemispherical punch	92

Tables

Table 1. Chemical composition of Inconel 718 plates.....	7
Table 2. Precipitation hardening heat treatment profile.....	7
Table 3. Tension test plan summary	9
Table 4. Compression test plan summary	10
Table 5. Torsion test plan summary.....	11
Table 6. Ductile fracture test series.....	14
Table 7. Compression specimen dimensions, orientation, and strain rate for each plate	21
Table 8. Plane stress fracture specimen geometry, dimensions, triaxiality, and Lode parameter	46
Table 9. Plane strain fracture specimen geometry, dimensions, triaxiality, and Lode parameter	47
Table 10. Axisymmetric fracture specimen geometry, dimensions, triaxiality, and Lode parameter.....	49
Table 11. Combined loading fracture specimen geometry, dimensions, triaxiality, and Lode parameter.....	50
Table 12. Average yield strength, ultimate strength, and failure strain at tested temperatures in tension at a strain rate of 0.001 s^{-1}	67
Table 13. Average true yield strength for all temperatures test in compression at 0.001 s^{-1}	70
Table 14. Average measured material properties at tested temperatures in torsion at 0.001 s^{-1} ...	71
Table 15. Average ultimate stress and failure strain for each axisymmetric notched specimen ..	85

Acronyms

Acronym	Definition
Al2024	Aluminum 2024
ATI	Allegheny Technologies Incorporated
CFR	Code of Federal Regulations
DIC	Digital Image Correlation
DMML	Dynamic Mechanics of Materials Laboratory
EDM	Electrical Discharge Machine
FAA	Federal Aviation Administration
FBO	Fan Blade Out
FE	Finite Element
FPS	Frames Per Second
GRC	Glenn Research Center
ID	Inner Diameter
JC	Johnson-Cook
OD	Outer Diameter
OSU	The Ohio State University
SHB	Split-Hopkinson Bar
Ti64	Titanium-6Aluminum-4Vanadium
NASA	National Aeronautics and Space Administration
QS	Quasi-static
RT	Room Temperature
VSG	Virtual Strain Gage

Executive summary

Fragments released from the failure of high-speed rotating turbine engine parts such as fan blades and disks can seriously threaten aircraft safety if they escape the engine case and strike the airplane. Airframe and engine manufacturers rely on high fidelity dynamic computer simulations performed using explicit finite element (FE) analysis software packages, like LS-DYNA, to model the damage resulting from fragment impacts. Such simulations are crucial to the design of adequate engine debris containment and shielding systems and are often used to aid in meeting FAA blade-out certification tests required for ensuring aviation safety. Accurate modeling and simulation predictions for containment or penetration are highly contingent upon the material model utilized, which dictates the structural deformation, damage, and failure resulting from the impact event.

A team consisting of Federal Aviation Administration (FAA) Propulsion Research Program for Advanced Analysis Methods for Rotor Burst and Blade Release Impacts The Ohio State University (OSU), George Mason University (GMU), and the National Aeronautics and Space Administration Glenn Research Center (NASA-GRC) collaborated to develop a new material model in LS-DYNA for impact applications of Inconel 718, a nickel based superalloy used widely for turbine engine hot section blades, disks, cases, and other components.

This report details mechanical testing of the plastic deformation and rupture of precipitate hardened Inconel 718. Specimens were tested in tension, compression, and shear experiments under a wide range of strain rates from 10^{-4} s^{-1} to 5000 s^{-1} and temperatures from $23 \text{ }^{\circ}\text{C}$ to $800 \text{ }^{\circ}\text{C}$. Experiments were conducted on five different plate stocks of thickness 1.27 mm, 2.03 mm, 3.17 mm, 6.35 mm, and 12.7 mm. Specimens were cut from different orientations to examine the directional dependence of the material. Dynamic tests were conducted using split Hopkinson bars and full field strain measurements were made using digital image correlation (DIC) techniques. Ductile fracture was also examined for different stress states induced by subjecting various specimen geometries to different loading conditions. Fracture tests included tension experiments on notched plane stress, plane strain, and axisymmetric specimens as well as combined loading tension-torsion and compression-torsion experiments of tubular specimens and punch tests on flat specimens. The material test plan, experimental setups and procedures, specimen designs, and results are presented and discussed in detail. The Inconel 718 tested exhibits significant strain hardening and strain rate sensitivity as well as a general decrease in strength with increasing temperature in all modes of loading.

Acknowledgments

This research was funded by the Federal Aviation Administration under grant 16-G-007. The work was completed at The Ohio State University (OSU) Dynamic Mechanics of Materials Laboratory (DMML) by Timothy Liutkus and Aaron Ressa under the direction of Professors Amos Gilat and Jeremy Seidt. Thank you to Bill Emmerling for his leadership as the FAA program manager on this task and to Mike Pereira, Duane Revilock, and Charles Ruggeri, of the National Aeronautics and Space Administration Glenn Research Center (NASA GRC) for conducting impact testing on Inconel 718 panels. Thanks also to Steve Kan, Paul Dubois, Kelly Carney, and Stefano Dolci of George Mason University for material model development.

1 Introduction

Inconel 718 is a nickel superalloy commonly used in the hot section of aircraft turbine engines due to its retention of mechanical strength at high temperatures, high resistance to corrosion, and processability. Several engine manufactures utilize Inconel 718 for high-pressure turbine blades, disks, aft engine casings and frames, and other structural engine parts exposed to high temperatures (Paulonis & Schirra, 2001; Schafrik, Ward, & Groh, 2001). When a rotating engine component such as a blade or disk fails, the resulting debris can impact the engine case, and if penetrated, potentially other parts of the aircraft. Numerical simulations are widely used by industry to create shielding designs capable of containing fragments in these rare but serious events. Computational models also play an important role in meeting FAA certification requirements for aircraft safety including engine fan blade out (FBO) containment and engine fragment impact hazard-mitigation. However, one of the significant difficulties in developing models, which can accurately simulate engine fragment impact and penetration, is sufficient mechanical test data necessary to characterize the dynamic material response and fracture.

Finite element (FE) analysis has become an essential tool in computational solid mechanics for the aerospace industry to evaluate complex structural designs. The explicit FE software, LS-DYNA, is often used to simulate dynamic aircraft applications such as crash, bird strike, and FBO. In addition to providing engineers a cost effective way for evaluating different materials and system designs during the product development and design phases, analysis is also now being used at least in part for certification of new and derivative aircraft and engines. Simulations allow engineers to analyze a multitude of conditions, which would be impossible to test in their entirety, for example, various blade release points, and provide insight into quantities of interest like plastic strain evolution, which can be difficult to measure in full-scale physical tests.

FBO tests required for engine certification under CFR 33.94 (2023) involve the demonstration that an engine can contain damage after release of the most critical blade at maximum rpm. These tests, which culminate certification in destruction of a physical engine, occur only after many lower level system and component tests and simulations are successfully accomplished at tremendous expense. While traditional aircraft mechanical design can involve complex geometry, multiple materials, and complex boundary conditions, it is mainly focused on a structure's elastic behavior as this is the intended application domain. FBO applications however, require a more complete understanding of the material plastic deformation, damage accumulation, and fracture as these structures must be capable of absorbing significant energy beyond yield. FBO events take place on a very fast timescale, resulting in impacts that create

high strain rates and temperatures in the target material. Furthermore, engine debris released from a fractured blade or disk can vary widely in size and velocity with many possible different relative orientations to the impacted structure, which also can vary in geometry and thickness depending upon impact location. This combination of factors strongly influence whether fragments will be contained or penetrate and can result in a multitude of different failure modes such as petaling, plugging, ductile hole growth, brittle fracture, and spall fragmentation.

Accurately simulating FBO events and ensuring robust designs capable of containing fragments necessitates the use of advanced material models. Such models must take into account how plastic deformation, damage, and failure is affected by influences such as strain rate, temperature, and stress state, which result from the inherently dynamic nature and complex loading conditions of an impact event. The ability of the material model to capture these phenomena for a variety of possible conditions has a significant influence on simulation predictions for the severity of impact damage and ultimately, if fragments are contained, or if an engine or airframe structure is penetrated. Therefore, experimental data derived from specimen tests at the strain rates, temperatures, and stress states experienced in the actual application is critical for accurate model predictions.

1.1 Purpose

The research presented herein is part of a project to develop and calibrate material model input parameters in the commercial explicit FE code, LS-DYNA, based on mechanical specimen tests. The plastic deformation and fracture of Inconel 718 plate is investigated by conducting tension, compression, and shear tests. The testing results in the form of stress strain curves provide the means for studying the following topics:

- Strain rate sensitivity of the material, from testing at different strain rates at the same constant ambient room temperature
- Temperature sensitivity of the material, from testing at the same (quasi-static) strain rate at different temperatures
- Anisotropic plastic properties from testing specimens machined in different orientations
- Difference in the properties of plates with different thicknesses from testing five plate thicknesses
- Failure strain dependence on the state of stress as obtained from different specimen geometries and loading configurations

1.2 Background

The specimen test data for Inconel 718 from this test program will be used for input into a material model MAT_224 in LS-DYNA (Ansys, 2021). As part of a previous effort, a family of material models was developed and integrated into LS-DYNA based on the Johnson-Cook (JC) model (Johnson & Cook, 1983; Johnson & Cook, 1985). The material model MAT_224 or *MAT_TABULATED_JOHNSON_COOK is detailed in previously published FAA reports (Buyuk, 2014). JC models are widely used to simulate impact problems and utilize a phenomenological approach to material plasticity and fracture accounting for strain rate sensitivity and temperature dependence. The constitutive model defines the effective material flow stress $\bar{\sigma}$ as shown in Equation 1, where ε_p is the equivalent plastic strain, $\dot{\varepsilon}$ is the instantaneous strain rate, $\dot{\varepsilon}_0$ is the reference strain rate. T is the instantaneous temperature, T_r is the reference temperature, and T_m is the melting temperature of the material.

$$\bar{\sigma} = [A + B\varepsilon_p^n] \left[1 + C \ln \left(\frac{\dot{\varepsilon}}{\dot{\varepsilon}_0} \right) \right] \left[1 - \left(\frac{T - T_r}{T_m - T_r} \right)^m \right] \quad 1$$

$A, B, C, n,$ and m are parameters determined through fitting curves to experimental test data. The constants A, B, n are found from a baseline test performed at the reference strain rate and temperature. C is found from data taken at various strain rates, while the m term is found from data at various temperatures. The equivalent strain at fracture of the material is given by Equation 2 where σ^* is stress triaxiality and $D_1, D_2, D_3, D_4,$ and D_5 are fracture parameters determined experimentally.

$$\varepsilon_f = [D_1 + D_2 D_3 \sigma^*] \left[1 + D_4 \ln \left(\frac{\dot{\varepsilon}}{\dot{\varepsilon}_0} \right) \right] \left[1 + D_5 \left(\frac{T - T_r}{T_m - T_r} \right) \right] \quad 2$$

D_1, D_2, D_3 are found experimentally by performing fracture experiments at various triaxialities obtained by different specimen geometries and loading conditions. D_4 is found by testing at various strain rates of a single triaxiality while D_5 is determined with tests at different temperatures.

The fracture component of the model uses a cumulative parameter, D , to define the damage of each element as in Equation 3 where $\Delta\varepsilon_p$ is the increment of equivalent plastic strain and ε_f is equivalent strain to failure. The element is deleted when D reaches unity.

$$D = \sum \frac{\Delta\varepsilon_p}{\varepsilon_f} \quad 3$$

The material test data set for Inconel 718 detailed in this report is intended to construct a MAT_224 tabulated material parameter input deck in LS-DYNA to include stress-strain curves at different strain rates and temperatures as well as a tabulated failure locus. MAT_224 offers greater versatility than the analytical Johnson-Cook and other plasticity models because it uses tabulated stress strain curves at various strain rates and temperatures, which are obtained from the experimental specimen test data. Stress state dependence is incorporated by tabulating a fracture locus consisting of an equivalent plastic strain failure criterion dependent on both the stress triaxiality and Lode parameter. The material models are ultimately validated by simulating impact tests performed at NASA GRC in which flat Inconel 718 panels were impacted by projectiles fired from a gas gun. The panel impact test results are summarized in a previously published report (Pereira, Revilock, & Ruggeri, 2020). A report detailing the material model development is forthcoming.

1.3 Literature review of plastic deformation and failure of Inconel 718

The mechanical behavior of Inconel 718 has been studied over a wide range of temperatures and strain rates. A significant amount of research has been conducted on machining and fabrication techniques. Ezugwu (2005) studied the history and difficulties in the manufacturing of Inconel 718 components and summarized the recent developments to increase manufacturability and reduce costs. Jafarian et al. (2014) calibrated an Inconel 718 Johnson-Cook FE model in order to simulate and study machining parameters. An important component of Inconel models includes strain rate effects. Kobayashi (2008) looked at plastic deformation in shear at strain rates between 0.01 s^{-1} and 3000 s^{-1} on a quasi-static load frame and torsional split Hopkinson bar in order to determine Johnson-Cook parameters. Pereira & Lerch (2001) studied ballistic impact responses of Inconel 718 plates with a projectile in the annealed and aged condition. Sciuva et al. (2003) looked at the structural response of Inconel 718 cast plates during a penetration event and created a ballistic limit curve from empirical correlation. DaMange et al. (2009) explored the effects of heat treatments in both the annealed and hardened forms with dynamic penetration experiments and developed a thermo-elastic-visco-plastic finite element model. Thomas et al. (2006) examined the aging characteristics and their effects on softening and deformation behavior. Zhang et al (2004) developed a set of constitutive equations based on a hyperbolic sine relation to represent the relationship between stress, strain, and strain rate over a wide range of strain. Xue et al. (2003) studied the superplastic behavior of Inconel 718 in tensile tests at $1000 \text{ }^{\circ}\text{C}$ and strain rate of 0.0001 s^{-1} in the context of forming operations for component fabrication. Zhou (1994) studied the effect of a wider strain rate range from 0.1 s^{-1} to 0.001 s^{-1} in compression, in a temperature range from $950 \text{ }^{\circ}\text{C}$ to $1100 \text{ }^{\circ}\text{C}$. Zhang et al (2011) examined high

temperature plasticity and micro void coalescence ductile fracture mechanisms in tension of Inconel 718. Jerky flow of Inconel 718 has been observed by many researchers at elevated temperatures including Chen & Chaturvedi (1997) who studied the serrated flow of aged Inconel 718 in the temperature range 200 °C to 575 °C, at strain rates between 0.01 s⁻¹ and 0.000005 s⁻¹. Prasad et al (2010) observed the effect in tensile tests of a forged disc at 650 °C in the strain rate regime between 0.01 s⁻¹ and 0.0001 s⁻¹. Garat et al (2008) conducted tensile tests on Inconel 718 between temperatures of 400 °C to 750 °C and concluded the Portevin-Le Chatelier effect produces instabilities of type C in the plastic flow and can affect crack propagation.

Characterization of ductile fracture in a material is an important component of producing a model to predict failure. Bao & Wierzbicki (2004) created a fracture locus based on triaxiality and equivalent strain for 2024-T351 through a series of tension, shear, and compression tests. However, Barsoum & Faleskog (2007) conducted combined tension and torsion on notched tubes and found that both stress triaxiality and the Lode parameter had a strong influence on ductile fracture. Xue (2007) created a phenomenological damage based plasticity model based on the stress triaxiality and Lode parameter.

Punch tests have also been shown to provide insight into the ductility and failure of a material. Guduru et al (2005) used a shear punch test to evaluate the yield and ultimate tensile strengths in different materials, and found good correlation between the material properties and shear punch test results. Dowling et al (1970) examined the effect of punch velocity on the energy to failure and ductility. Dabboussi & Nemes (2005) used a punch test at different velocities to establish ductile fracture criteria. Punch tests have also been shown to be valuable in validation of numerical models. Goijaerts et al (2001) examined energy based ductile fracture models in punch by correlating experimental resulting to finite element simulations.

2 Materials and test plan

The overall objective of the test plan is to characterize the plasticity and fracture properties of Inconel 718 through specimen test experiments. With regard to plasticity properties, the emphasis is on the effect of strain rate and temperature on the stress-strain response. Variation in the stress-strain response is measured for five different plate thicknesses. Additionally, for the thickest plate, anisotropy is investigated as well as a substantial fracture series designed to obtain failure strains over a broad region of stress states. The experimental methods are detailed in Section 3.

The effects of strain rate are investigated by conducting uniaxial tensile, compression, and torsion tests at room temperature over a wide range of strain rates from 0.0001 s⁻¹ to 5000 s⁻¹.

The effects of temperature are investigated from tensile, compression and torsion test series done at strain rate of 0.001 s^{-1} and 1 s^{-1} and various temperatures ranging from room temperature (RT) to $800 \text{ }^{\circ}\text{C}$. Tension and compression tests are performed at 0.001 s^{-1} and 500 s^{-1} for each of the five different plate thicknesses. Anisotropic plasticity properties are investigated for the thickest plate by conducting tensile and compression tests with specimens machined in directions 0° , $\pm 45^{\circ}$, and 90° from the rolling direction and through the thickness in compression. The fracture properties are determined from tensile tests of notched specimens (including plane stress, plane strain, and axisymmetric geometries), combined loading in tension-torsion and compression-torsion of hollow cylindrical specimens, as well as a series of punch tests on flat specimens.

Details of the material tested are presented in Section 2.1. A summary of the plasticity test plan for all tension, compression, and shear tests used for investigating the strain rate and temperature effects is presented in Section 2.2. The test plan used for investigating the fracture properties is presented in Section 2.3.

2.1 Materials

The mechanical properties of Inconel 718 plates with thicknesses of 12.7 mm (Plate P4), 6.35 mm (Plate P3), 3.175 mm (Plate P2), 2.032 mm (Plate P1), and 1.27 mm (Plate P5) are investigated. The plates were purchased from Allegheny Technologies Incorporated (ATI) in the annealed condition. Material certification sheets are provided in Appendix 1)a)i)(1)(a)A of the impact validation tests report DOT/FAA/TC-19/40, NASA/TM-2020-220451 (Pereira, Revilock, & Ruggeri, 2020). It should be noted that there are several manufacturers with different trade names for Inconel 718; ATI refers to this as ATI 718 Alloy in the certification sheets, but the term Inconel 718 is used in this report for consistency with other related reports and common name recognition. Table 1 summarizes the chemical composition of the plates, which varies slightly for each thickness. The plates in each thickness were from the same mill run.

Table 1. Chemical composition of Inconel 718 plates

	12.7 mm / Plate P4	6.35 mm / Plate P3	3.18 mm / Plate P2	2.03 mm/ Plate P1	1.27 mm / Plate P5
C	0.048	0.53	0.05	0.05	0.05
Mn	0.083	0.21	0.07	0.12	0.08
P	0.008	< 0.005	0.007	0.008	0.006
S	0.0001	< 0.002	0.0002	0.0001	0.0002
Si	0.072	0.08	0.06	0.07	0.05
Ni	52.60	52.90	52.20	52.54	52.79
Cr	18.32	18.1	18.27	18.21	18.18
Mo	2.87	3.09	2.89	2.90	2.88
Co	0.20	0.27	0.16	0.30	0.16
Cu	0.034	0.05	0.04	0.06	0.03
Al	0.54	0.53	0.59	0.55	0.6
Ti	1.02	0.92	1.02	1.00	1.02
Cb	4.94	5.17	5.04	5.00	4.96
B	0.0029	0.003	0.002	0.002	0.001
Fe	19.25	18.9	19.62	19.05	19.13
Ta	0.01	< 0.05	0.01	0.01	0.01

The plates were then precipitation hardened using the heat treatment profile described in Table 2. The precipitation hardening heat treatment resulted in a Rockwell hardness of HRC 44 as noted in the certification sheet found in Appendix B of DOT/FAA/TC-19/40, NASA/TM-2020-220451 (Pereira, Revilock, & Ruggeri, 2020).

Table 2. Precipitation hardening heat treatment profile

Phase	Duration (hours)	Description
1 – Temp Hold	8	Hold temperature at 718°C
2 – Ramp Cool	1.75	Ramp cool at 55°C per hour
3 – Temp Hold	8	Hold temperature at 621°C

2.2 Plastic deformation test plan

The mechanical behavior of the precipitation hardened Inconel 718 is investigated through a series of tension, compression, and torsion experiments. These tests are summarized in Table 3, Table 4, and Table 5, and are used to determine the effects of strain rate and temperature on the

material plasticity. All strain rate and temperature sensitivity experiments are performed on Plate P4 (the thickest plate) with specimens oriented in the rolling direction.

Strain rate sensitivity is assessed with a series of tension, compression, and torsion tests at room temperature. Tension tests are performed at strain rates ranging from 0.0001 s^{-1} to 2000 s^{-1} . Compression tests are performed at strain rates ranging from 0.0001 s^{-1} to 5000 s^{-1} . Shear tests are performed at strain rates ranging from 0.0001 s^{-1} to 5000 s^{-1} . Tests at nominal strain rates of 1 s^{-1} and below are performed on a hydraulic load frame while dynamic tests at strain rates of 500 s^{-1} and higher are conducted with a split-Hopkinson bar (SHB).

Temperature sensitivity is assessed with a series of tension, compression, and torsion tests at a quasi-static strain rate of 0.001 s^{-1} . Tests are performed at room temperature and four elevated temperatures: $200 \text{ }^{\circ}\text{C}$, $400 \text{ }^{\circ}\text{C}$, $600 \text{ }^{\circ}\text{C}$, and $800 \text{ }^{\circ}\text{C}$. Tests at 1 s^{-1} are also conducted in tension at room temperature and the four elevated temperatures.

Plate P4 anisotropy is investigated with tension and compression tests conducted at a strain rate of 1 s^{-1} on specimens fabricated in four orientations: the rolling direction, $+45^{\circ}$ from the rolling direction, transverse to the rolling direction, and -45° from the rolling direction. Compression tests are also performed in the through thickness direction.

The effect of plate thickness is tested by conducting tension and compression tests at a strain rate of 1 s^{-1} and room temperature on plates P1, P2, P3, and P4. Tension tests are also performed on plate P5, which is too thin to test in compression.

Table 3. Tension test plan summary

Loading Mode	Testing Fixture	Strain Rate (1/s)	Temperature (°C)	Specimen Orientation	Plate Stock
Tension	Hydraulic Load Frame	0.0001	RT	Rolling	P4
		0.001	RT		P1, P2, P3, P4, P5
			200		P4
			400		
			600		
			800		
		1	RT	Rolling	P4
				+45°	
				Transverse	
				-45°	
	1	RT	200	Rolling	P4
			400		
			600		
			800		
			800		
Tension SHB	Tension SHB	500	RT	Rolling	P1, P2, P3, P4, P5
		2000	RT		P4

Table 4. Compression test plan summary

Loading Mode	Testing Fixture	Strain Rate (1/s)	Temperature (°C)	Specimen Orientation	Plate Stock			
Compression	Hydraulic Load Frame	0.0001	RT	Rolling	P4			
		0.001	RT	Rolling	P1, P2, P3, P4			
			200					
			400					
			600					
			800					
		0.01	RT	Rolling	P4			
		1	RT	Rolling	P4			
				+45°				
				Transverse				
	-45°							
	Through Thickness							
					Compression SHB	500	Rolling	P1, P2, P3, P4
						1000		
						2000		
5000								

Table 5. Torsion test plan summary

Loading Mode	Testing Fixture	Strain Rate (1/s)	Temperature (°C)	Specimen Orientation	Plate Stock
Torsion	Hydraulic Load Frame	0.0001		Rolling	P4
		0.001	RT		
			200		
			400		
			600		
	800				
	0.01	RT			
	1				
	Torsion SHB		500		
			2000		

Figure 1 illustrates the quasi-static tension and compression specimen orientations used to test the anisotropic properties of plate P4.

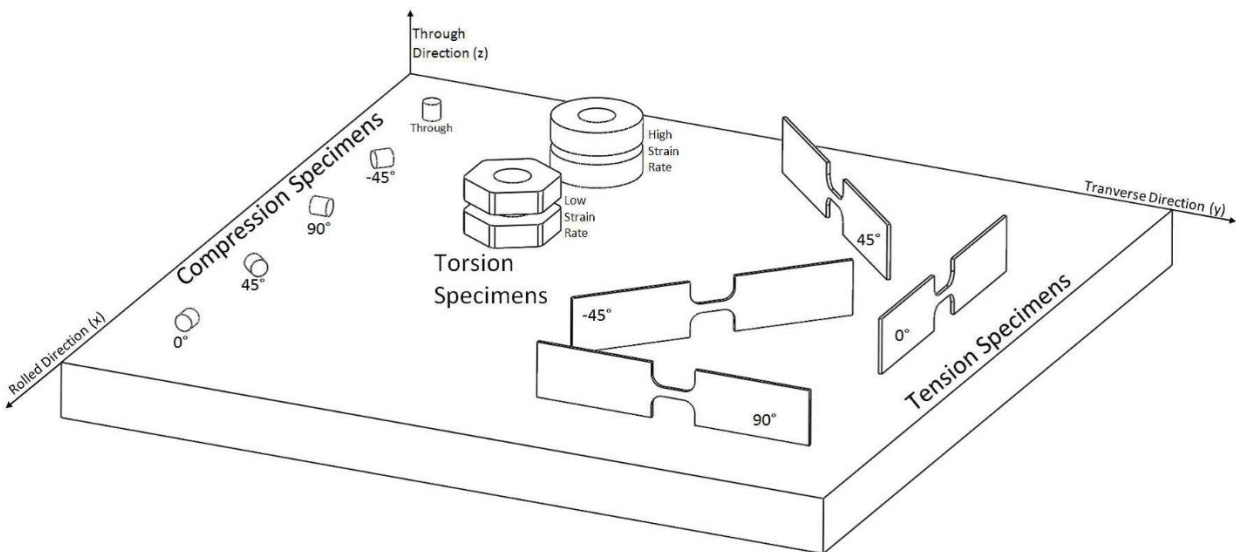


Figure 1. Tension, compression, and torsion specimen orientations cut from plate P4

2.3 Ductile fracture test plan

In addition to experiments characterizing the strain rate and temperature plasticity of precipitate hardened Inconel 718, this work also investigates ductile fracture of the material under a broad range of stress states. All specimens in the fracture series are cut from P4. Fracture specimens are designed with different geometries to produce a variety of stress states defined by the triaxiality, σ^* , and Lode parameter, θ_L . All tension and combined loading specimens were fabricated so the direction of loading was parallel to the rolled direction of the plate as shown in Figure 2.

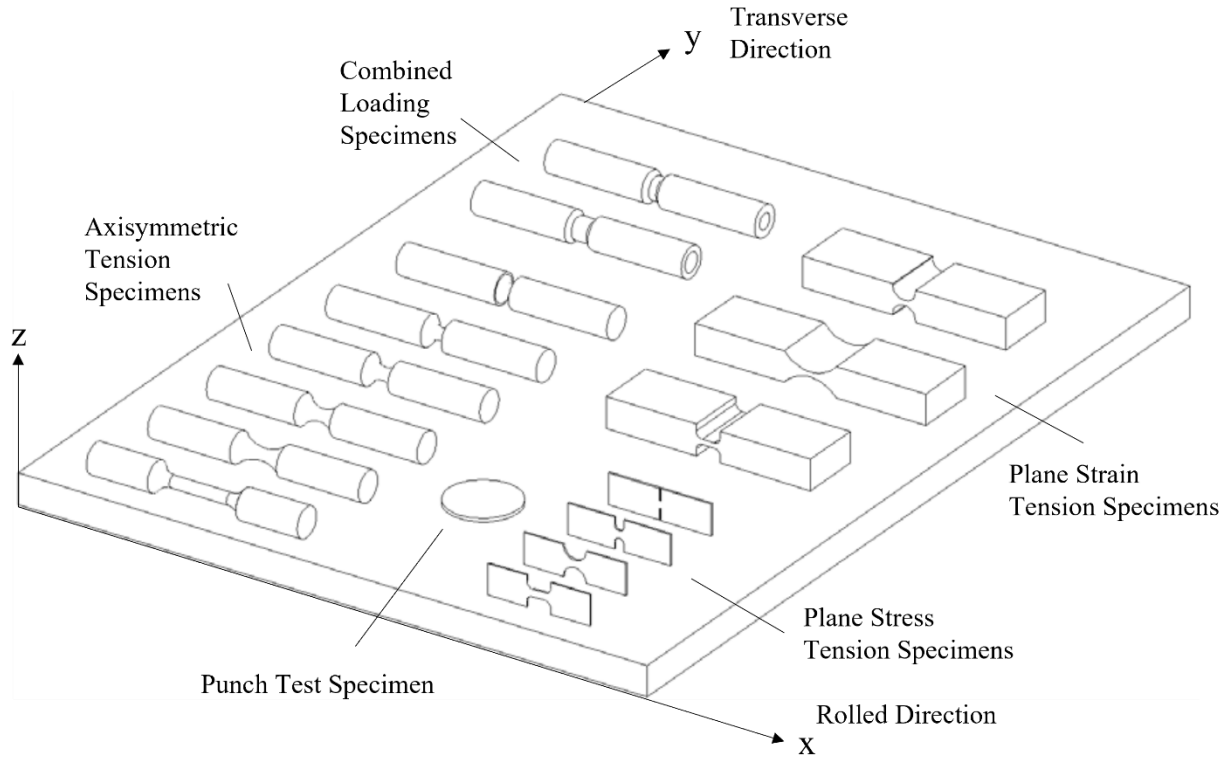


Figure 2. Fracture test specimens fabricated from plate P4

The stress triaxiality (σ^*) is defined in Equation 4 as:

$$\sigma^* = \sigma_m / \bar{\sigma} \quad 4$$

where σ_m is the mean stress defined by Equation 5 and $\bar{\sigma}$ is the von Mises stress defined by Equation 6.

$$\sigma_m = \frac{1}{3} \sigma_{kk} = \frac{1}{3} (\sigma_1 + \sigma_2 + \sigma_3) \quad 5$$

The principal strains, $\sigma_1, \sigma_2, \sigma_3$ are defined such that $\sigma_1 \geq \sigma_2 \geq \sigma_3$.

$$\bar{\sigma} = \left(\frac{3}{2} S_{ij} S_{ij} \right)^{\frac{1}{2}} \quad 6$$

The deviatoric stress tensor, S_{ij} , is defined as shown in Equation 7 σ_{ij} denotes the stress tensor components and δ_{ij} is the Kronecker delta.

$$S_{ij} = \sigma_{ij} - \sigma_m \delta_{ij} \quad 7$$

Note that this conventional definition of triaxiality with positive values corresponding to tension and negative values corresponding to compression is the opposite sign convention of the triaxiality definition used in LS-DYNA. As mentioned, Barsoum and Faleskog (2007) found that in stress triaxiality alone was insufficient to describe material fracture behavior over the entire range of potential stress states. Therefore, an additional parameter, the Lode parameter θ_L must be introduced as defined in Equation 8, where $J_3 = S_1 S_2 S_3$ is the third invariant of the deviatoric stress tensor, and S_1, S_2 and S_3 are the principal deviatoric stresses.

$$\theta_L = \frac{27 J_3}{2 \bar{\sigma}^3} \quad 8$$

Ultimate fracture of the material is then fully quantified by the equivalent plastic failure strain $\bar{\epsilon}_f^p$ as a function of σ^* and θ_L defined in Equation 9.

$$\bar{\epsilon}_f^p = f(\sigma^*, \theta_L) \quad 9$$

Additional details on the definition and characteristics of the triaxiality and Lode parameter are given in Carney et al (2020) and Seidt (2014).

The fracture test series consists of tension tests, combined tension/torsion and compression/torsion loading, and punch tests. The tension tests are performed on notched plane stress, plane strain, and axisymmetric specimens. The combined loading tests are performed on hollow cylindrical specimens. Punch tests are performed on thin specimens at quasi-static and dynamic rates. All specimens in the fracture test series are fabricated from Plate P4 as shown in Figure 2. The Inconel 718 fracture specimens were designed by Liutkus (2014) and Ressa (2015) and developed based on previous work at the OSU DMML on Titanium-6Aluminum-4Vanadium (Ti64) by Hammer (2014) and Aluminum 2024-T351 (Al 2024) by Seidt (2014). The fracture

series specimens were designed using LS-DYNA to obtain failure strain data at the σ^* and θ_L values shown in Table 6.

Table 6. Ductile fracture test series

Test No.	σ^*	θ_L
Plane Stress Series		
SG1	0.355	0.943
SG2	0.405	0.753
SG3	0.476	0.533
SG4	0.574	0.603
Axisymmetric Series		
SG5	0.378	1.0
SG6	0.492	1.0
SG7	0.562	1.0
SG8	0.651	1.0
SG9	0.768	1.0
SG10	0.942	1.0
Plane Strain Series		
SG11	0.585	0.0635
SG12	0.662	0.0464
SG13	0.761	0.0293
Combined Loading Series		
LR1	0.251	0.702
LR2	0.147	0.39
LR3	0.000	0
LR4	-0.147	-0.39
LR5	-0.233	-0.55
Punch Series		
TMP1	-	-
TMP4	-	-
TMP6	-	-

3 Experimental methods

The experimental methods used to test both the plastic deformation and ductile fracture behavior of Inconel 718 are presented in this section. The plastic deformation experimental program consists of tension, compression, and torsion (pure shear) tests, at various strain rates ranging from nominal values of 0.0001 s^{-1} to 5000 s^{-1} and various temperatures ranging from room temperature to $800 \text{ }^{\circ}\text{C}$. Plasticity characterization specimens are designed to have the same gage section for all strain rates and temperatures for a given loading mode. The ductile fracture experimental program consists of several test series including: tensile tests with flat (plane stress) and round (axisymmetric) specimens with various notched geometries, tensile tests with wide (plane strain) specimens with various notched geometries, combined loading (axial-torsional) tests, and punch tests of flat specimens with various punch geometries.

3.1 Digital image correlation techniques

Strain measurements are obtained by using 3D digital image correlation (DIC). DIC is an optical measurement technique that allows for full field displacement (and therefore strain) measurements on the surface of a specimen. Deformation is tracked through the evolution of a random contrast pattern applied to a specimen's surface. DIC techniques are described in detail by Sutton et al (2009) as well as in previous testing done for this program with Ti64 (Hammer, 2014) and Al2024 (Seidt, 2014).

An advantage of using DIC is that surface displacement measurements can be made on the fixture grips or platens as well as the specimen shoulder regions and entire gage section. This eliminates errors in using the crosshead displacement data due to test fixture compliance or slip and thus provides the most accurate boundary condition measurements. Full field DIC measurements also provide advantages over physical extensometers in accurately measuring post-yield plastic deformation necessary for calculating true strains. DIC is also essential in obtaining fracture data by tracking the strain evolution of all points on the specimen surface allowing data extraction at the point of failure, which would not be always possible with strain gages since this location is not known before the test.

The 3D DIC system employed consists of two cameras that provide a stereographic view of the specimen, data acquisition software that provides time synchronized images, and the 3D DIC commercial image processing software VIC-3D (Correlated Solutions Inc., 2014). 3D-DIC measurements are completed by first calibrating the system, recording and processing an experiment, and then using post-processing techniques to extract the desired data. The camera setup involves two cameras in a synchronized stereographic configuration that take images at the

same time instants throughout a test. The cameras are set up 10-20 degrees apart such that the focal length of each cameras is equidistant from the specimen. Additional lighting is provided so that the lenses can be set to a high aperture setting. This produces a large focused field depth range. The DIC system is calibrated by taking multiple photographs of a panel with known grid spacing in various orientations. These calibration images are taken using both cameras and are then analyzed using the VIC-3D software to determine the position of the cameras relative to each other and determine a spatial coordinate system.

After the DIC system is calibrated, images of the specimen deformation can be recorded during the test. A random speckle pattern is applied to the specimen using black and white spray paint. The pattern is typically applied with household spray paint. The DIC software analyzes each pair of images from the two cameras by first discretizing the image into $n \times n$ pixel subsets defined by the user. The deformation is calculated for every n^{th} pixel, known as the step. The first image becomes the reference. The VIC-3D software tracks the displacement of each pixel subset by referencing to their locations in the initial image. Strains are calculated from these displacements using one of several available definitions of the strain tensor in VIC-3D. In this case, the Hencky strain tensor is used.

For each test, a virtual strain gage (VSG) length is calculated which is a product of the pixel length, step size, and strain filter. The pixel length is dependent on the camera setup and lenses used. The step size and strain filter are changed accordingly to maintain the same VSG length for all tests. The VSG is also used in determining the element size in numerical simulations, which are compared to the experimental results. A VSG length of between 0.15 mm and 0.20 mm was established to accurately resolve areas of highly localized deformation as in the necking region of tensile specimens. VIC-3D gives the user a variety of post-processing inspection options, such as data from a single point, a virtual extensometer, or data averaged within a box. Single point data is useful for understanding the evolution of the strain at the location of specimen fracture. Virtual extensometers are used to determine engineering strain and these data can be compared to data generated using traditional measurement techniques like mechanical extensometers and strain gages. Averaged data in a given area can be extracted as well including five strain components ϵ_{xx} , ϵ_{yy} , ϵ_{xy} , ϵ_1 , ϵ_2 and three displacement measurements – x-displacement (u), y-displacement (v), and z-displacement (w).

All tension tests presented utilize DIC measurements for strain data. A 4 mm virtual extensometer is used over the gage section of the tension specimen. Figure 3 provides an example showing the initial extensometer length before deformation has taken place and extensometer length at the moment before specimen failure.

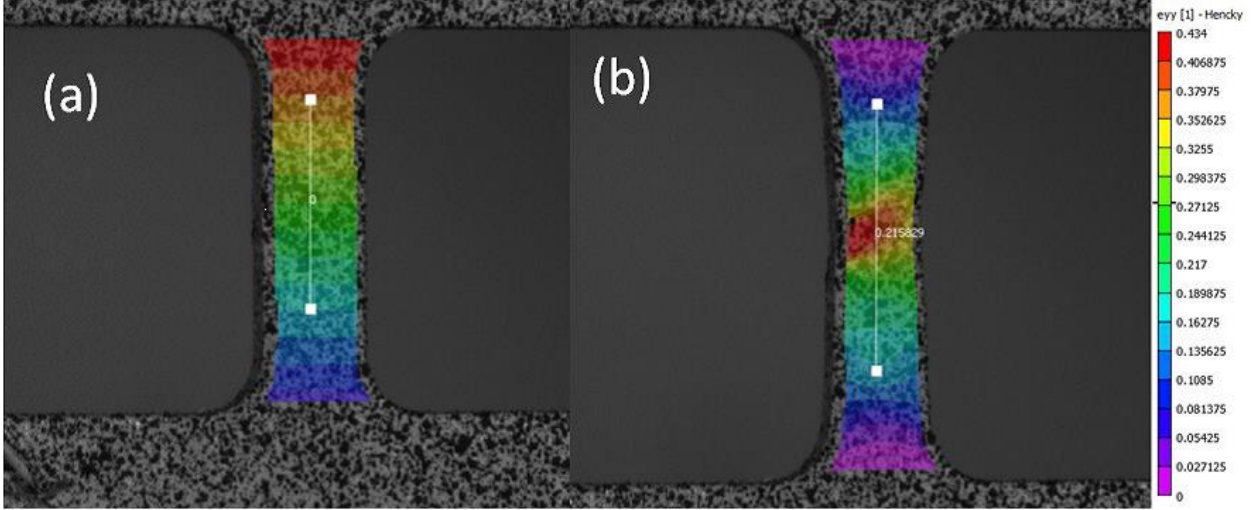


Figure 3. 4mm extensometer used for tension. (a) initial length (b) length prior to failure

All compression tests, except those completed at nominal strain rates of 1000 s^{-1} and higher on the compression SHB, are presented with DIC strain measurements. DIC data are collected using a combination from a 2 mm virtual extensometer over the specimen surface and the relative displacements of the platens. The elastic deformation is collected from the extensometer, and deformation after yield is calculated from the relative platen motion. Strain is calculated from the platen motion. Platen data is used because a barreling of the compression specimen occurs. This phenomenon arises due to friction at the sample/platen interface, resulting in surface strains that are not representative of the strain in the center of the specimen. The 2 mm extensometer and the selected platen areas are shown in Figure 4.

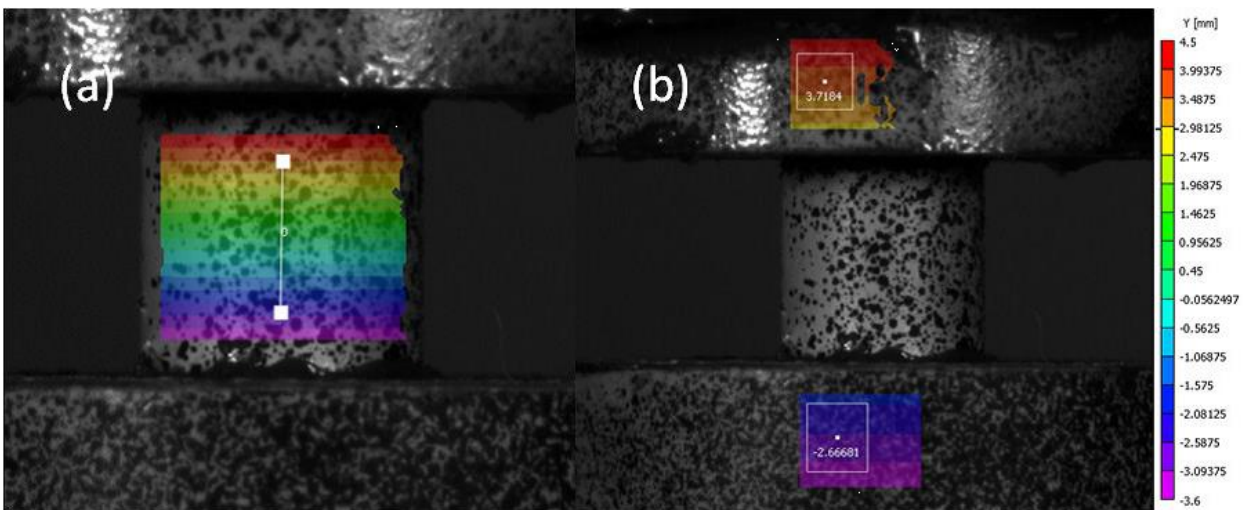


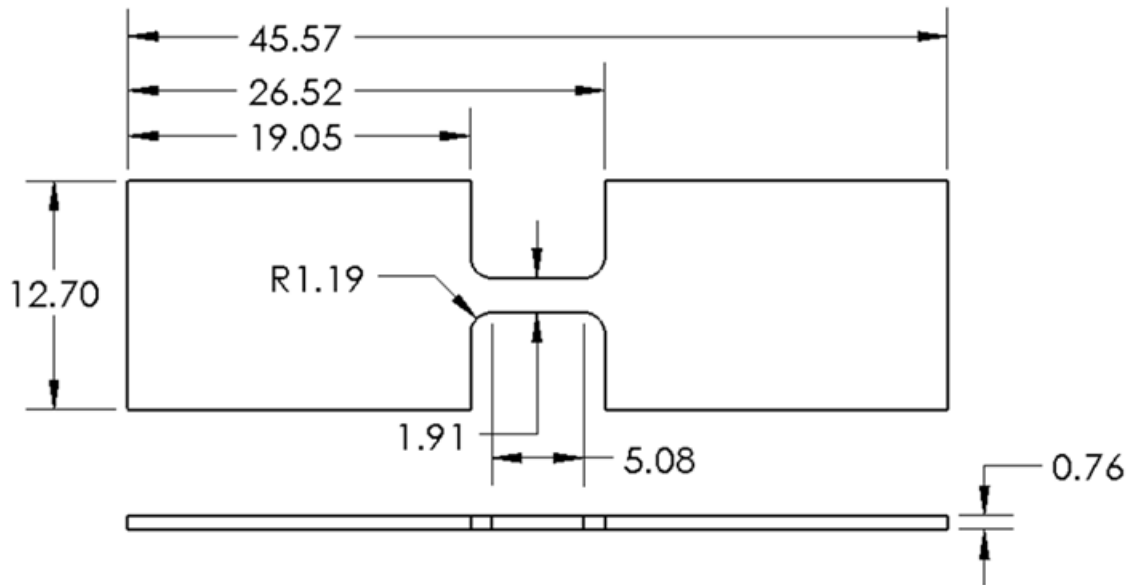
Figure 4. (a) 2mm extensometer (b) platen area data used in compression DIC measurements

3.2 Plastic deformation specimen design

Tension, compression, and torsion specimens were fabricated from the Inconel 718 plates shown in Table 1 to characterize the material's plastic deformation over the intended strain rates and temperatures. Tension specimens with flat dogbone geometries were machined from all five different thickness plates and cylindrical compression specimens were cut from plates P1, P2, P3, and P4. Torsion spool specimens with a thin-walled tube gage section were cut from only the thickest plate, P4. All specimen geometries were consistent throughout the plastic deformation test program to eliminate geometric effects skewing the overall interpretation of the data. Fracture test specimens used to characterize the ductile failure of P4 as a function of stress state are detailed in Section 3.6.

3.2.1 Tension specimen

Thin dog-bone shaped specimens are used in the tension experiments used to characterize the strain rate and temperature dependent plastic deformation and failure of precipitation hardened Inconel 718. The high strain rate specimen dimensions shown in Figure 5 are determined by the limitations of the tension SHB apparatus used in the high strain rate tests. In the high strain rate tests, the length of the gage section is inversely proportional to the achievable strain rate, where the length of the tensile wave is governed by the length of the clamped section of the incident bar. The thickness and width of the gage section is determined by the load capacity of the glue. The specimen must fail before the bond between the specimen and the bar does. The design requires less than 2670 N (600 lb) to fail the specimen and permits a strain rate up to 2000 s^{-1} .



Dimensions shown in millimeters

Figure 5. High strain rate tension specimen geometry

The high strain rate specimen is used as the base design for the low rate and elevated temperature tension tests. The gage section matches that of the other specimens in the tension series. Slight modifications are made to the specimen in those tests, which include extending the flange to 63.5 mm for the low rate tests. Additionally, the elevated temperature test specimens feature two 4.50 mm through-holes in the flange 7.62 mm from each end of the specimen. These holes are used with the high temperature tension fixture that uses pins and bushings to hold the specimen. These modifications accommodate different fixtures and do not affect the dimensions of the gage section. The low strain rate test and elevated temperature test specimens are illustrated in Figure 6 and Figure 7.

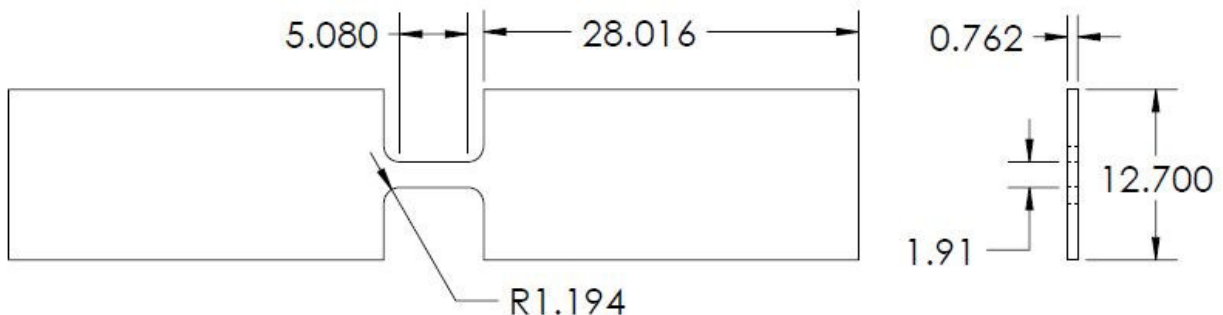


Figure 6. Low rate tension test specimen geometry

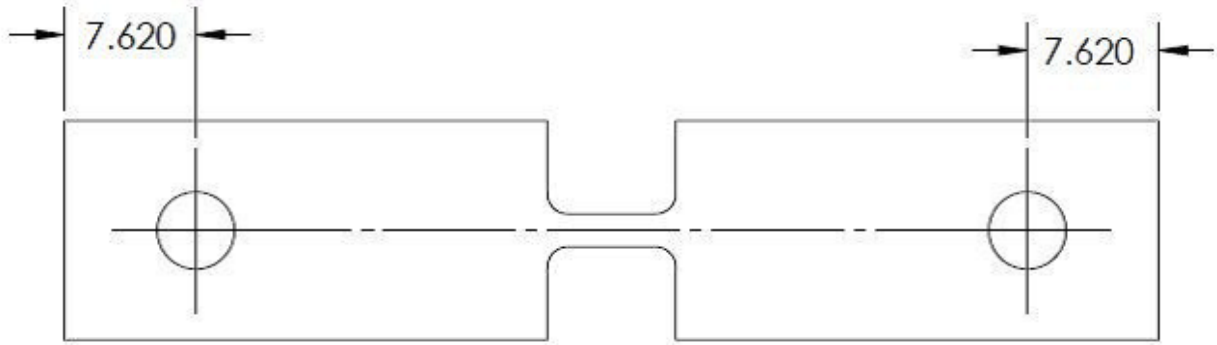


Figure 7. Elevated temperature tension test specimen geometry

3.2.2 Compression specimen

The cylindrical compression specimen was designed based on the limitations of the compression SHB with the aim to maintain a uniaxial state of stress. The maximum achievable strain rate is inversely proportional to the length of the specimen gage at the max striker velocity. Therefore, the length of the specimen must be limited. The diameter is designed to be the same as the length in order to prevent buckling which induces undesirable complex stress states. The compression specimen dimensions are shown in Figure 8.

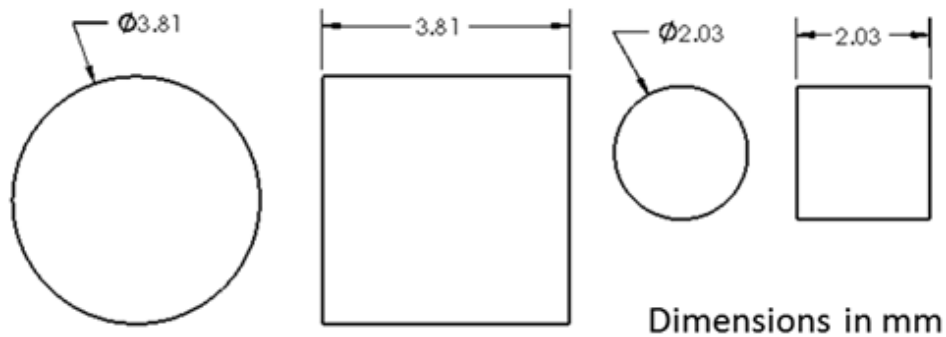


Figure 8. Compression specimen geometry

Two specimens are designed for the strain rate dependence testing. The first is 3.81 mm in length and 3.81 mm in diameter. This specimen is limited to 2000 s^{-1} . An additional specimen, scaled down to 2.03 mm in diameter and length, is made for a target rate of 5000 s^{-1} . The compression specimens are cut with an electrical discharge machine (EDM) in the rolling direction of the material from P4. The EDM recast layer on is ground off.

Additional compression experiments are conducted on specimens manufactured from plates P1, P2, P3, and P4. P5 is excluded since it is too thin to design a compression specimen. The cylinder dimensions must be reduced for P2 and the orientation must be changed to through thickness for P1 to accommodate design of the compression specimens from the thinner plates. Due to the different specimen geometries, each plate was tested at a different dynamic rate. All plates were tested at a static rate of 0.001 s^{-1} . The specimen dimensions, material orientation, and dynamic rates are specified for each plate in Table 7.

Table 7. Compression specimen dimensions, orientation, and strain rate for each plate

Plate Thickness (mm)	Cylinder Height (mm)	Cylinder Diameter (mm)	Specimen Orientation	Strain Rate (1/s)
2.03 (P1)	2.03	3.81	Through Thickness	2000
3.17 (P2)	3.05	3.05	Rolling	3800
6.35 (P3)	3.81	3.81	Rolling	1230
12.7 (P4)	3.81	3.81	Rolling	1000

3.2.3 Torsion specimen

The torsion specimen is also designed based on the limitations of the torsion Kolsky bar and material stock thickness. A hollow thin wall specimen with flanges is used. This geometry reduces the cross sectional area of the specimen while increasing the available bonding area ensuring that sufficient force is transmitted through the bond to fail the specimen. The overall length of the specimen is 12.7 mm, which is determined by the stock through thickness of P4, from which the specimen is cut. A gage section length of 2.54 mm and 1.78 mm is used to achieve the two dynamic strain rate targets of 500 and 2000 s^{-1} . The specimen was designed so that the specimen flange and incident bar have the same impedance to prevent unwanted wave reflections from the incident bar and specimen interface. The specimen flange is designed with an outer diameter (OD) of 17.22 mm to match the impedance of the incident bar. A fully dimensioned drawing of the specimen is shown in Figure 9.

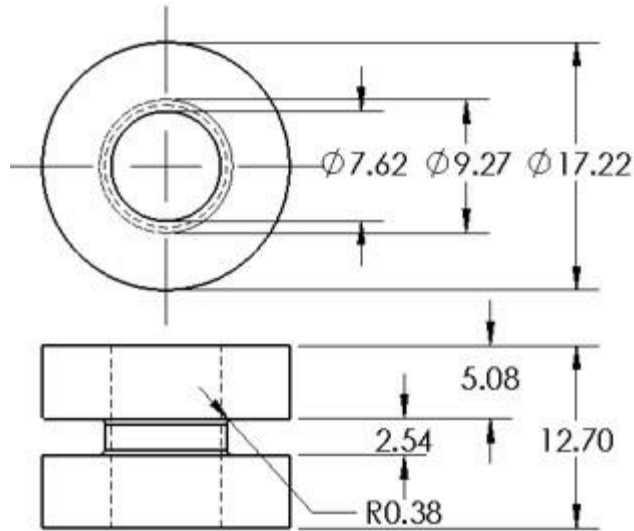


Figure 9. Torsion specimen geometry

3.3 Low strain rate room temperature test methods

Low strain rate tests are performed at room temperature to evaluate the mechanical response of Inconel 718 at strain rates ranging from 0.0001 s^{-1} to 1.0 s^{-1} . Inertial effects are negligible at strain rates in this low range and therefore these rates are often referred to as quasi-static. The low strain rate room temperature tests include tension, compression, and shear tests to characterize plastic deformation on the specimens described in Section 3.2 and additionally several loading modes on fracture specimens as described in Section 3.6.

All low rate tests are performed on an Instron 1321 servo-hydraulic biaxial load frame shown in Figure 10. This machine's actuator can move axially with $\pm 63 \text{ mm}$ stroke limits and rotate with $\pm 45^\circ$ angle limits providing capability for uniaxial tension and compression, torsion (pure shear), and combinations of tension-torsion and compression-torsion. Two different load cells can be equipped depending on the expected force (or torque): an Interface 1216CEW-2k with a capacity of 8.9 kN (110 Nm) or a Lebow 6467-107 with a capacity of 89 kN (1100 Nm). The machine is controlled by an MTS FlexTest SE controller with software that allows the user to independently control both the axial and torsional channels of the load frame. The controller acquires data through MTS 493.25 Digital Universal Conditioners with maximum sample rates of 100 kHz and 22-24 bit resolution.

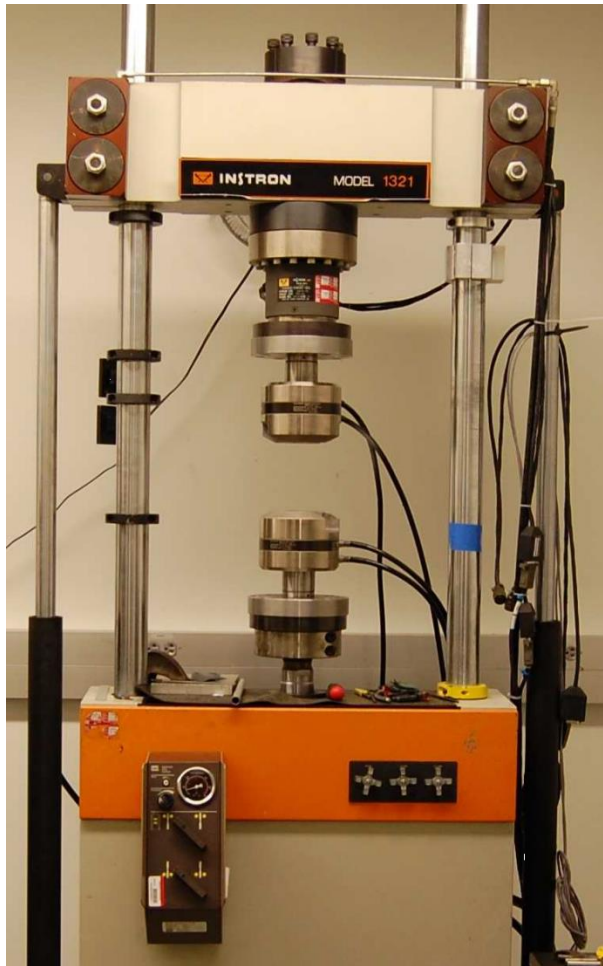


Figure 10. Instron 1321 servo-hydraulic biaxial load frame equipped with hydraulic wedge grips

A Linear Variable Differential Transformer (LVDT) and a Rotational Variable Differential Transformer (RVDT) are used to control the load frame's actuator. The LVDT and RVDT also provide force/torque and linear and angular displacement measurements and can be used for strain computations but are not as accurate as DIC measurements as shown in detail by Seidt (Seidt, 2014). Therefore, DIC data is utilized for all strain results presented herein.

3.3.1 Tension at low strain rates

Low strain rate room temperature tension tests are conducted using an 89 kN test setup. The specimen is held 12.7 mm from the gage section using MTS hydraulic grips with flat serrated wedge jaws at either end as shown in Figure 11.

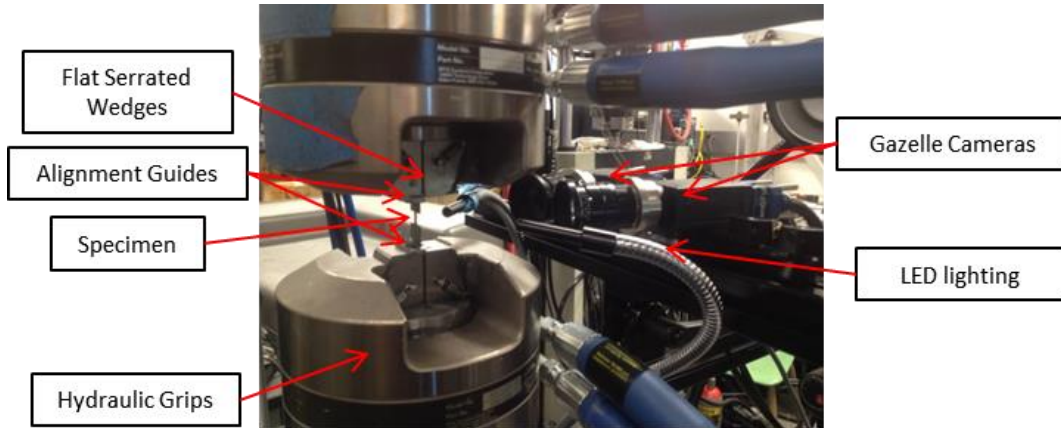


Figure 11. Low rate room temperature tension test setup

The machine is placed in load control mode to maintain a zero load on the specimen while pressure is slowly applied as the grips are tightened. The upper clamp is connected to the 89 kN load cell, which is fixed to the crosshead at the top of the load frame. The lower clamp is connected to the actuator head. The load frame controller is programmed to move the actuator downwards in displacement control at a constant speed. The specimen is pulled at the target nominal strain rate with the velocity of the actuator, calculated in the following manner from Equation 10, where \dot{u} is the actuator velocity, $\dot{\epsilon}_E$ is the nominal engineering strain rate, and l_s is the length of the specimen's gage section.

$$\dot{u} = \dot{\epsilon}_E l_s \quad 10$$

Data recorded during a test includes force and actuator displacement as a function of time. In addition, full-field deformation is measured directly on the surface of the specimen using 3D DIC. Images for the DIC analysis are recorded by two cameras that are positioned less than 0.5 m from the specimen, on the same vertical plane, such that they are focused on the gage section of the specimen with roughly 12° to 15° angle between them. The strain in the specimen is tracked using a 4 mm virtual extensometer centered over the gage section. The experimental setup is shown in Figure 12. Point Gray Research GRAS-20S4M-C cameras with a 1624×1224 pixel resolution are used in experiments at nominal strain rates of 0.0001 s^{-1} and 0.01 s^{-1} . Photron MC2 cameras with a resolution of 512×512 pixels are used in experiments at a nominal strain rate of 1.0 s^{-1} . All quasi-static tests use Schneider 30 mm lenses. The framerate of the cameras is set such that about 500 images are taken during each test. A National Instruments DAQ is used to record the analog output of the force from the load cell. The force outputs from the load cell and force measurement at every DIC image instant are used to synchronize the data set times. A

force is then calculated for each DIC image by interpolating the time at each image from the load cell data set.

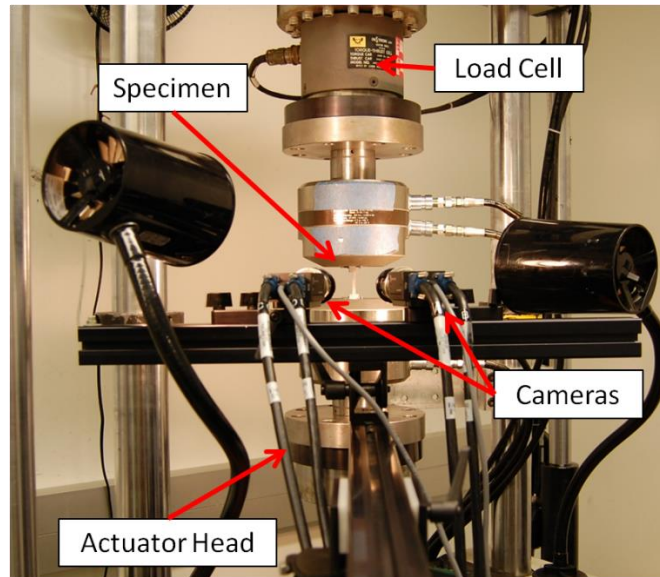


Figure 12. Low strain rate tension setup

The specimen geometry was previously shown in Figure 6 in Section 3.2.1. The geometry is dictated by the requirement of the high strain rate tests, which are done using the split Hopkinson bar technique. This technique requires a short specimen with relatively small maximum force. To eliminate any influence of the specimen geometry on the measured strain rate sensitivity, specimens with the same geometry and gage dimensions are used in the tests at all strain rates.

Engineering stress and engineering strain are calculated from measurements of the specimen dimensions and the recorded loads and displacements from the experiment. The engineering strain is calculated using Equation 11:

$$\varepsilon_E = \frac{\Delta l}{l_0} \quad 11$$

where Δl is the displacement between two points on the surface of the specimen (a 4mm virtual extensometer that is centered over the failure point) and l_0 is the initial gage length.

The engineering stress σ_E is calculated by Equation 12:

$$\sigma_E = \frac{F}{wt} \quad 12$$

where F is the loading force, w is the initial gage width, and t is the initial gage thickness. These two values can be converted to true strain ε_T and true stress σ_T using Equations 13 and 14.

$$\varepsilon_T = \ln(1 + \varepsilon_E) \quad 13$$

$$\sigma_T = \sigma_E(1 + \varepsilon_E) \quad 14$$

3.3.2 Compression at low strain rates

The low strain rate room temperature compression experimental set up, shown in Figure 13 is similar to that used in quasi-static tension experiments. The compression specimen geometry used was previously shown in Figure 8. The specimen is placed between two 12.7 mm diameter tungsten carbide platens. The contact surfaces between platen and specimen are lubricated with molybdenum disulfide (MoS₂) grease. These platens are fit into cylindrical slots cut in the top and bottom fixtures. The top fixture is mounted to the 89 kN load cell, and the load cell is fixed to the crosshead of the load frame. The bottom fixture is mounted to the actuator head of the load frame. Two cameras are positioned between 0.25 m and 0.50 m from the specimen such that their focal points are trained on the same location on the specimen surface and the angle between them is between 10° and 15°. As in the tension tests, around 500 images are recorded in each test. Tests at the nominal strain rate of 0.0001 s⁻¹ and 0.01 s⁻¹ use Point Gray Research GRAS-20S4M-C cameras, and tests at 1.0s⁻¹ use Photron MC2 cameras.



Figure 13. Low strain rate compression setup

The load frame controller is programmed to move the actuator at a constant speed. The specimen is compressed at the target nominal strain rate with the displacement of the actuator, calculated using the method as for tension from Equation 10.

Data recorded during a test includes time, force, and actuator displacement. In addition, full-field deformation is measured directly on the surface of the specimen with a 2 mm virtual extensometer that is centered using 3D DIC. The engineering strain is calculated using Equation 11 as in the tension tests. The engineering stress σ_E is calculated by using Equation 15, where F is the applied compressive load, and d is the initial specimen diameter. True stress and strain are calculated using Equations 13 and 14.

$$\sigma_E = \frac{F}{\frac{\pi d^2}{4}} \quad 15$$

3.3.3 Torsion at low strain rates

Low strain rate room temperature testing in shear is done by applying torque to a thin-walled tube. A dimensioned drawing of the specimen was shown previously in Figure 9. The gage section is the thin-walled tube portion in the middle. The hexagonal flanges at the ends are used for attaching the specimen to the hydraulic machine. The attachment mechanism is shown in Figure 14. The hexagonal end slides into a circular hole in the adapter and each corner of the hexagonal is fixed in place by two M4 set screws.

To load the specimen, the load frame is placed in rotational displacement control where a ramp input is used. The machine is also in axial load control, set to maintain a zero axial load. The ramp input ($\dot{\theta}$) is calculated based on the desired torsional strain rate ($\dot{\gamma}_s$) by Equation 16, where $\dot{\theta}$ is the rate of rotation, r_m is the mean radius, and l_g is the nominal gage length.

$$\dot{\gamma}_s = \frac{\dot{\theta} * r_m}{l_g} \quad 16$$

DIC is used to take measurements of the specimen using Point Grey Gazelles with 50 mm lenses recording images. Rotation of the specimen is determined from the displacement of two points tracked on the surface of the gage section. Axial force, torsional force, and rotational displacement are recorded with the MTS frame at 10 Hz.

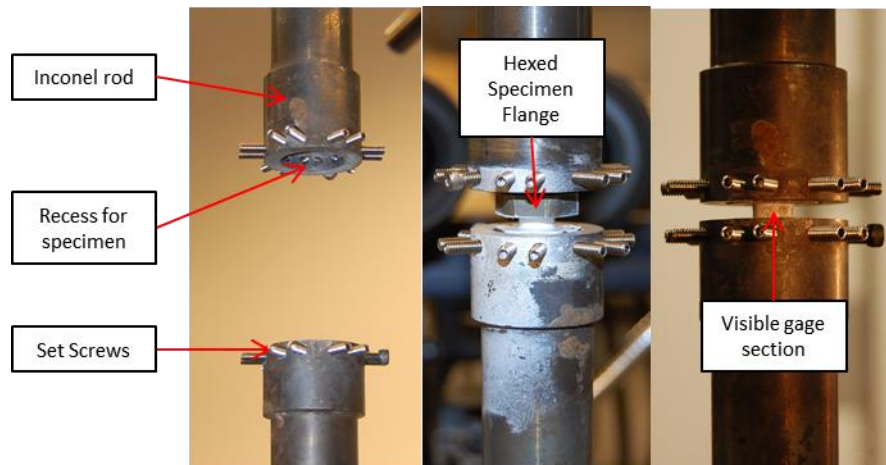


Figure 14. Attachment of torsion specimen to the hydraulic machine

3.4 Elevated temperature low strain rate test methods

Elevated temperature tests, up to temperature of 800 °C, are done by mounting a specially designed furnace on the servo hydraulic load frame. The experimental setup is shown in Figure 15.

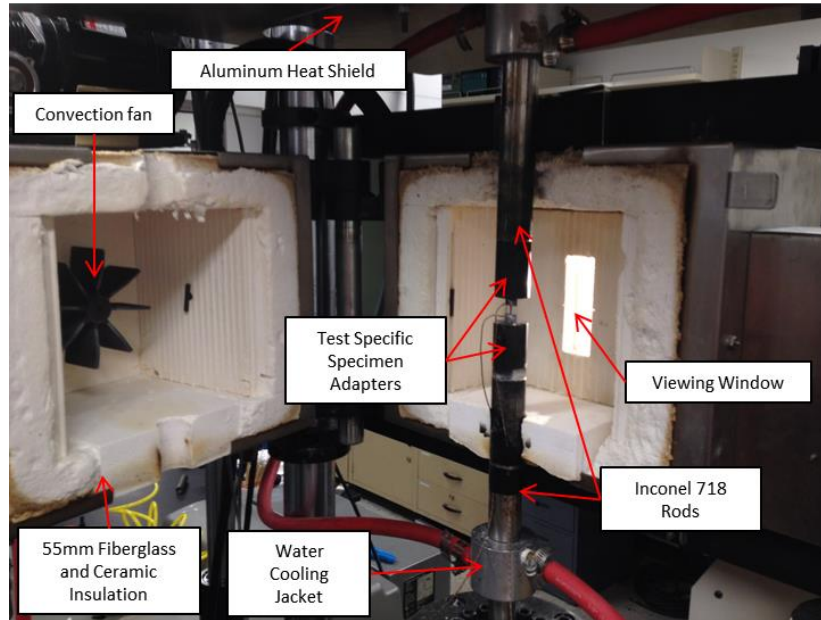


Figure 15. High temperature testing experimental setup

The furnace has cutouts in the body and insulation that allow fixtures to pass through the furnace and to be connected to the actuator and cross-head of the load frame. Two thermocouples mounted to the walls of the furnace provide a feedback signal for an Applied Test Systems controller that controls the air temperature inside the furnace. A 152 mm diameter fan in the rear of the furnace circulates the air during operation to insure a uniform air temperature. The front of the furnace has a 40 mm by 102 mm window to allow for DIC measurements. The window, made of optical quartz, floats in a loose ceramic frame attached to the furnace to allow for expansion without warping the glass, which could distort the images. A thin aluminum heat shield is attached above the furnace with a small fan blowing air overtop the heat shield to prevent convective heat transfer to the load cell. The setup requires the use of 31.75 mm diameter Inconel 718 rods attached to the load frame actuator. The rods extend into the furnace and attach to the test specimen adaptor. Water collars cool the Inconel rods to prevent conductive heat transfer from the furnace to the load cell and the load frame actuator. An image from a test in progress is shown in Figure 16, which shows the closed furnace and DIC cameras positioned in the viewing window with fiber optic light sources to illuminate the specimen.

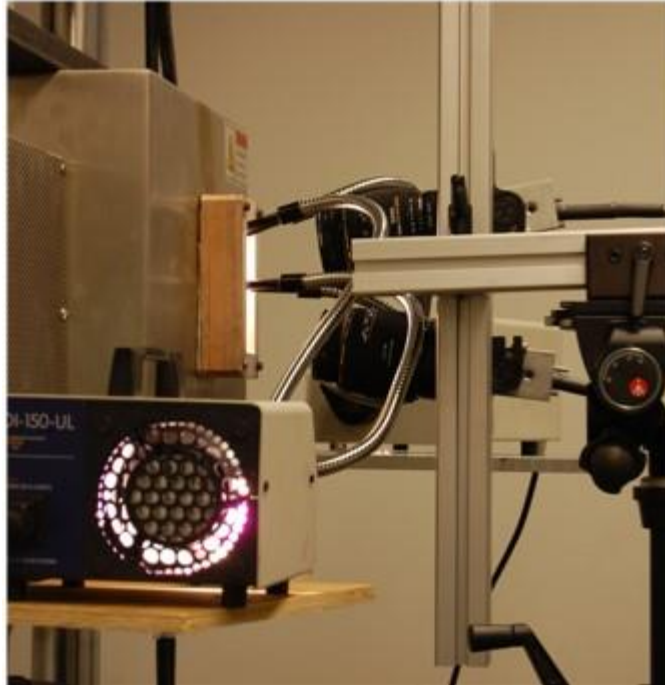


Figure 16. Close-up of elevated temperature setup

3.4.1 Tension at elevated temperatures

A diagram of the elevated temperature tension test fixture is shown in Figure 17. The fixture assembly is comprised of two slotted adapters, two #8 hex screws, two #8 hex nuts, and four 12.7 mm cylindrical bushings.

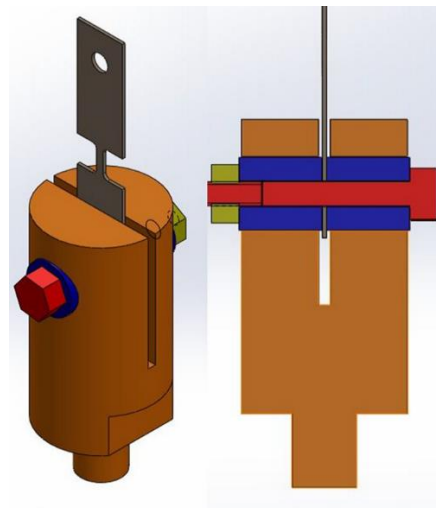


Figure 17. Diagram of elevated temperature tension test adapters

The slotted adapters, hex screws, and nuts are made from Inconel 718 and the bushings are machined from Hastalloy-X. The tension specimen is inserted into the slotted adapters, and bushings are placed in the holes. The screws are then inserted through the bushings and the nuts are secured to the other side. The slotted adapters are threaded such that they can be screwed into the Inconel 718 rods that extend through the furnace, and attach to the load cell and load frame actuator. The geometry for low strain rate tension experiments at elevated temperatures was shown previously in Figure 7.

Prior to commencing the test, the load frame is placed in load control and a 44.5 N tensile load is applied to the specimen before the hex screw is fully tightened. This eliminates any slip in the fixture and compensates for thermal expansion in the rods ensuring that the sample is not buckled.

The temperature of the specimen is measured with two thermocouples that are cemented to the back of the specimen above and below the gage section. The temperatures are averaged to determine the temperature in the gage section. The temperature history of the specimen is recorded during the pre-test heating phase. When the specimen temperature reaches the desired temperature the load frame is switched back into displacement control, and the actuator head is displaced at a constant velocity.

The elevated temperature tension experiments are conducted with a similar procedure as the low rate room temperature experiments. As the specimen is pulled, the load is transferred through both the friction force of the bushings and the screws. DIC measurements are made with a virtual extensometer as in the other tension experiments. Figure 18 shows a photograph of the tension adaptors and DIC camera setup used to image the specimen through the furnace window.

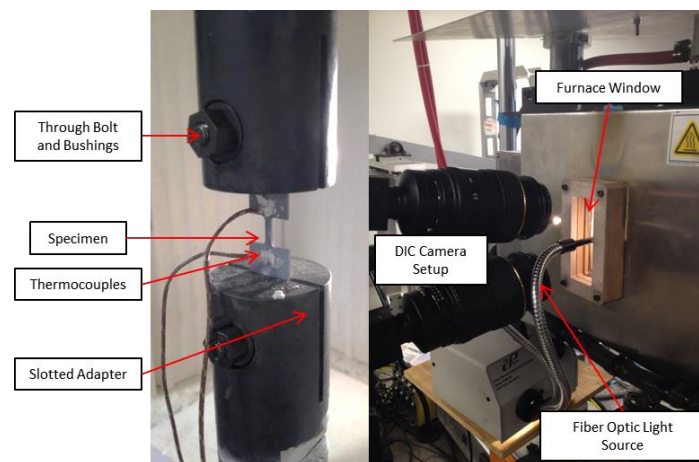


Figure 18. Tension specimen fixture and high temperature DIC camera setup

3.4.2 Compression at elevated temperatures

In compression, blunt adapters are threaded onto the Inconel 718 rods used in the tension experiment. The adapters thread on an additional adapter plate on which a tungsten platen is placed. The compression specimen is placed between the upper and lower platen. A high temperature silicon lubricant is used between the specimen and platens to reduce friction and allow planar movement. Two thermocouples are attached with a small amount of cement in the upper and lower interior corner between the specimen and the platen. The temperatures are averaged to determine the temperature of the specimen. As the specimen is heated, a load of 44.5 N is applied to the specimen to keep it in place during the heat up but allow it to expand without adding unintended compression. Due to the radial expansion of the specimen as it is compressed, the paint flakes off the surface preventing DIC surface measurements at large strains. To address this, DIC measurements are made using two extensometers. During the elastic portion of the loading, a 2 mm extensometer on the specimen is used to measure the strain. After the specimen begins to yield, the subsequent strain is measured with an extensometer placed on the platens. This method assumes that all further deformation occurs in the sample and the tungsten platens remain rigid. This measurement method is shown in Figure 19.

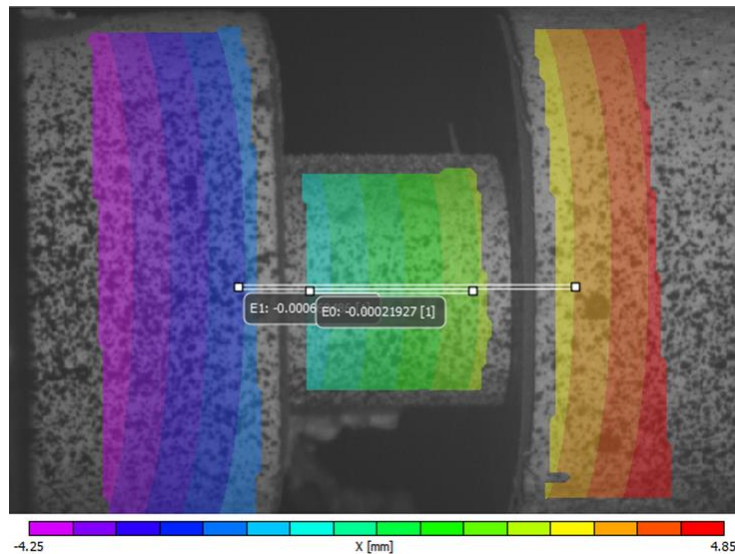


Figure 19. The initial frame of a compression test with the specimen and platen virtual extensometers

3.4.3 Torsion at elevated temperatures

The elevated temperature torsion tests use slightly different Inconel 718 rods to connect the load cell and actuator to the specimen in the furnace. The rods are machined to have a 12.7 mm deep, 19.05 mm diameter round pocket inset in one end. Twelve Grade 5 Titanium M6 setscrews protrude perpendicular into the pocket. These setscrews are used to fix the bottom of a torsional specimen fixture to prevent rotation during the test. The top of the torsional specimen fixture is a slotted collet where the hexed flange of the torsional specimens sit inset in the top of the fixture. The collet is compressed onto the specimen with the use of a slotted ring clamp. This setup is shown in Figure 20. Two thermocouples are affixed with a small amount of cement to the top and bottom of the gage section on the back of specimen to measure the temperature. The measured temperatures are averaged to determine the gage section temperature.

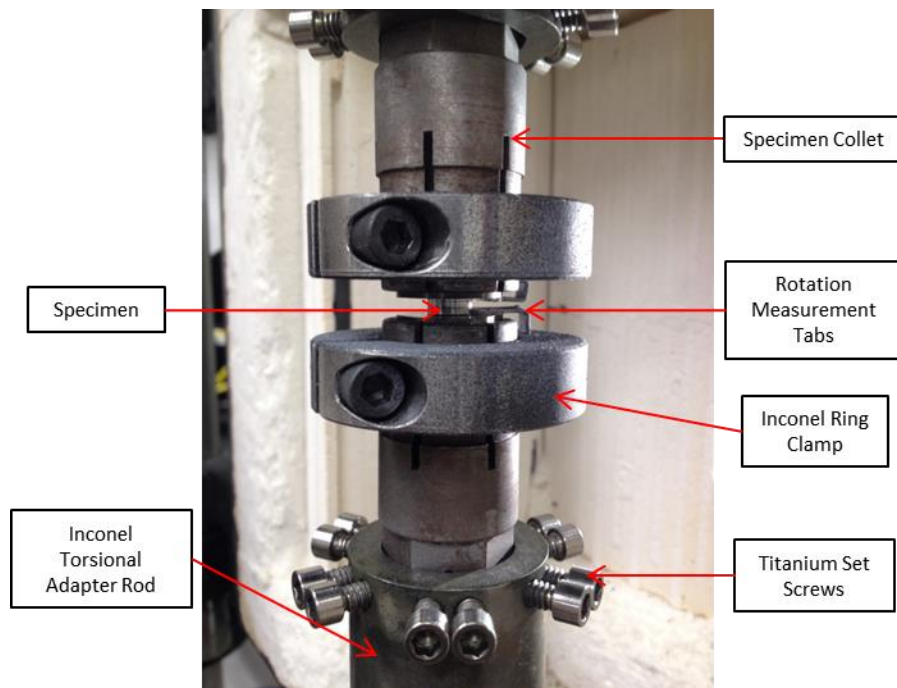


Figure 20. High temperature torsional specimen fixture

Due to the vertical configuration of the viewing window into the furnace and the width of the fixture gripping the specimens flange, DIC measurement of the gage are not made. Rotation of the gage section is measured using L-shaped bent tabs attached to the inside of the upper and lower flange of the specimen. Figure 21 shows the tabs in the initial and final frame along with the points used to calculate the rotation. The tabs extend out 15 mm from the gage section and the bent portion is patterned for DIC measurement. The rotation of the tabs is tracked in the same manner as the dynamic torsion test, by tracking the rotation of a point on the upper and lower

tab. The strain is calculated assuming the tabs are rigid and no deformation occurs between where the tabs are mounted to the flange and the gage section.

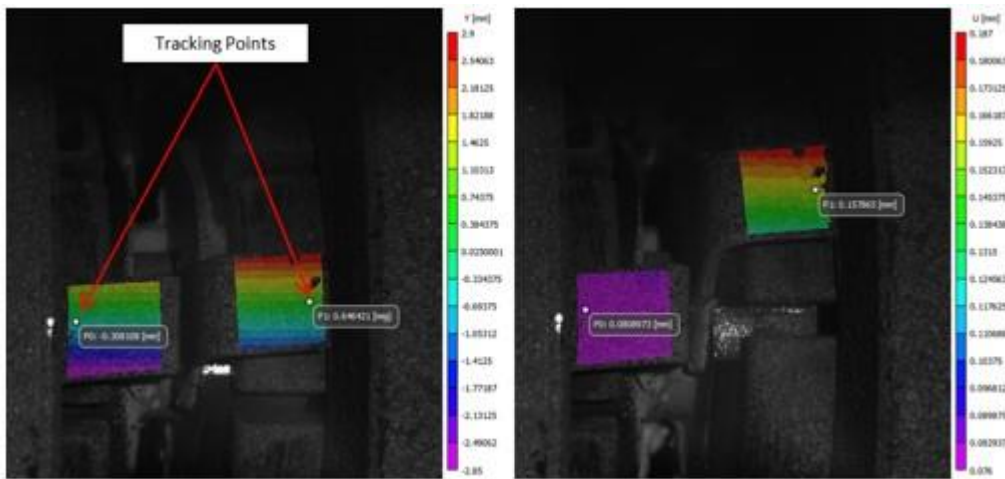


Figure 21. Initial and final frame of DIC used in torsional test to measure rotation in the gage section

3.5 High strain rate (Split Hopkinson Bar) test methods

High strain rate tests in the range of 500 s^{-1} to $5,000 \text{ s}^{-1}$ were done using the Split Hopkinson Bar (SHB) technique. Details of the experimental setups for testing in compression, tension, and torsion are described in the following sections.

3.5.1 Tension at high strain rates

A diagram of the tension SHB setup is shown in Figure 22. The tension SHB apparatus is composed of two bars, a 3.68 m long incident bar, and a 1.83 m transmitter bar. Both bars are 7075 aluminum and 12.7 mm in diameter. The specimen is bonded to slotted adapters with JB quick weld adhesive which are in turn bonded between the incident and transmitted bars with the same epoxy. The adapters are designed such that the cross section including the Inconel specimen has the same impedance as the incident and transmitter bars. The loading wave is generated by a pinned scissor clamp, 1.47 m from the start of the bar and a pretension induced with a hydraulic pump and pulley loading the bar. The loading wave is generated by breaking the pin and rapidly releasing the stored tensile strain as an elastic wave. Once this incident wave is released, it travels down the incident bar to the specimen and causes deformation by the relative motion between the bars ends. The transmitted wave travels through the specimen until it breaks, while the part of the incident wave is reflected back into the incident bar. Three Wheatstone bridges, labeled gage A, B, and C in the diagram in Figure 22, are used to measure the incident, reflected, and transmitted waves in the bars respectively. The three bridges are run at a 15 V

excitation that outputs a signal to a National Instruments amplifier and is measured using a Tektronix TD550348B oscilloscope sampling at 5 MHz.

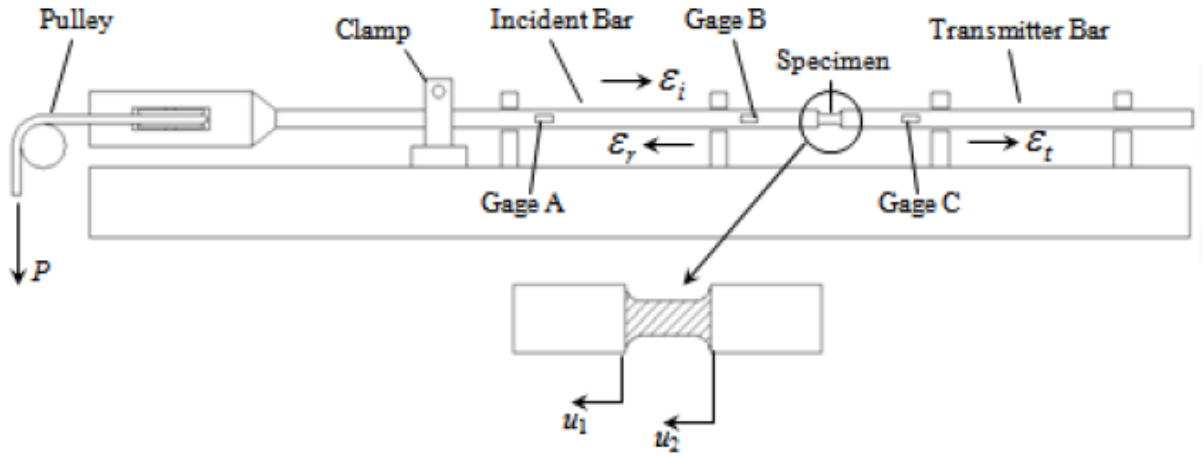


Figure 22. Schematic of tension split-Hopkinson bar

The following equations are used to calculate the engineering stress and strain from the measured waves using the various properties of the SHB apparatus and the specimen dimensions (Staab & Gilat, 1991). The linear velocities at each end of the specimen at the ends of the incident, \dot{u}_i and transmitter bar, \dot{u}_t at time t can be determined from 1-D wave theory using Equations 17, 18, and 19. A is the cross sectional areas of the bar, ρ is the density, c is uniaxial wave speed in the bar, and E is the modulus of elasticity of the bar. F_A , F_B , and F_C are the tensile forces at gages A, B and C calculated from the strain measurements. L_A , L_B , and L_C are the distance of the gages from the end of the bar that is attached to the specimen.

Assuming a homogenous state of uniaxial tension and deformation, the relative linear velocities can be used to calculate the strain rate using Equation 20, where l is the gage length of the specimen.

$$\dot{\varepsilon}(t) = \frac{\dot{u}_i - \dot{u}_t}{l} \quad 20$$

Integrating this result with respect to time yields the engineering strain expressed in Equation 21.

$$\varepsilon_e(t) = \int_0^t \dot{\varepsilon}(t) dt \quad 21$$

The engineering and true stress in the specimen is determined from measurements at gage C and the specimen dimensions in the Equations 22 and 23, where A_s is the cross sectional area of the specimen.

$$\sigma_e(t) = \frac{F_c}{A_s} \left(t + \frac{L_C}{c} \right) \quad 22$$

$$\sigma_t = \sigma_e(1 + \varepsilon_e) \quad 23$$

Full surface displacement measurements are also made using DIC in the high rate SHB tests as described in Seidt (2014). A high-speed stereo camera setup using two photon SA1.1 cameras, running at 210,000 fps, records approximately 100 images for each test. A 4 mm virtual extensometer tracks the strain in the gage section of the specimen. This extensometer is centered on the failure point of the specimen that is also tracked throughout the test. An example is shown in Figure 23.

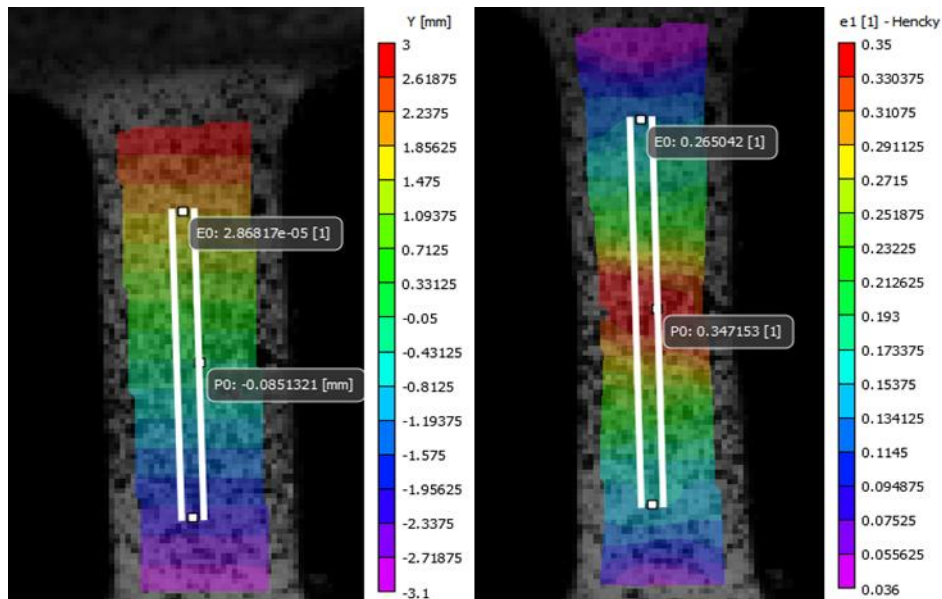


Figure 23. Initial Y position with the extensometer and failure point (left) and e1 at the final frame (right)

The engineering (ε_e) and true (ε_t) strain in the gage section are calculated by the elongation of the virtual extensometer in the Equations 24 and 25, where Δl is the change in extensometer length and l_g is the extensometer's original length.

$$\varepsilon_e = \frac{\Delta l}{l_g} \quad 24$$

$$\varepsilon_t = \ln(1 + \varepsilon_e) \quad 25$$

3.5.2 Compression at high strain rates

A diagram of the compression SHB setup is shown in Figure 24. The setup consists of three 12.7 mm diameter Ti-6Al-4V bars, the incident bar, the transmitter bar, and the striker bar, with lengths of 1.88 m, 1.88 m, and 0.61 m respectively. The specimen is placed between the incident and transmitter bars, each of which has a threaded insert that includes a tungsten platen. The interface between the tungsten platen and the specimen is greased to reduce friction. A detailed view of this setup is shown in Figure 25.

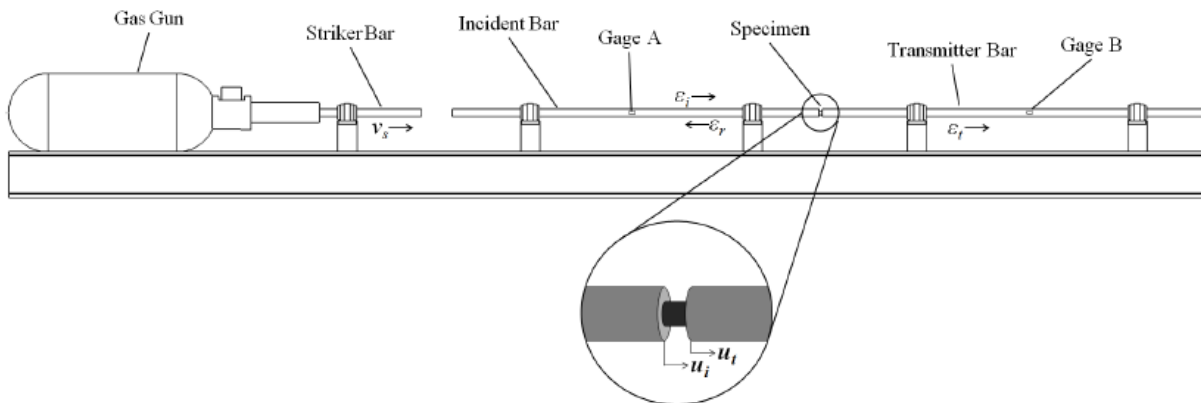


Figure 24. Diagram of split-Hopkinson compression pressure bar

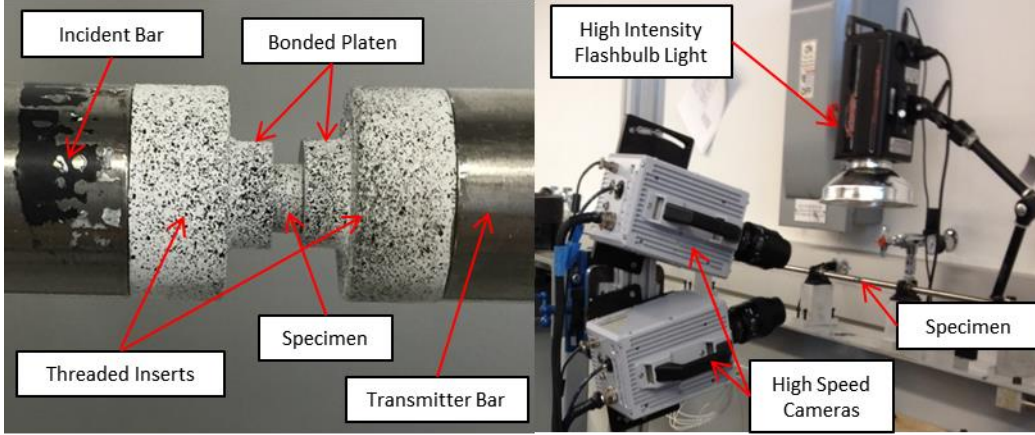


Figure 25. Specimen and bar contact setup (left). Camera and light setup (right)

Two full Wheatstone bridges are located on the incident and transmitter bars, each 863 mm from the specimen. These gages are excited with a 15 V excitation and the signal is amplified with a signal preamplifier. The signal is recorded at 5 MHz with a Tektronix oscilloscope. The test is conducted by generating a compression wave by striking the incident bar with the striker rod. The striker rod is propelled by a gas gun where the pressure is regulated to control the striker velocity. The incident compression wave travels down the bar and is measured with gage A. Once the wave reaches the specimen, part of the wave travels through the specimen and into the transmitter bar with the remaining part reflecting back to the incident bar. The reflection is measured with gage A on the incident bar while gage B measures the transmitted wave.

The strain rate is determined by calculating the relative velocity between the specimen end of the incident and transmitter bars from the reflected wave in Equation 26, where l_s is the length of the sample and ϵ_r is the strain of the reflected wave measured at gage A.

$$\dot{\epsilon} = \frac{2 * c_b * \epsilon_r}{l_s} \quad 26$$

c_b is the elastic wave speed in the bars and is a function of the elastic modulus and density as shown in the Equation 27.

$$c_b = \sqrt{\frac{E_b}{\rho}} \quad 27$$

The strain is derived from these results by integrating the strain rate with respect to time.

The stress in the specimen is calculated by Equation 28, where A_b is the cross section area of the bar, ε_t is the strain in the transmitted bar measured at gage B, and A_s is the cross sectional area of the specimen.

$$\sigma = \frac{A_b E_b \varepsilon_t}{A_s} \quad 28$$

Full surface displacement measurements are also made with DIC using high speed Photron SA1.1 cameras with Nikon 105 mm lenses, running at 180,000 and 270,000 fps for strain rates 2000 s^{-1} and 5000 s^{-1} respectively. The DIC setup is shown in the right image of Figure 25. Measurements are made using a 2 mm extensometer centered on the specimen and an averaging box. The averaging box averages all the data points in the box, approximately 3500. A figure of this data extraction method is shown in Figure 26.

The engineering (ε_e) and true (ε_t) strains in the gage section are calculated by the elongation of the virtual extensometer in the same manner as the tension SHB following Equations 24 and 25.

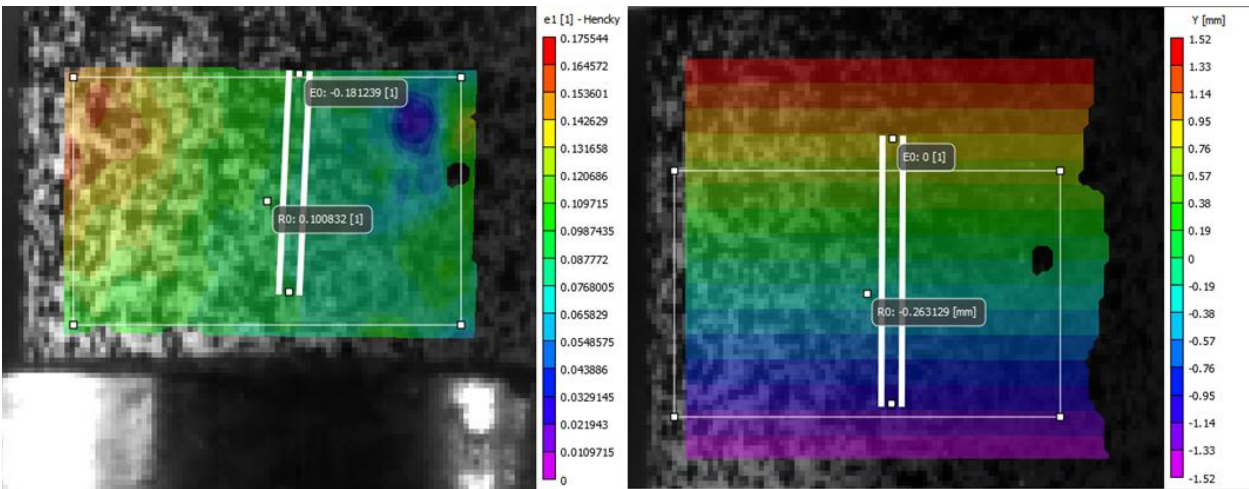


Figure 26. (Left) Initial Extensometer and Averaging Box with the Y[mm] coordinate plot and (Right) the final frame with the extensometer and averaging box overlaid on the first principal strain plot

3.5.3 Torsion at high strain rates

A torsional Kolsky Bar is used to conduct dynamic torsion testing with target strain rates of 500 s^{-1} and 2000 s^{-1} . This technique is described in detail by Gilat (2000). A diagram of the apparatus is shown in Figure 27.

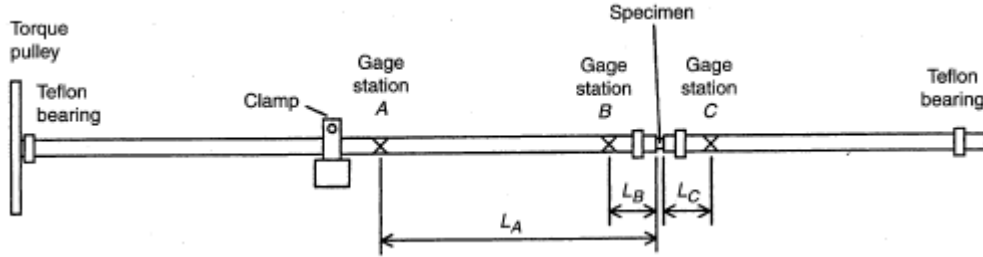


Figure 27. Schematic representation of the Kolsky bar at the DMML

Similar to the tension SHB, this design consists of 7075 aluminum incident and transmitter bars of lengths 2.28 m and 2.03 m respectively. A fracture pin clamp, of same design used in the tension SHB, is located 1.23 m away from the specimen on the incident bar. Three full Wheatstone bridges are set up to measure the waves in the bars. Gage A is located on the incident bar 1715 mm from the specimen. Gages B and C are located 385 mm from the specimen on the incident and transmitter bars respectively. A 20 V excitation is applied to the gages, which output to a Tektronix differential preamplifier. The signal from the amplifiers is recorded with a Tektronix oscilloscope at 5 MHz. The test is conducted by applying a pre-torque to the clamped section of the incident bar and once the desired pre-torque is reached, the fracture pin clamp releases the stored elastic wave.

The shearing incident wave travels down the incident bar to the specimen where part of the incident wave is reflected. The incident wave is measured at gage A and the reflection in the incident bar is measured at gage B. The wave transmitted through the specimen is measured on the transmitter bar at gage C. The amplitude of the shearing incident wave γ_i is calculated using Equation 29, where T_p is the preload torque, r_b is the radius of the bar, G_b is the shear modulus of the bars, and J_b is the polar moment of inertia of the bar.

$$\gamma_i = \frac{T_p r_b}{2G_b J_b} \quad 29$$

From elastic wave theory the rotational velocity of the incident ($\dot{\theta}_i$) transmitter bar ($\dot{\theta}_t$) is determined at time t by Equations 30 and 31, where ρ is the density of the bar, T_A , T_B , and T_C

are the forces measured at their respective gages, and L_a , L_b , and L_c are the distances of each gage for the specimen.

$$\dot{\theta}_i(t) = \frac{1}{\rho * J_b * c} \left[T_A \left(t - \frac{L_a}{c} \right) + T_A \left(t - \frac{L_a}{c} + 2 \frac{L_b}{c} \right) - T_B \left(t - \frac{L_b}{c} \right) \right] \quad 30$$

$$\dot{\theta}_t(t) = \frac{1}{\rho * J_b * c_b} [T_C(t - t_c)] \quad 31$$

The elastic wave speed, c , in the bar is calculated from Equation 32.

$$c = \sqrt{\frac{G_b}{\rho}} \quad 32$$

The shear strain rate, $\dot{\gamma}_s$, is determined by the relative velocity of the incident and transmitter bars and dimensions of the specimen using Equation 33, where r_m is the mean radius of the specimen and l_s is the length of the gage section.

$$\dot{\gamma}_s(t) = \frac{[\dot{\theta}_i(t) - \dot{\theta}_t(t)] * r_m}{l_s} \quad 33$$

Integrating the specimen shear strain rate yields the strain expressed in Equation 34.

$$\gamma_s(t) = \int_0^t \dot{\gamma}_s(t) dt \quad 34$$

The shear stress in the specimen is found assuming force equilibrium and thin walls in Equation 35, where A_s is the cross sectional area of the gage section of the specimen. DIC is used to make measurements.

$$\tau_s(t) = \frac{T_C(t - t_c)}{A_s * r_m} \quad 35$$

The test setup is shown in Figure 28. Two Photron SA1.1 are setup in a stereo configuration running at 150,000 FPS for the 500 s⁻¹ tests and at 270,000 FPS in the 2000 s⁻¹ tests. The shear strain in the specimen is measured by the displacement of two points on the specimen surface.

These points are selected in the center of the specimen and spaced 2 mm apart. These initial points are shown in the left side of Figure 29.

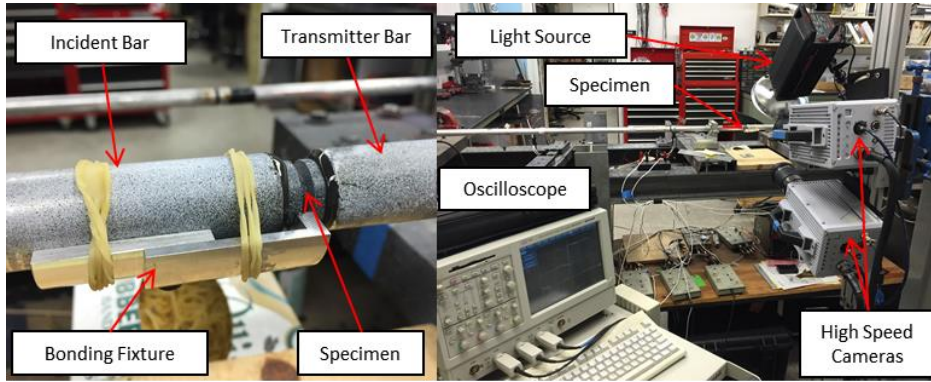


Figure 28. Torsional specimen setup (left). DIC acquisition system setup (right)

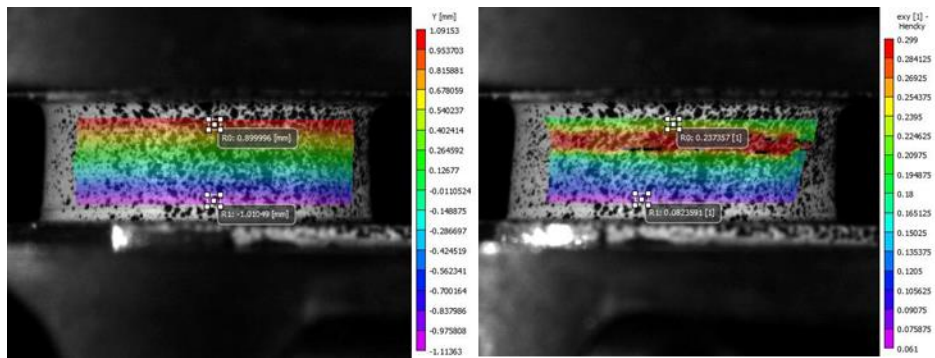


Figure 29. Initial (left) and final (right) selected DIC measurement points

For the shorter high strain rate specimens, 1.25 mm spacing is used. The x, y, and z displacements of each point are tracked over the course of the test. The x and z displacements are used to determine the rotation of each point on the gage section using Equation 36, where r_o is the radius of the outer surface and θ is the angle of rotation.

$$\theta = \cos^{-1} \left(1 - \frac{\Delta X^2 + \Delta Z^2}{2r_o^2} \right) \quad 36$$

The DIC shear strain, γ_{xy} , is calculated from the relative rotation θ_r of the upper and lower point as shown in Equation 37, where r_m is the mean radius of the specimen and l_g is the original distance between the two points.

$$\gamma_{xy} = \frac{\theta_r * r_m}{l_g}$$

This measurement method provides a direct measurement of the rotation of the gage section. The rotations measured from the waves include rotation that occurs outside the gage section and the difference between these measurements is shown in Figure 30. Therefore, DIC is used to calculate the torsional strain in the dynamic torsion experiments.

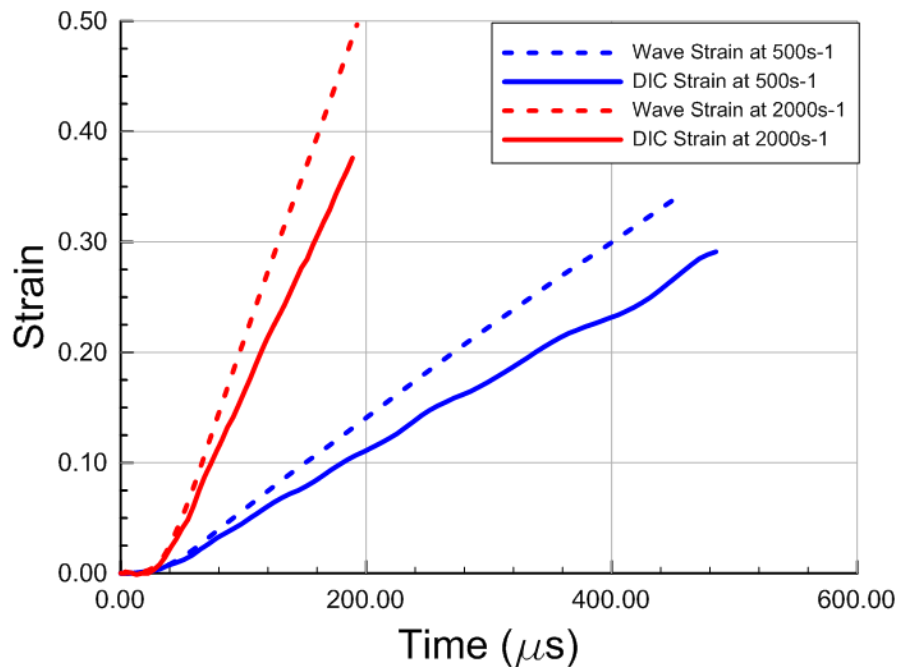


Figure 30. Comparison of strain measurements from wave and DIC at 500s⁻¹ and 2000s⁻¹

3.6 Ductile fracture experimental methods

The ductile fracture of Inconel 718 is examined at various stress states by subjecting different specimen geometries to a variety of loading configurations. The fracture series includes thin plane stress specimens, thick plane strain specimens, axisymmetric specimens, combined loading tests, and punch tests. Tension tests are performed on the plane stress, plane strain, and axisymmetric specimens. Combined loading mode tests in pure torsion, torsion-tension, and torsion-compression as well as quasi-static and dynamic punch tests are also conducted.

3.6.1 Fracture specimen design

The fracture specimens for Inconel 718 must be designed such that they result in experimental failure strain data at a variety of data points in the triaxiality and Lode parameter stress space. The specimen geometries are designed using finite element simulations in LS-DYNA to numerically predict the stress state of candidate specimen geometries. The goal is to generate a stress state dependent fracture locus determined by the plastic failure strain as a function of triaxiality and Lode parameter stress. The work closely follows the study of ductile fracture for Ti-6Al-4V performed by Hammer (2014) and for 2024-T351 Aluminum performed by Seidt (2014)

Simulated specimens are meshed with hexahedral elements with a characteristic length of 0.1524 mm per element in the gage section. This results in 5 elements across the thickness of plane stress geometries, 32 elements across the minimum notch diameter of axisymmetric geometries, and 167 elements across the thickness of plane strain geometries. Representative meshes are shown in Figure 31.

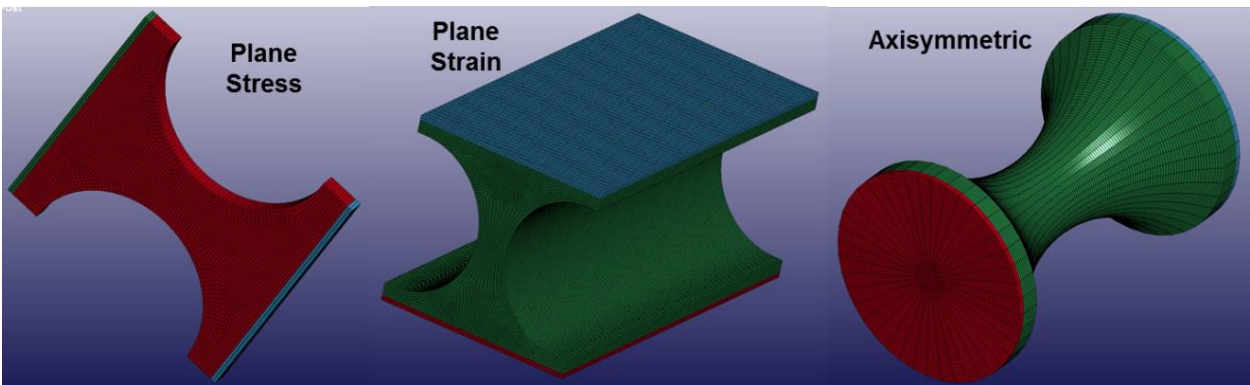


Figure 31. Representative meshes for plane stress (left), plane strain (center), and axisymmetric (right)

The specimens are simulated by applying a constant velocity in the axial direction to one end while the other is fixed. After the simulation is complete, data is extracted from the element located at the center of the minimum notch width, which is the first element expected to fail. These locations are highlighted in Figure 32. Equivalent plastic strain and three principal stress histories are extracted from this element. From this data, the average triaxiality σ_{avg}^* is computed using the Equation 38.

$$\sigma_{avg}^* = \frac{1}{\bar{\epsilon}_f^p} \int_0^{\bar{\epsilon}_f^p} \sigma^* d\bar{\epsilon} \quad 38$$

The average lode parameter $\bar{\theta}_L$ is calculated using Equation 39.

$$\bar{\theta}_L = \frac{1}{\bar{\epsilon}_f^p} \int_0^{\bar{\epsilon}_f^p} \theta_L d\bar{\epsilon} \quad 39$$

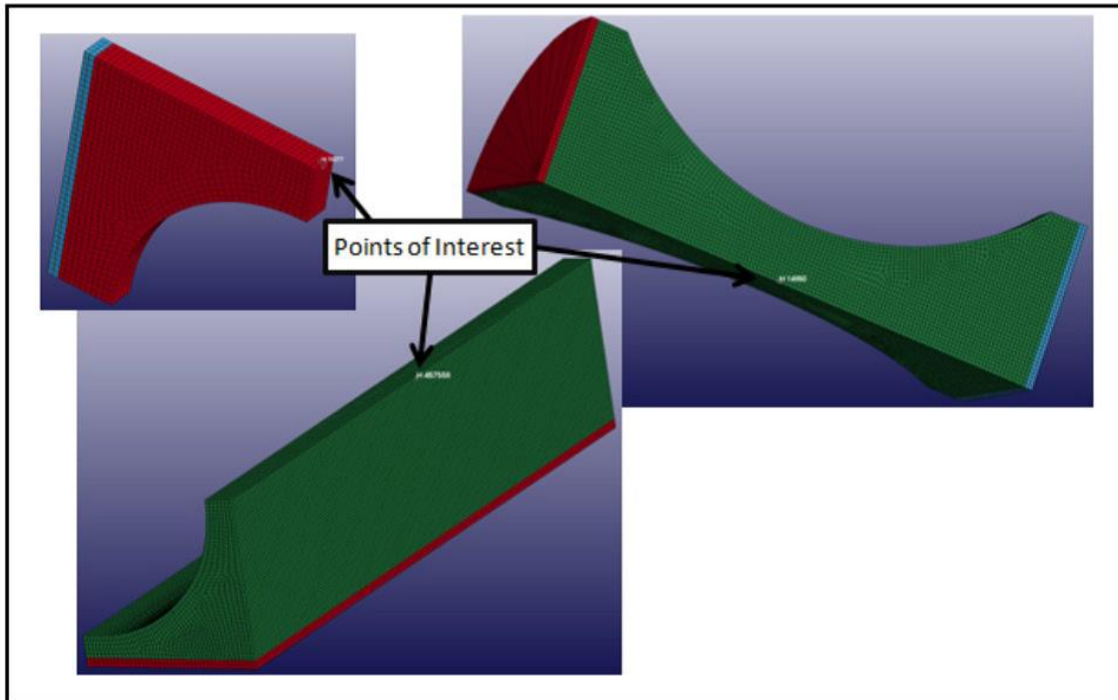


Figure 32. Meshed geometries with arrows highlighting the location from which data is extracted in fracture specimen design process

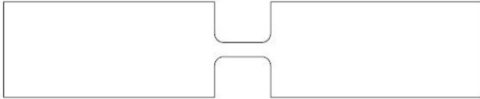
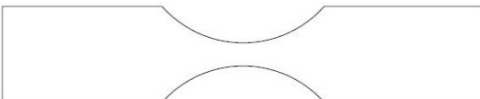
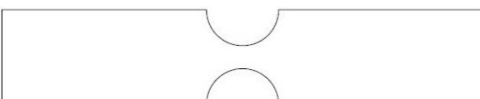
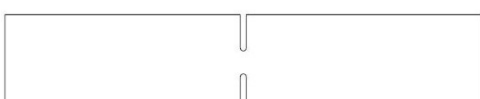
The geometry for the fracture specimens, dimensions, average triaxiality, and Lode parameter are shown below. Stress triaxiality and lode parameter are calculated using principal stress data from LS-DYNA simulations and the average stress-state equations presented above. As mentioned previously, the sign convention defined for triaxiality in Equation 1 and used

throughout this report is the one conventionally used in literature and the opposite sign as in LS-DYNA.

Single axis tension loading is performed on the plane stress and plane strain specimens using the same methods and fixtures as the low rate tension loading detailed in Section 3.3.1, with a constant displacement ramp. The axisymmetric tension specimens also use the same grips as the combined loading which is necessary to hold the round specimens as described in Section 3.6.2


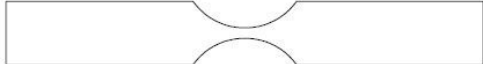

The plane stress specimens have notch radii ranging from 0.396 mm to 14.29 mm. The triaxiality for these specimens range from 0.355 to 0.574 to and the Lode parameter ranges from 0.603 to 0.943. All plane stress samples are 63.5 mm long. The geometries for these specimens are shown in Table 8.

Table 8. Plane stress fracture specimen geometry, dimensions, triaxiality, and Lode parameter

Test No.	Geometry	Specimen Dimensions	σ^*	θ_L
SG1		Thin smooth specimen Gage length: 5.08 mm Gage width: 1.91 mm Gage thickness: 0.762 mm	0.355	0.943
SG2		Thin large notched specimen Notch radius: 14.29 mm Min notch width: 3.05 mm Gage thickness: 0.762 mm	0.405	0.753
SG3		Thin medium notched specimen Notch radius: 4.76 mm Min notch width: 3.05 mm Gage thickness: 0.762 mm	0.476	0.533
SG4		Thin small notched specimen Notch radius: 0.396 mm Min notch width: 3.05 mm Gage thickness: 0.762 mm	0.574	0.603

The three plane strain geometries are shown in Table 9. They have triaxiality between 0.585 and 0.761. Lode parameter ranges between 0.0293 and 0.0635.

Table 9. Plane strain fracture specimen geometry, dimensions, triaxiality, and Lode parameter

Test No.	Geometry	Specimen Dimensions	σ^*	θ_L
SG11		Thick smooth specimen Gage Length: 4.57 mm Gage Width: 2.03 mm Gage Thickness: 25.4 mm	0.585	0.0635
SG12		Thick large notched specimen Notch radius: 12.7 mm Min notch width: 2.03 mm Gage Thickness: 25.4 mm	0.662	0.0464
SG13		Thick small notched specimen Notch radius: 4.76 mm Min notch width: 2.03 mm Gage Thickness: 25.4 mm	0.761	0.0293

The axisymmetric geometries are designed iteratively, in an effort to match the average stress triaxiality from each plane stress and plane strain specimen. The specimen design is deemed acceptable if the average stress triaxiality is within 5% of the target value. The first iteration of each design is developed using Bridgman's analytical solution for the stress state at the center of a necked sample (Bridgman, 1964). The Bridgman equation is shown in Equation 40, where a is the minimum cross-section radius and R is the required notch radius. This geometry is illustrated in Figure 33 (Bridgman, 1964).

$$\sigma^* = \frac{1}{3} + \ln \left(1 + \frac{a}{2R} \right) \quad 40$$

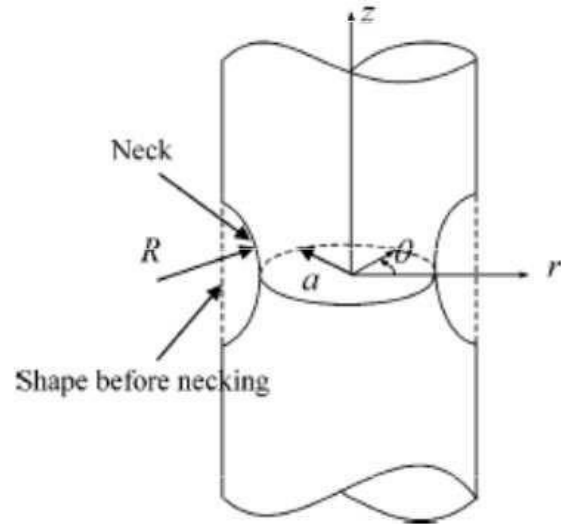

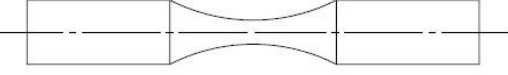
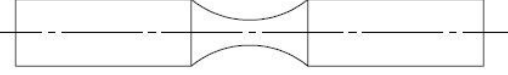
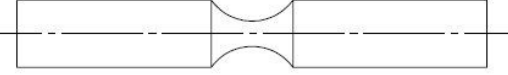
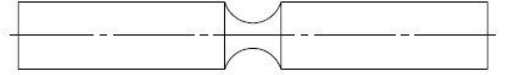
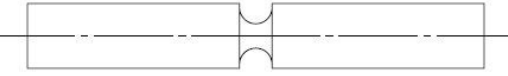


Figure 33. Necked sample geometry as used in Bridgman's equation (Bridgman, 1964)

Due to localization prior to failure, the actual triaxiality will likely not exactly match the value predicted by Bridgman's equation. Through an iterative simulation process, the initial notch radius is modified, and the new geometry is simulated and compared until the triaxiality value predicted by the LS-DYNA simulation results is within 5% of the goal triaxiality. Generally, triaxiality is inversely proportional to notch radius, aiding adjustments to notch radius from one design to the next.

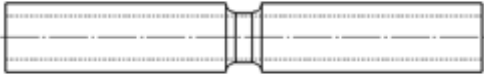
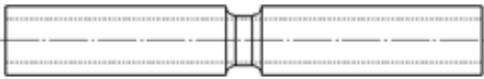
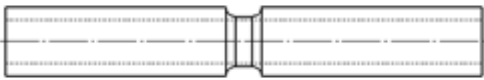
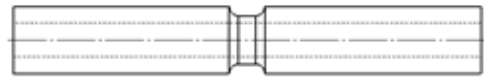
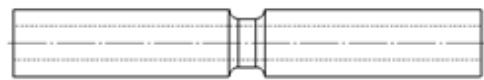
The axisymmetric specimens are designed with to approximately match the stress triaxiality range of the plane stress and plane strain specimens but with a different Lode parameter. These specimens all have a Lode parameter of 1, since the axisymmetric geometry results in two equal principal stresses when loaded in tension. The axisymmetric specimens are shown in Table 10.

Table 10. Axisymmetric fracture specimen geometry, dimensions, triaxiality, and Lode parameter

Test No.	Geometry	Specimen Dimensions	σ^*	θ_L
SG5		Axisymmetric smooth specimen Gage length: 24.13 mm Gage diameter: 4.76 mm	0.378	1.0
SG6		Axisymmetric notched specimen Notch radius: 35.72 mm Gage diameter: 4.76 mm	0.492	1.0
SG7		Axisymmetric notched specimen Notch radius: 17.46 mm Gage diameter: 4.76 mm	0.562	1.0
SG8		Axisymmetric notched specimen Notch radius: 9.53 mm Gage diameter: 4.76 mm	0.651	1.0
SG9		Axisymmetric notched specimen Notch radius: 5.56 mm Gage diameter: 4.76 mm	0.768	1.0
SG10		Axisymmetric notched specimen Notch radius: 3.18 mm Gage diameter: 4.76 mm	0.942	1.0

The combined loading specimens have geometries shown in Table 11. The combination of shear and axial stress results in complex stress states not achievable in uniaxial loading tests. Tension and torsion are combined in LR1 and LR2 to achieve the desired stress state. LR3 is pure torsion. Compression and torsion are combined in LR4 and LR5. The LR4 and LR5 combined loading specimens have a thicker wall to prevent buckling that could induce complex stress states.

Table 11. Combined loading fracture specimen geometry, dimensions, triaxiality, and Lode parameter

Test No.	Geometry	Specimen Dimensions	σ^*	θ_L
LR1		Gage length: 3.125 mm Outer gage diameter: 9.144 mm Inner gage diameter: 7.874 mm	0.251	0.702
LR2		Gage length: 24.13 mm Outer gage diameter: 9.144 mm Inner gage diameter: 7.874 mm	0.147	0.39
LR3		Gage length: 24.13 mm Outer gage diameter: 9.144 mm Inner gage diameter: 7.874 mm	0.000	0
LR4		Gage length: 24.13 mm Outer gage diameter: 9.144 mm Inner gage diameter: 6.350 mm	-0.147	-0.39
LR5		Gage length: 24.13 mm Outer gage diameter: 9.144 mm Inner gage diameter: 6.350 mm	-0.233	-0.55

3.6.2 Combined loading test setup

The combined loading test and axisymmetric tension setup is similar to the flat specimen tension tests but use a v-notched wedge to grip the round specimen. This setup is shown in Figure 34.

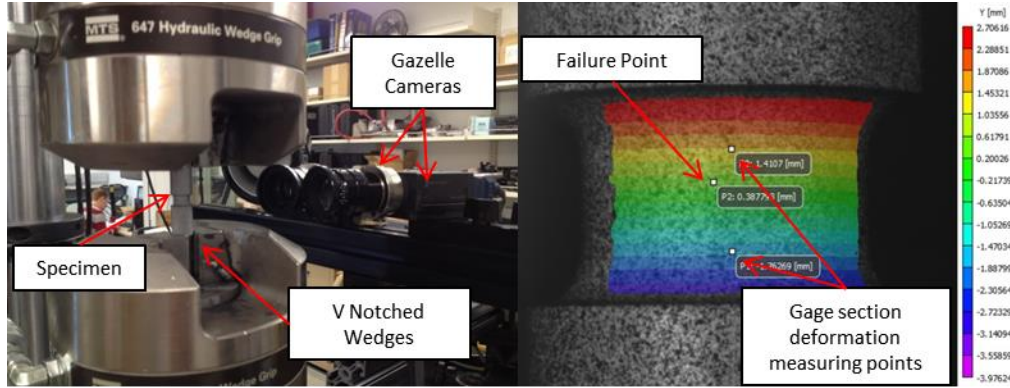


Figure 34. (Left) Axisymmetric tension and combined loading setup. (Right) Initial combined loading measurement points

DIC measurements are made using Gazelle cameras at a frame rate of 2 FPS. The torsional strain is calculated with the same method as the high rate torsion experiments. The axial strain is calculated by the relative axial displacement of the two points used for the rotational measurements. The point of failure is also tracked throughout the test. These points are selected in the initial frame and are shown in Figure 34.

Combined axial tension/compression and torsion loading is used to achieve different states of stress triaxiality (σ^*) and Lode (θ_L) parameters as shown in Equations 41 and 42.

$$\sigma^* = \frac{\frac{\sigma_x}{\tau_{xy}}}{3 \sqrt{3 + \left(\frac{\sigma_x}{\tau_{xy}}\right)^2}} \quad 41$$

$$\theta_L = \sqrt{\frac{\frac{\sigma_x}{\tau_{xy}}}{4 + \frac{\sigma_x}{\tau_{xy}}}} \quad 42$$

These parameters are a function of the ratio of axial stress (σ_x) to shear stress (τ_{xy}). Equations 43 and 44 define the axial and shear stress.

$$\sigma_x = \frac{F}{(r_o^2 - r_i^2)\pi} \quad 43$$

$$\tau_{xy} = \frac{T}{\pi^2 * r_m * t} \quad 44$$

The torque is calculated as a function of the axial force, the desired stress ratio, and the dimensions of the specimen gage section as a function of the outer diameter (OD) and inner diameter (ID) as shown in Equation 45.

$$T = \frac{F * (OD + ID)^2 * (OD - ID)}{4 * \frac{\sigma_x}{\tau_{xy}} * (OD^2 - ID^2)} \quad 45$$

In order to maintain the desired stress ratio for the duration of the combined loading test, the experiments are controlled with a feedback control mode that inputs torque based on the axial force output from the load cell. This prevents increases in the strain rate at failure. The stress ratio and shear strain rate calculated from the DIC are shown in Figure 35. The axial force is generated by inputting an axial displacement ramp at a strain rate of 0.001 s^{-1} .

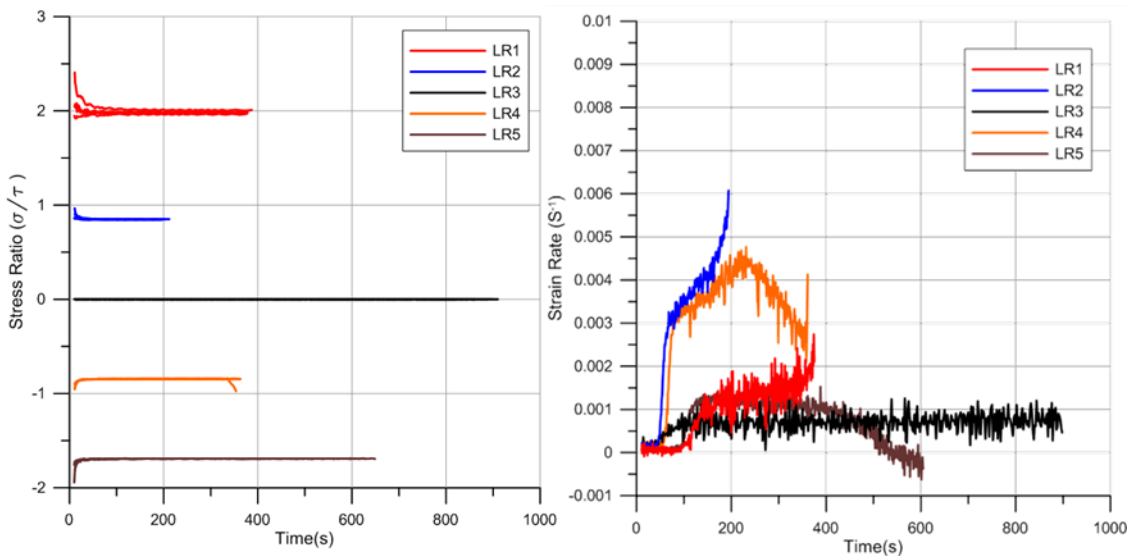


Figure 35. (Left) Stress ratios vs time and (Right) shear strain rate vs time in combined loading tests

3.6.3 Punch experiment setup

Punch experiments are performed at quasi-static and dynamic rates, with several different punch geometries. The geometries of the punch are selected to induce several stress states to evaluate the model's effectiveness with complex stress states. The experiment uses three different punch geometries shown in Figure 36.

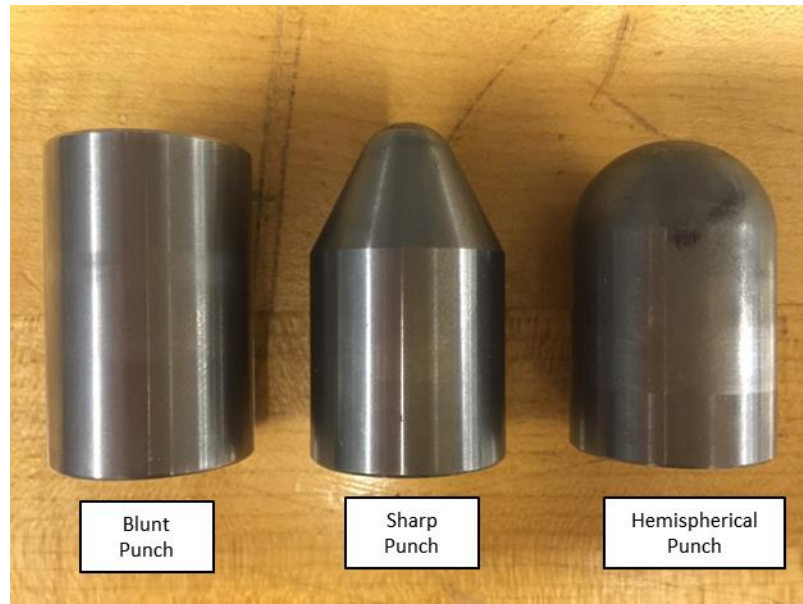


Figure 36. Punch geometries. Blunt Punch (0.79mm radius) Sharp Punch (6.35mm radius) Hemispherical Punch (12.17mm radius)

3.6.3.1 Punch specimen design

The specimen is designed to fit a fixture used in a similar test with titanium by Hammer (2014). The specimen is 50.8 mm in diameter and has six clearance holes for six 8-32 screws in a 40.9 mm bolt circle. Figure 37 shows a detailed drawing of the specimen.

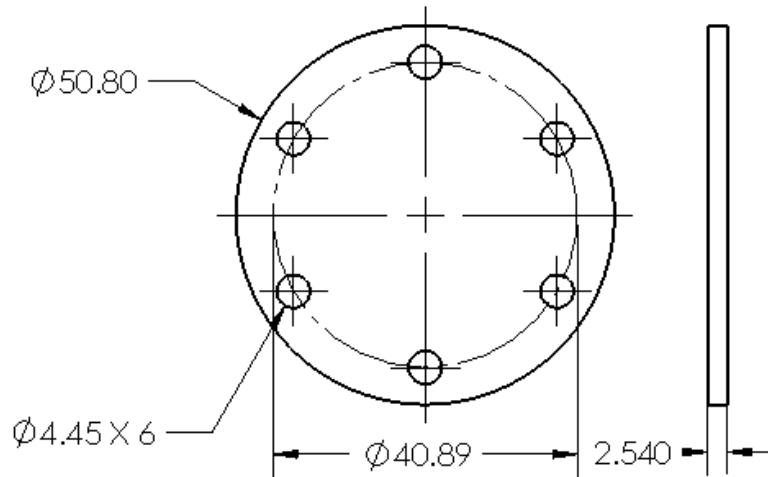


Figure 37. Drawing of punch specimen dimensioned in mm

The thickness of the specimen is determined through a series of LS-DYNA simulations. The simulations are run to estimate the required amount of force at failure, the states of stress on the backside of the specimen at the failed elements, and the failure mode of the specimen. The goals of the design were to keep the punch force below 30 kN, have the desired triaxiality of 0.6 at the failure element on the back surface, and form a plug at failure. The model setup and element stress triaxiality are shown in Figure 38 and Figure 39.

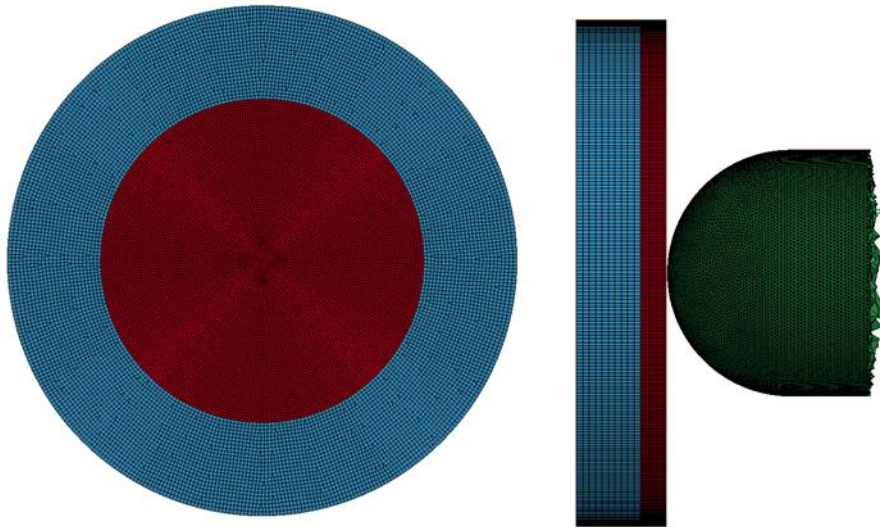


Figure 38. Hemispherical punch test setup in LS-Dyna

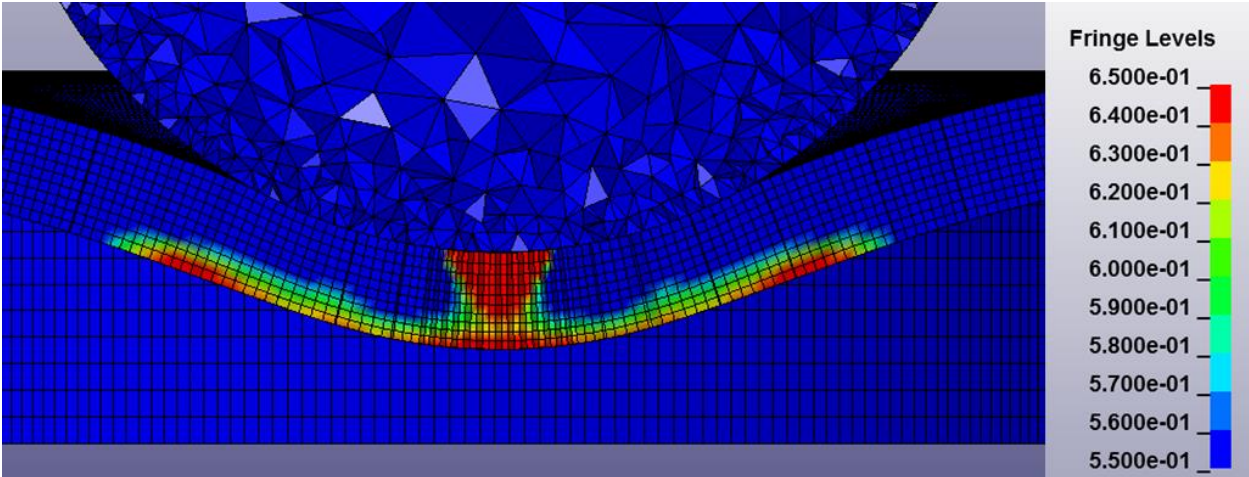


Figure 39. Triaxiality of the elements plotted at the last time step before failure

3.6.3.2 Quasi static punch setup

The quasi-static punch experiments are conducted using a hydraulic load frame. The test uses the same slotted specimen fixture and punch geometries as the dynamic punch but has additional adapters to connect it to the load frame load cell. A picture of the setup is shown in Figure 40, including the camera setup and the respective system labeling. The specimen is loaded at an actuator displacement of 0.01905 mm per second. DIC measurements are made using two different stereo camera setups, both of which consist of two Point Gray Gazelles running at 2 to 4 FPS with a 2048 by 2048 pixel resolution and using 35 mm C-mount lenses. Each camera set is calibrated individually. The camera of each set that has the lowest angle relative to the surface of the specimen is also calibrated to one another. This produces three calibrated stereo camera systems.

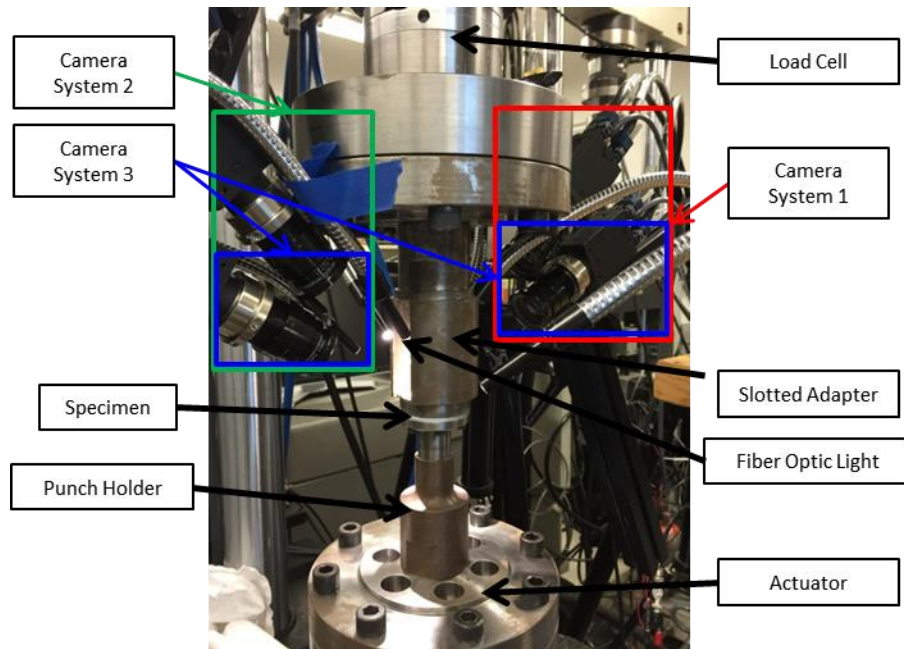


Figure 40. Quasi static punch fixture and DIC setup

The cameras are synced with a 5V TTL pulse generated by a NI-DAQ system with Correlated Solutions VIC-Snap. By using three camera systems, 3D surface data is taken on a much larger portion of the specimen than it is with a single camera set. By having a larger area of view of the specimen surface, tests that have a failure point not directly in the center, such as in the blunt punch case, can be captured in addition to the maximum displacement at the center of the specimen. Such additional data is useful when using the punch test to validate a material model. This is illustrated in Figure 41 where the individual system's area of data is shown relative to the edge of the support fixture. The first principal strain is plotted at the failure frame in a blunt punch test.

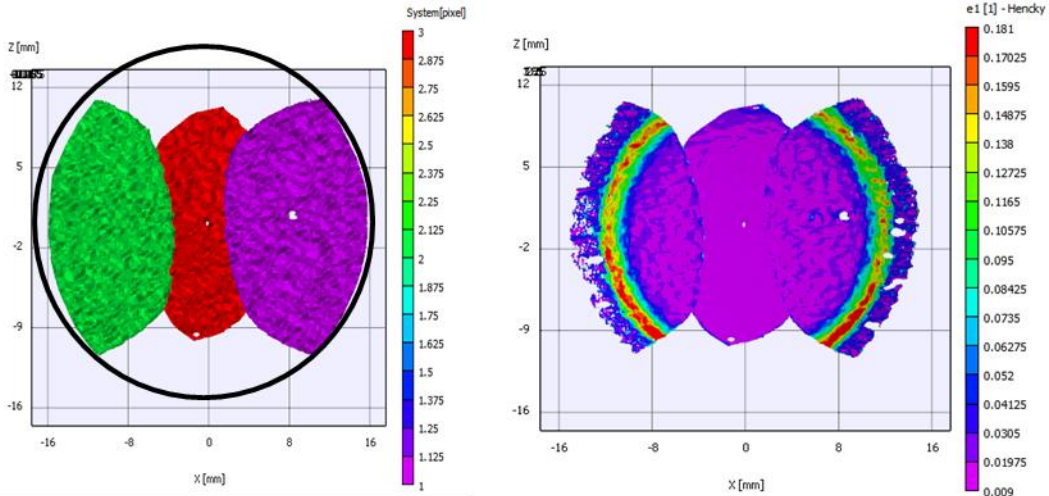


Figure 41. (Left) Areas of capture for each camera system along with approximate edge of fixture support. (Right) Plot of first principal strain where the failure is shown occurring outside central camera system

As with the dynamic tests, the maximum point of displacement and the point of failure are tracked throughout the test in addition to the full field strain plots. The full field strain and displacement plots are used to validate simulation results qualitatively when compared to the experimental results.

3.6.3.3 Dynamic punch setup

The dynamic punch experiment is conducted on a large 50.8 mm diameter Ti64 compression SHB. This bar itself operates the same as the bar used for the compression-rate dependence test. The length of the incident and transmitter bars are 1930.4 mm and the striker bar is 774.7 mm long. The specimen is attached to a specially designed fixture that has two slots cut into opposite sides as seen in Figure 42.

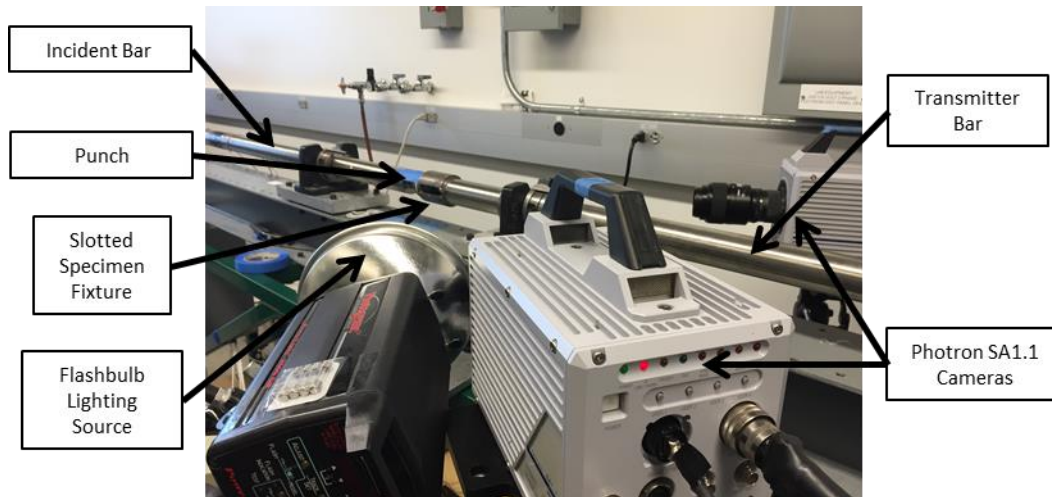


Figure 42. Dynamic punch setup

This fixture allows for stereographic DIC measurements on the back surface of the specimen without significant change in the impedance between the bars to prevent unwanted wave reflections. The design of this fixture is discussed by Hammer (2014). The specimen is clamped to the end of this fixture with a 4130 steel locking ring.

4 Results and discussion

The experimental results from the plastic deformation and ductile fracture behavior of precipitate hardened Inconel 718 are presented in this section. The plastic deformation test program consists of tension, compression and torsion (pure shear) tests, all at various strain rates ranging from 0.0001 s^{-1} to 5000 s^{-1} , and various temperatures ranging from room temperature ($23 \text{ }^{\circ}\text{C}$) to $800 \text{ }^{\circ}\text{C}$ as described in Section 3. The ductile fracture test program consists of several test series including: tensile tests with flat and round notched specimens with various notched geometries, tensile tests with wide notched specimens with various notched geometries, combined loading (axial-torsional) tests, and punch tests of flat specimens with various punch geometries. Tension and compression experiments were also conducted to evaluate P4 anisotropy. Another test series was also performed to measure variation in mechanical properties between the different plate thicknesses.

Additional small diameter punch tests and ultra-high strain rate tests were also conducted as part of this program for Inconel 718 (as well as Ti-6Al-4V and Al 2024) and are published separately as a technical thesis (Spulak, 2022). Further high-rate testing with strain rates up to 6000 s^{-1} was subsequently performed to determine the Taylor-Quinney parameter for Inconel 718 (and also Ti64 and Al 2024) and is also available as a technical thesis (Smith, 2020).

4.1 Strain rate sensitivity test series

Experiments were conducted in uniaxial tension, compression, and torsion to evaluate the effect of strain rate on the plastic response of Inconel 718. The tests were done at room temperature and at various strain rates as summarized in Section 2.2. Low rate tests were performed using a hydraulic load frame as described in Section 3.3 while high rate tests were performed using SHB's as described in Section 3.5. The specimens were fabricated in the rolling direction of P4.

Three specimen replicates were typically tested at each strain rate. True stress vs true strain curves are show for all test samples are shown in 1)a)i)(1)(a)A.

4.1.1 Tension strain rate sensitivity

Tension tests were performed at nominal strain rates of 0.0001 s^{-1} , 0.01 s^{-1} , 1 s^{-1} , 500 s^{-1} , and 2000 s^{-1} with representative data shown in Figure 43. A significant strain hardening is observed from about 1100 MPa yield stress to around 1600 MPa at ultimate stress at a strain rate of 0.0001 s^{-1} . The ultimate stresses occur around 22.5% strain at 0.0001 s^{-1} , 0.01 s^{-1} and around 18.5% at 1 s^{-1} , 500 s^{-1} , and 2000 s^{-1} .

In addition to a degree of rate dependence, the data from this test series presents another interesting trend with regard to plastic flow behavior when examining the data from 0.01 s^{-1} and 1.0 s^{-1} in Figure 43. Starting around 11% strain, the rate of strain hardening – i.e. the slope of the true stress/true strain curve – is lower in the 1.0 s^{-1} test than in the 0.01 s^{-1} case. Despite a lower yield stress, the slower test results in a higher ultimate stress. This result suggests that the strain hardening behavior varies slightly with strain rate, in addition to the typical increase in stress with increasing strain rate.

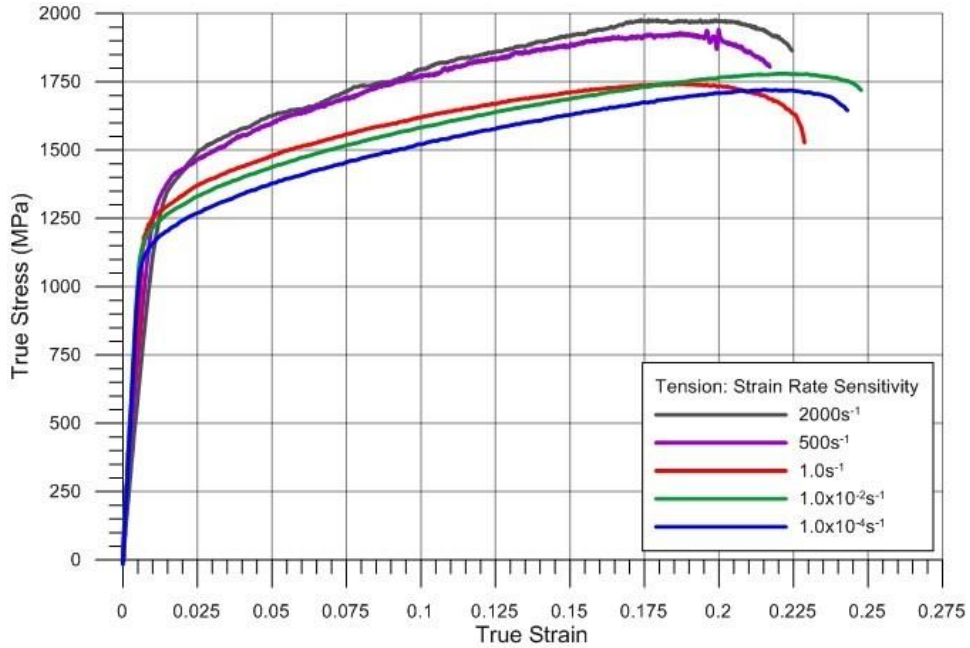


Figure 43. True stress-strain strain rate sensitivity in tension

The true stress at 5% true strain is plotted in Figure 44 for each tension test replicate at each nominal strain rate to further quantify the strain rate sensitivity. True stress increases with increasing strain rate, rising from roughly 1400 MPa at 0.0001 s^{-1} to around 1650 MPa at 2000 s^{-1} .

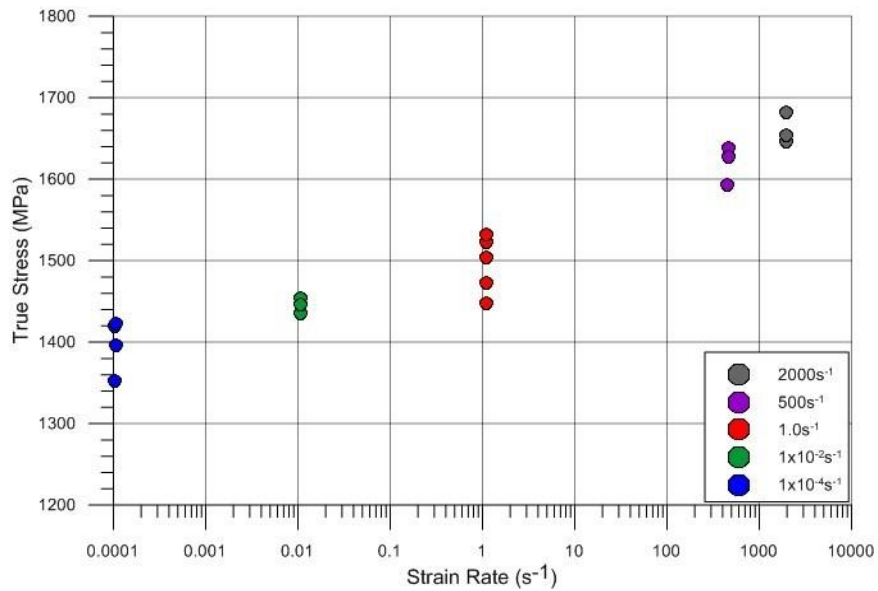


Figure 44. True stress at 5% strain versus strain rate in tension

4.1.2 Compression strain rate sensitivity

Compression tests were performed at nominal strain rates of 0.0001 s^{-1} , 0.01 s^{-1} , 1 s^{-1} , 1000 s^{-1} , 2000 s^{-1} , and 5000 s^{-1} . Representative data from compression experiments at various strain rates on specimens fabricated in the rolled direction are shown in Figure 45.

In the low rate experiments (0.0001 , 0.01 , and 1 s^{-1}), yield occurs around 1200 to 1250MPa. The plastic flow behavior is similar to that seen in tension. The material exhibits significant strain hardening in compression, with stress rising roughly 700 MPa by 30% strain. Comparing experiments conducted at a nominal strain rate of 0.01 s^{-1} and 1.0 s^{-1} show that these two samples yield at approximately the same stress level, and their strain hardening rates are nearly identical between yield and a true strain of 7.5%. The strain hardening rate decreases at true strains greater than 7.5%, resulting in a lower true stress level around 13.5% true strain. The plastic flow behavior is sensitive to changes in strain rate, particularly strain rates greater than 1.0 s^{-1} . The strain hardening rate decreases as strain increases when compared to that at 0.0001 s^{-1} and 0.01 s^{-1} .

Rates above 1000 s^{-1} show a dramatic increase in stress compared to the increase between the lower rates as illustrated in Figure 46. At 2000 s^{-1} stress at 5% strain increases to 1726 MPa from 1576 Mpa, the stress at a strain rate of 1000 s^{-1} . At a strain rate of 5000 s^{-1} the stress at 5% strain increase further to 2208 MPa, a 46% increase from the 1000 s^{-1} experiment.

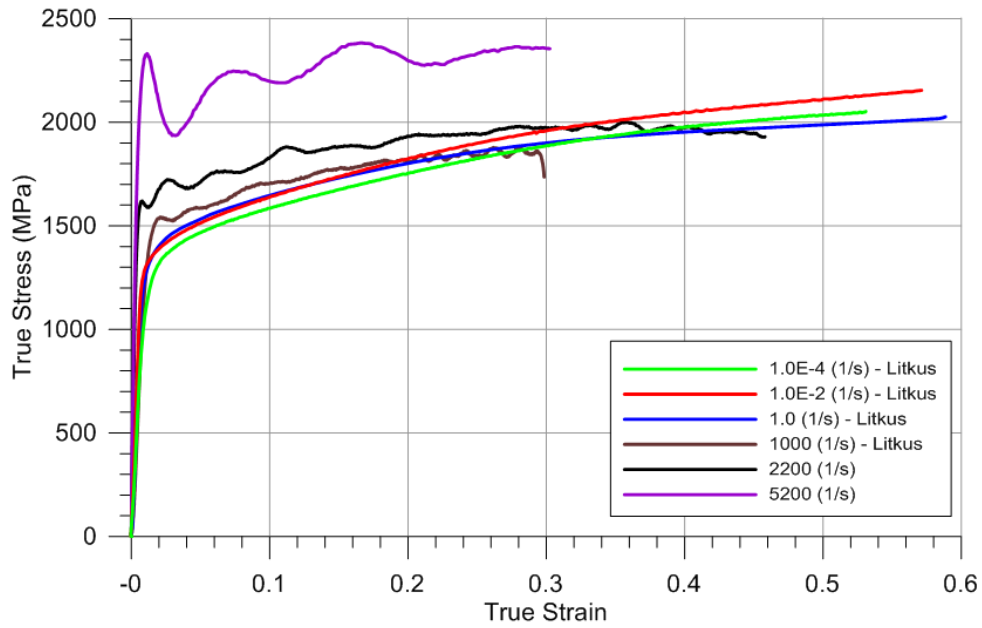


Figure 45. Compression stress-strain curves from tests at different strain rates at room temperature

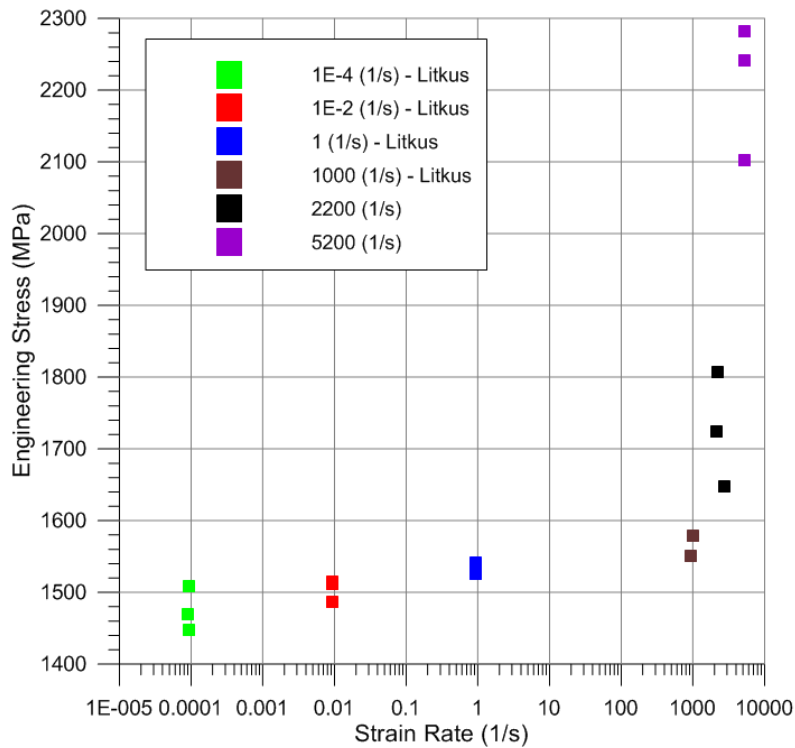


Figure 46. Engineering stress versus strain rate at 5% strain for all strain rates tested in compression

4.1.3 Torsion strain rate sensitivity

Torsion strain rate experiments are conducted at nominal strain rates 0.0001 s^{-1} , 0.01 s^{-1} , 1 s^{-1} , 500 s^{-1} , and 2000 s^{-1} . Experiments at rates of 1 s^{-1} and below are conducted on a torsional load frame as described in Section 3.3.3 and testing on rates above that are completed utilizing a torsion SHB as described in Section 3.5.3. Representative engineering shear-stress versus engineering shear-strain curves at each strain rate are presented in Figure 47.

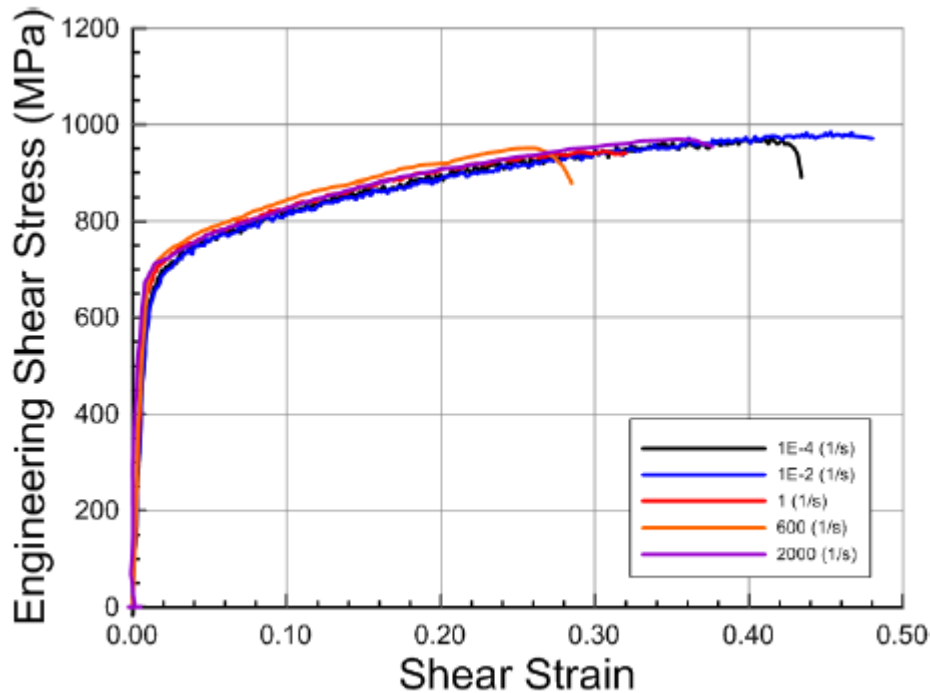


Figure 47. Shear stress-strain curves from tests at different strain rates at room temperature

Shear stress levels show no obvious or significant strain rate sensitivity at the strain rates examined. Strain rate sensitivity is not observed when examining the shear stress for each specimen at 2.5%, 7.5%, and 12.5% strain as shown in Figure 48.

Test results also show a large spread of failure strains at each rate and no significant dependence on the strain rate could be determined.

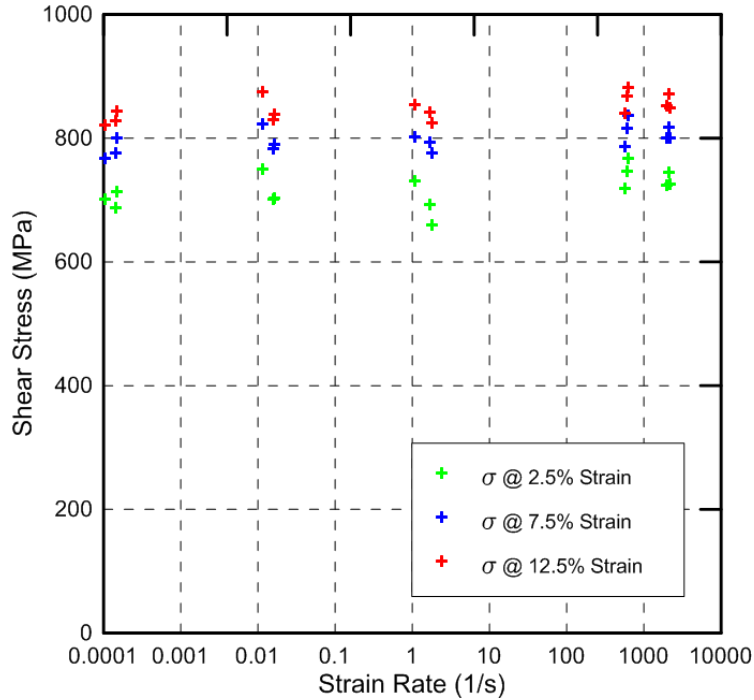


Figure 48. Shear stress versus log scale strain rate for all the torsion strain rate sensitivity experiments at 2.5%, 7.5%, and 12.5% strain

4.1.4 Comparison of strain rate sensitivity in tension and compression

Figure 49 presents effective stress versus equivalent plastic strain for representative experimental data from tension and compression experiments at a nominal strain rate of 1.0 s^{-1} . These data suggest that the material response is very similar in both tension and compression.

Figure 50 compares true stress versus strain rate data for experiments in tension and compression at 10% true strain. The material shows greater rate sensitivity in tension than compression. At low strain rates, the stress in compression is greater than that in tension, and at high rates, the tension and compression data fall in the same stress range.

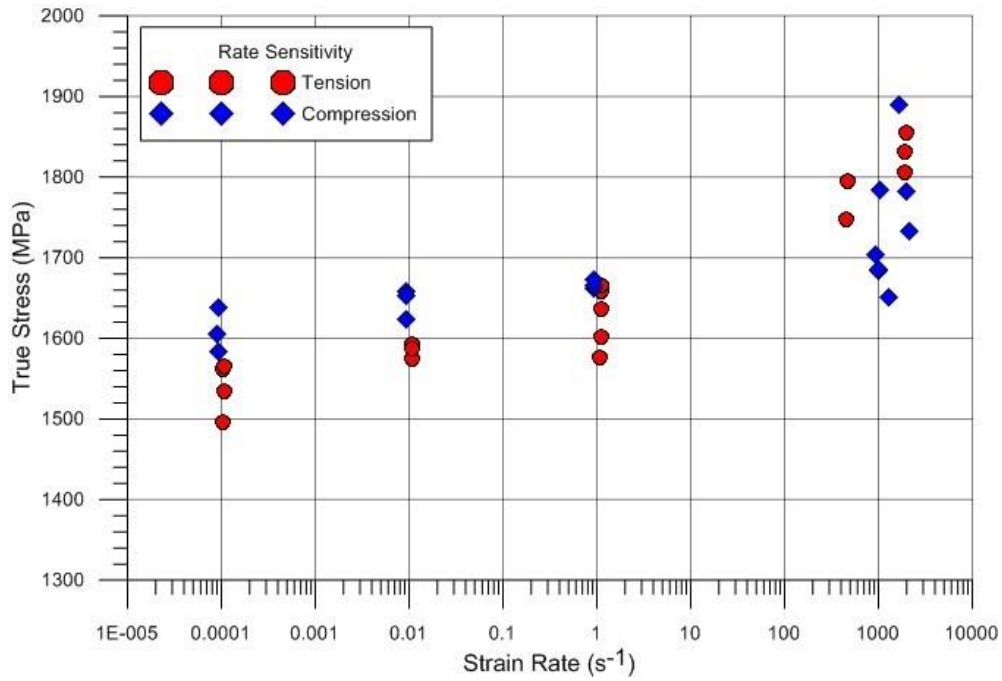


Figure 49. Comparison of rate sensitivity data for tension and compression. True stress at 10% true strain versus strain rate

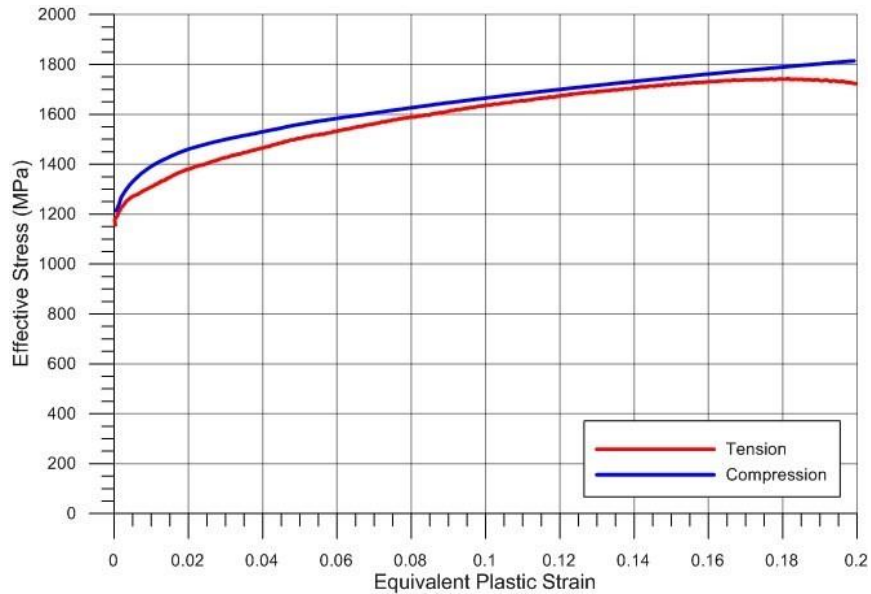


Figure 50. Effective stress versus equivalent plastic strain data for the tension and compression loading conditions at the 1.0 s⁻¹ strain rate

4.2 Temperature sensitivity test series

Tension, compression, and torsion tests were conducted at temperatures of 23 °C (room temperature), 200 °C, 400 °C, 600 °C, and 800 °C at a nominal strain rate of 0.001 s^{-1} as described in Section 3.4. All specimens were fabricated from the rolling direction of P4. Additional temperature tests were conducted in tension at a strain rate of 1 s^{-1} . Results for all temperature sensitivity tests are shown in Appendix B.

4.2.1 Tension temperature sensitivity

Experimental temperature dependence results in tension at a strain rate of 0.001 s^{-1} are presented in the true stress versus true strain curves for each temperature shown in Figure 51. The yield strength, ultimate stress, and failure strain are measured from these results and tabulated at each temperature in Table 12.

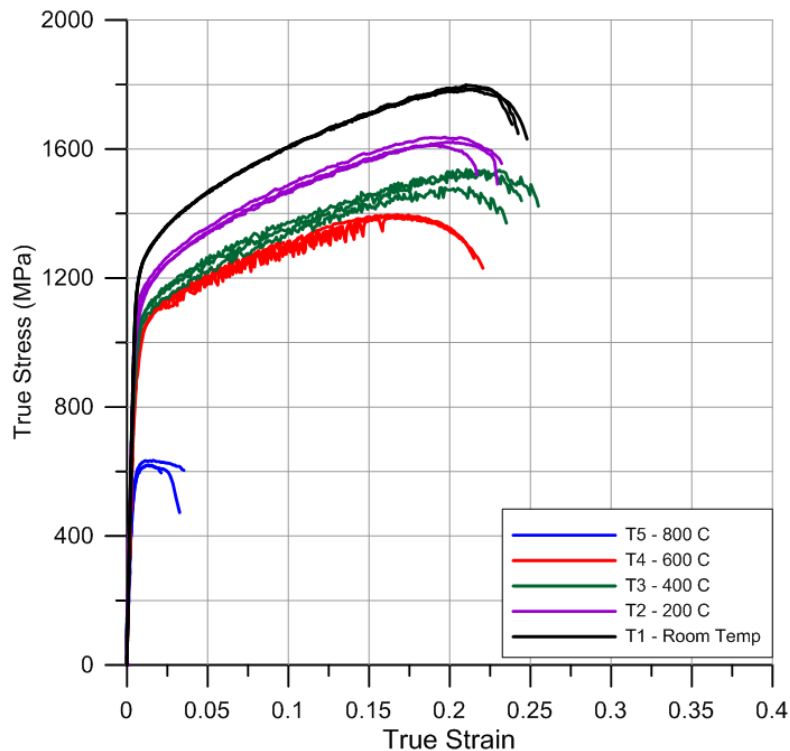


Figure 51. Stress vs. strain at a strain rate of 0.001 s^{-1} over a range of temperatures

Table 12. Average yield strength, ultimate strength, and failure strain at tested temperatures in tension at a strain rate of 0.001 s^{-1}

Temperature	Average True Yield Strength (MPa)	Average True Ultimate Strength (MPa)	Average True Strain at Failure
23 °C	1206	1792	0.243
200 °C	1102	1623	0.2262
400 °C	1037	1517	0.2448
600 °C	1004	1392	0.2167
800 °C	599	624	0.0297

Tensile tests were also performed over the range of temperatures at a strain rate of 1 s^{-1} as shown in Figure 52. Inconel 718 exhibits a reduction in strength with increasing temperature for both rates tested. However, the material shows a drastically different failure strain behavior at 800 °C between the tests performed at the strain rates 0.001 s^{-1} and 1 s^{-1} . At 0.001 s^{-1} , there is marked reduction in ductility as the failure strain drops to approximately 0.03. In contrast, at 1 s^{-1} , the ductility increases substantially from the room temperature tests as the material ruptures at a failure strain of about 0.35.

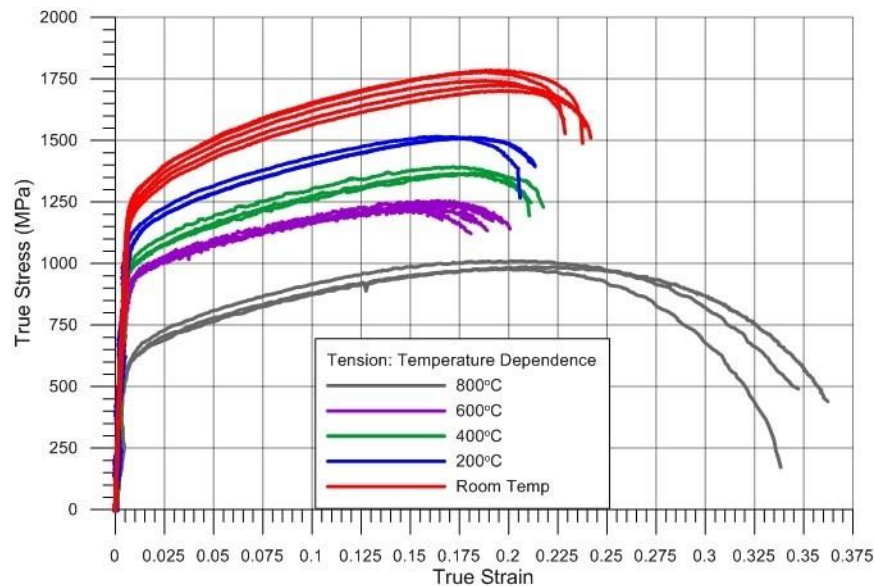


Figure 52. Tensile stress strain curves at different temperatures at a strain rate of 1 s^{-1}

The reduction in ductility of Inconel 718 at low strain rates has also been observed by others. Booker and Booker noted that for strain rates in the range of $1e-6$ to $1e-3$ s^{-1} , ductility measures for Inconel 718 fell to 10% or less at around 700 °C. As the temperature increases beyond 800 °C the ductility again increased (Booker & Booker, 1980). Dynamic embrittlement has been observed for Inconel 718 and other nickel based alloys, which is promoted at high temperatures as oxygen diffuses into the grain boundaries producing local decohesions, leading to early rupture (McLouth, et al., 2021). However, as the strain rate increases there is less time for diffusion to occur. This may be one reason why the test results at 800 °C presented herein show a brittle response at 0.001 s^{-1} but not at 1 s^{-1} . Another factor contributing to the lack of brittleness observed at 800 °C in the 1 s^{-1} may be the additional local temperature rise induced in the specimen from the Taylor-Quinney conversion of plastic work to heat. At 0.001 s^{-1} there is a negligible temperature increase from plastic heating as there is ample time for heat dissipation whereas at 1 s^{-1} significant local temperature rise occurs as the process occurs much faster without time for diffusion of the added heat from plastic work. Temperature rises above 150 °C have been observed at 1 s^{-1} during testing of Inconel 718 at OSU as part of this project (Smith, 2020).

Serrated flow can be seen in the tension tests conducted at 400°C and 600°C. This can be attributed to dynamic strain aging and the Portevin–Le Chatelier effect. Garat et al. (2008) conducted tensile tests on Inconel 718 at the same strain rate at 650°C and observed jerky flow. The fluctuations present in the stress-strain curve tension test at 600°C shown in Figure 53 migrate to different areas of high strain localization in the specimen gage section. The two black dots labeled A and B on the load curve correspond to where the DIC measurements are taken.

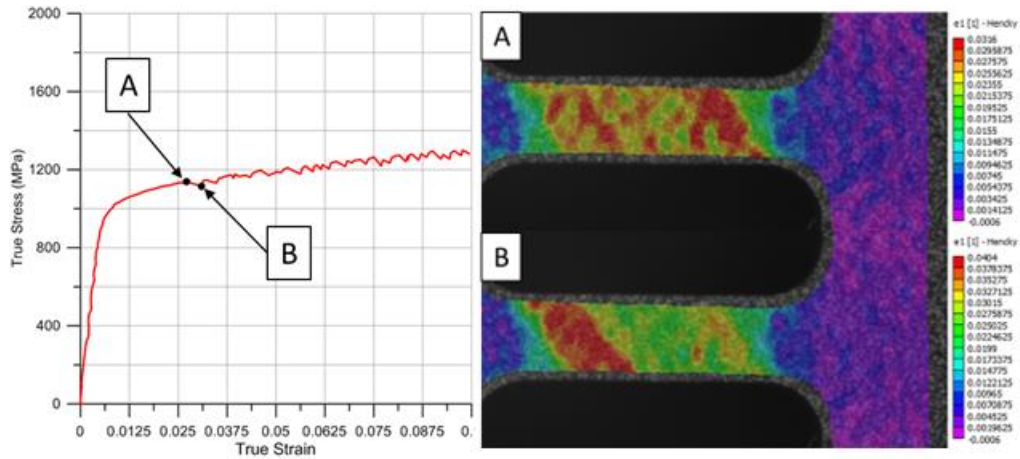


Figure 53. Serrated flow in tension tests at 600°C

4.2.2 Compression temperature sensitivity

Figure 54 presents true stress versus true strain curves for each temperature tested in compression. The average yield strength calculated by a 0.2% offset at each temperature is tabulated in Table 13.

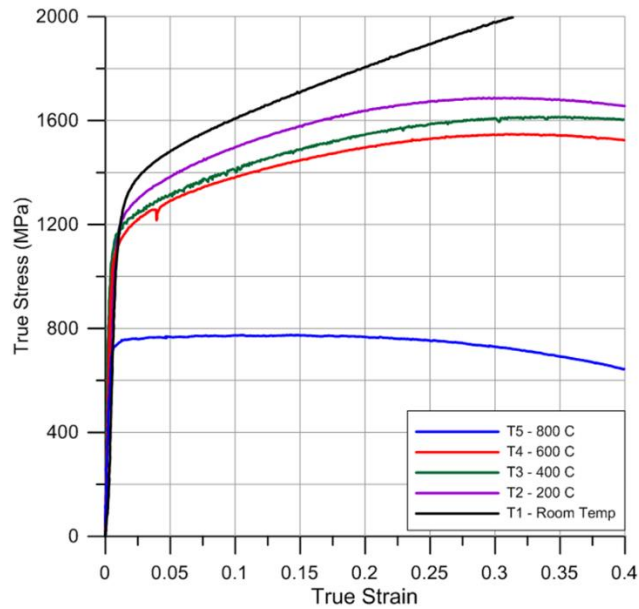


Figure 54. True stress versus true strain for compression specimens for all temperatures conducted at a strain rate of 0.001 s^{-1}

Table 13. Average true yield strength for all temperatures test in compression at 0.001 s^{-1}

Temperature	Average True Yield Strength (MPa)
23 °C	1194
200 °C	1131
400 °C	1123
600 °C	1034
800 °C	701

The compression results show that Inconel 718 exhibits a decreasing strength, which is not linearly proportional to the increase in temperature. The yield strength decreases 63 MPa from room temperature to 200 °C. The decrease between 200°C and 400°C is much smaller. A large decrease of 89 MPa is seen between 400 °C and 600 °C and a much larger decrease of 396 MPa is seen between 600 °C and 800 °C. Changes in the plastic behavior can also be observed in Figure 54. At room temperature, the plastic curve hardens at a nearly constant rate. Between 200 °C and 600 °C, the material hardens less and reaches its ultimate stress between strain values of 0.30 and 0.35. At 800 °C, the material exhibits almost no hardening after the yield point and displays nearly purely plastic behavior before softening at strain values above 0.2.

4.2.3 Torsion temperature sensitivity

Experimental results for the temperature dependence behavior in torsion are presented in Figure 55. The figure shows the effective stress versus the equivalent strain for the three tests at each temperature at a strain rate of 0.001 s^{-1} . At each temperature, the average yield strength, ultimate stress, and strain at failure are extracted from the data and presented in Table 14.

Table 14. Average measured material properties at tested temperatures in torsion at 0.001 s^{-1}

Temperature	Average Effective Yield Strength (MPa)	Average Effective Ultimate Stress (MPa)	Average Equivalent Shear Strain at Failure
23 °C	1041	1547	0.1922
200 °C	948	1416	0.1933
400 °C	937	1412	0.2948
600 °C	872	1326	0.4977
800 °C	377	415	0.0254

Figure 55 depicts the decrease in strength as the temperature increases, as well as changes in the ductility of the material. While the strength decreases with temperature, this effect is not proportional to the increase in temperature as seen from the relative decrease in yield strength between temperatures. As tabulated in Table 14, the yield strength decreases by 93 MPa between 200 °C and room temperature, while only decreasing a further 11 MPa between 200 °C and 400 °C. A slightly larger decrease of 65 MPa is seen between 400 °C and 600 °C, and a very large decrease of 593 MPa is measured between 400 °C and 800 °C. Increasing ductility with temperature is observed in the tests from RT to 600 °C. Between 200 °C and 400°C, the failure strain increases by 0.10 (mm/mm). The failure strain further increases 0.20 (mm/mm) between 400 °C and 600 °C. Unexpectedly, the material becomes very brittle at 800°C. The specimen fails at a strain of 0.025 (mm/mm), a decrease of 0.47 (mm/mm) from the failure strain at 600 °C.

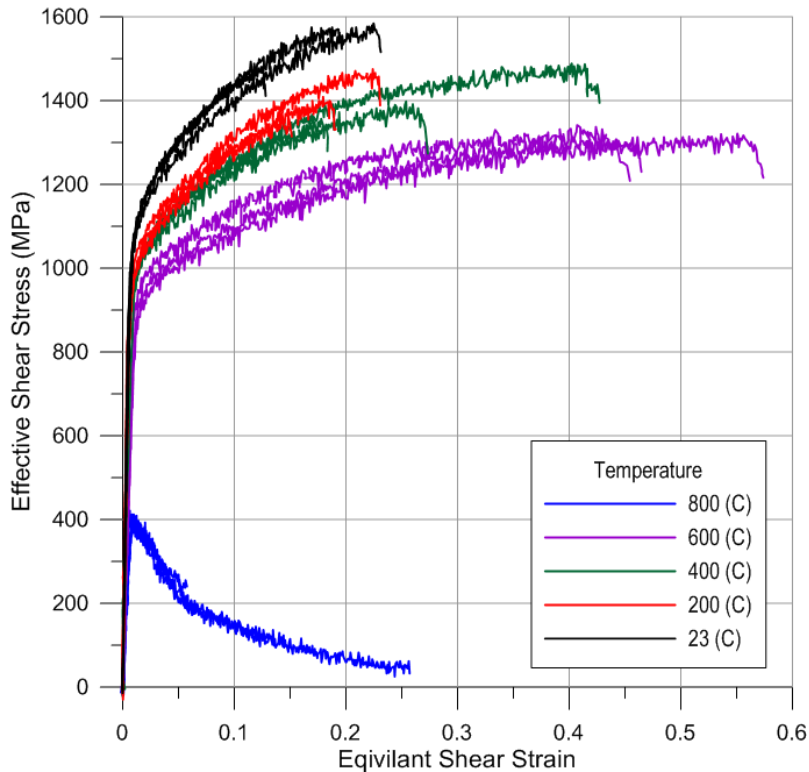


Figure 55. Effective stress versus equivalent strain for torsion experiments at various temperatures and a strain rate of 0.001 s^{-1}

4.2.4 Comparison of temperature sensitivity in tension and compression

A comparison of the true stress versus true strain temperature dependence results in compression and tension at a strain rate of 0.001 s^{-1} is made in Figure 56. The figure shows similar hardening behavior and stress levels for the tests in compression and tension at room temperature and $200 \text{ }^{\circ}\text{C}$. As the temperature increases however, the material becomes more sensitive to the temperature increase in tension than in compression. At $400 \text{ }^{\circ}\text{C}$, a large decrease is seen in tension, as the yield strength remains 92 MPa higher in compression than tension. At $800 \text{ }^{\circ}\text{C}$, the yield strength becomes 115 MPa greater in compression than in tension. The difference in the ductility at $800 \text{ }^{\circ}\text{C}$ is also observed. In compression, the plastic flow appears very smooth with no failure occurring up to the tested strain value of 0.50 , while in tension the material becomes brittle and fails at a very low strain. This brittleness is also observed at $800 \text{ }^{\circ}\text{C}$ in the torsion results. In torsion, a 63% decrease in the yield strength as compared to 50% and 40% in tension and compression, is observed. Below $800 \text{ }^{\circ}\text{C}$, the material is slightly less sensitive to temperature in torsion than tension. At $200 \text{ }^{\circ}\text{C}$, $400 \text{ }^{\circ}\text{C}$, and $600 \text{ }^{\circ}\text{C}$ the yield strength decreases 8.9% , 9.9% ,

and 16.2% as compared to 8.6%, 14.0%, and 16.7% in tension respectively. Both tension and torsion are more sensitive to temperature than compression. The compression tests show a 3.7%, 5.4%, and 11.3% decrease in yield strength at 200 °C, 400 °C, and 600 °C respectively.

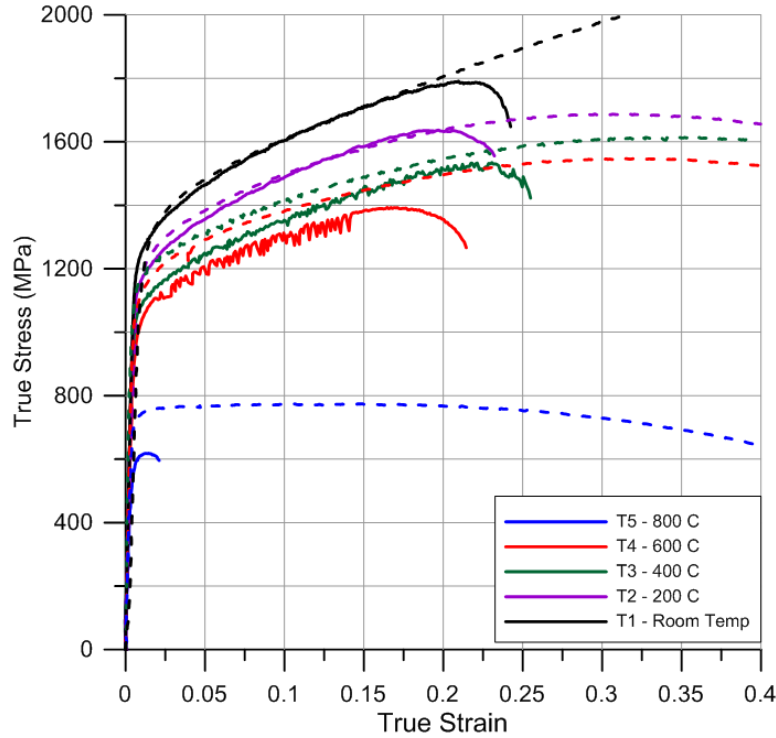


Figure 56. True stress versus true strain curves at each temperature for both the tension (solid line) and compression (dashed line)

4.3 Anisotropy

4.3.1 Tension anisotropy

Representative experimental results for the anisotropy series are presented in Figure 57. These data show moderately different behavior in between the $\pm 45^\circ$ directions and the rolled/transverse directions. The yield stress is approximately 1075 MPa for the former and 1175 MPa for the latter. This trend holds for the ultimate stress where the $\pm 45^\circ$ directions average roughly 1600 MPa and rolled/transverse directions about 1725 MPa. One interesting difference is in the strain at onset of localization and failure. The rolled direction sample localizes around 18.5% strain and fails just past 22.5% strain. The other directions all localize around 21% strain and fail at approximately 24.5% strain.

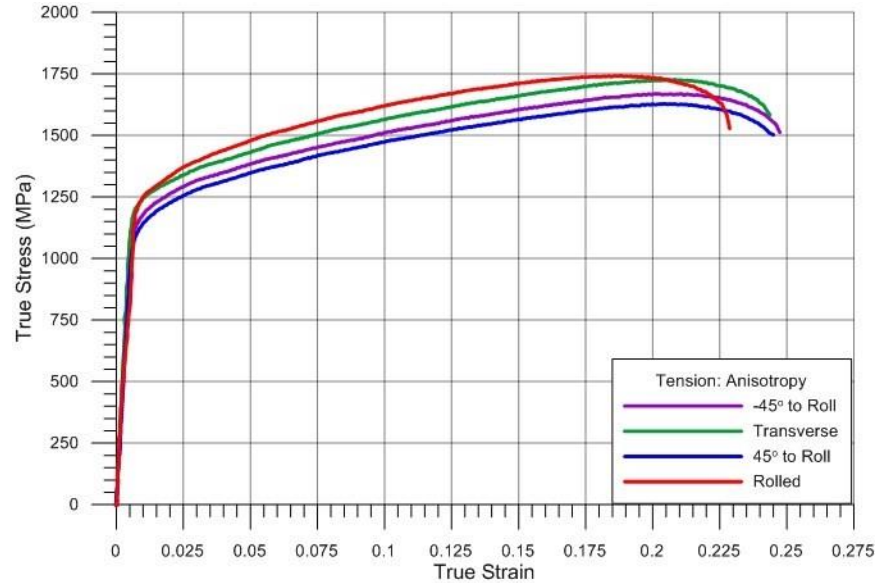


Figure 57. Stress strain curves from tensile tests at different orientations (strain rate 1 s^{-1})

4.3.2 Compression anisotropy

Representative data from experiments on specimens fabricated in each direction is presented in Figure 58. In this plot, the $\pm 45^\circ$ directions show similar behavior, as do the through thickness and transverse direction. The rolled direction data is interesting because it yields at roughly the same stress as the transverse and through directions, but exhibits less strain hardening. In fact, the strain hardening rates between yield and 15% true strain are roughly equal for all directions except the rolled. At true strain larger than 15%, the transverse and through direction strain hardening rate is less than that of the $\pm 45^\circ$ directions. The stress at high strains (true strain greater than 45%) is nearly the same for all orientations.

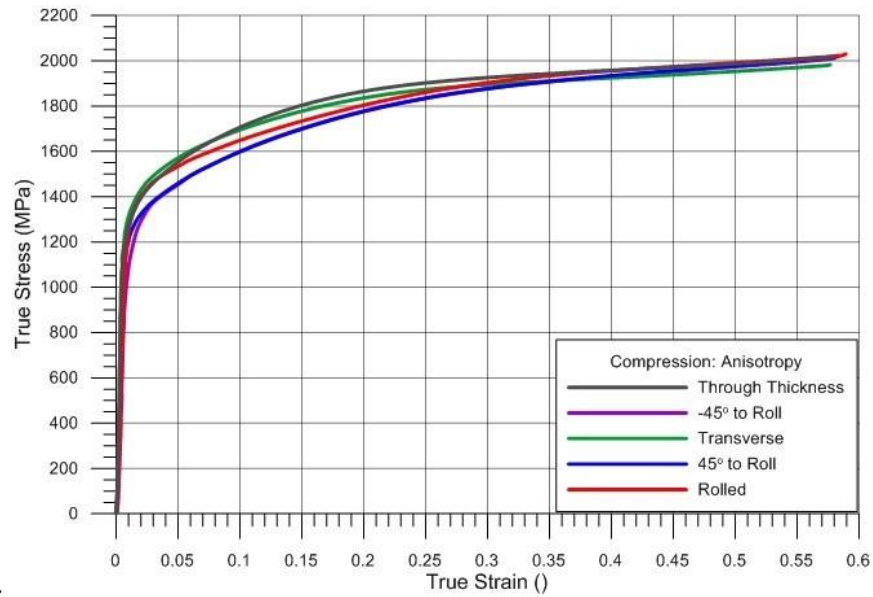


Figure 58. Stress strain curves from compression tests at different orientations (strain rate 1 s^{-1})

4.3.3 Comparison of tension and compression anisotropy

Figure 59 presents representative effective stress versus equivalent plastic strain data for tension and compression experiments conducted on specimens fabricated from different directions through the P4 (12.7 mm thick) stock. This data suggests subtle anisotropy and potentially differences in flow behavior between the loading configurations.

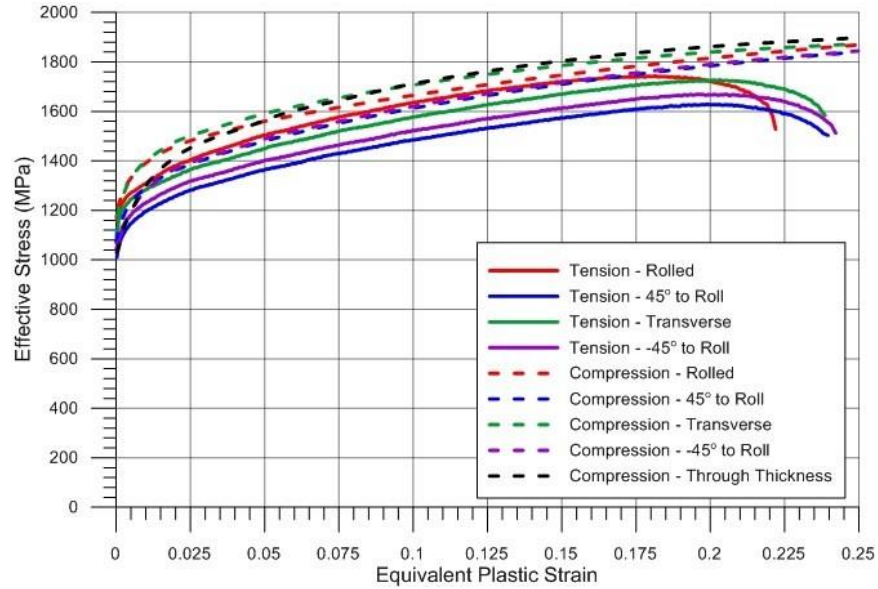


Figure 59. Effective stress versus equivalent plastic strain data for specimens with various plate orientations

Figure 60 plots the average effective stress at 10% equivalent plastic strain for each specimen orientation. The error bars reflect the 95% confidence intervals. The chart suggests that the anisotropy present in both tension and compression is statistically significant. Specifically, the stresses in the $\pm 45^\circ$ direction are less than those in the rolling direction. Average transverse stress is less than the rolling direction stress in tension; however, the opposite is true in compression. This trend suggests an asymmetry between tension and compression.

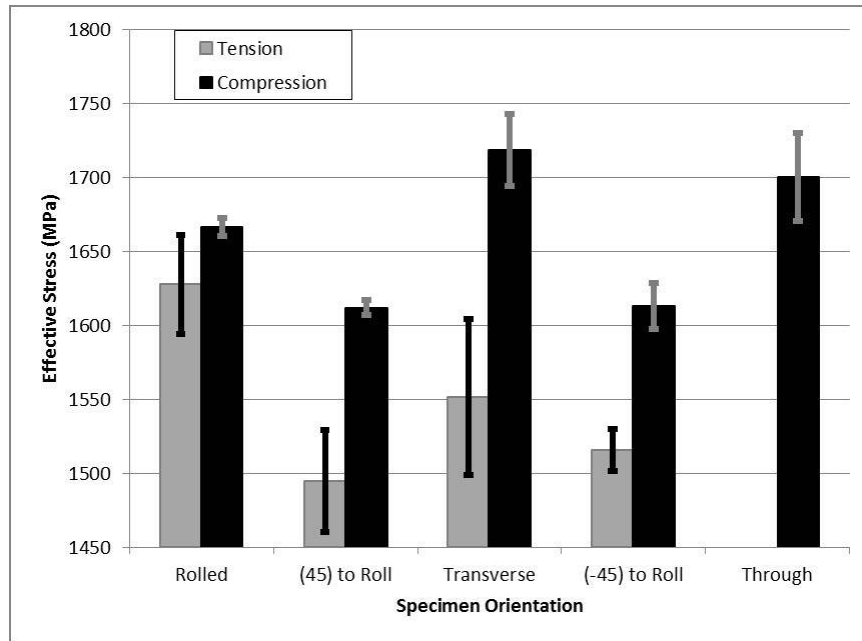


Figure 60. Effective stress at 10% equivalent plastic strain and specimen orientation with 95% confidence intervals

4.4 Plate thickness experiments

Five different plate stock thicknesses are examined to evaluate the effect of plate thickness on the material properties. The plate thicknesses corresponding to each plate designation are P5: 1.27 mm, P1: 2.03 mm, P2: 3.17 mm, P3: 6.35 mm, and P4: 12.7 mm. All plates have a similar material composition, as shown in Table 1. The plates underwent the same precipitation hardening procedure as described in Table 2. Experiments are conducted for all plates in tension. P1, P2, P3, P4 are examined in compression as P1 is too thin for fabrication of compression specimens.

4.4.1 Tension experiments for various plate stock thickness

Experiments are conducted on tension specimens from each plate in the rolling direction, at strain rates of 0.001 s^{-1} and 500 s^{-1} . The low rate tests are conducted as described in Section 3.3.1. The high rate test procedure is described and shown in Section 3.5.1. The results for each plate at the static and dynamic strain rate are shown in Figure 61 and Figure 62 respectively.

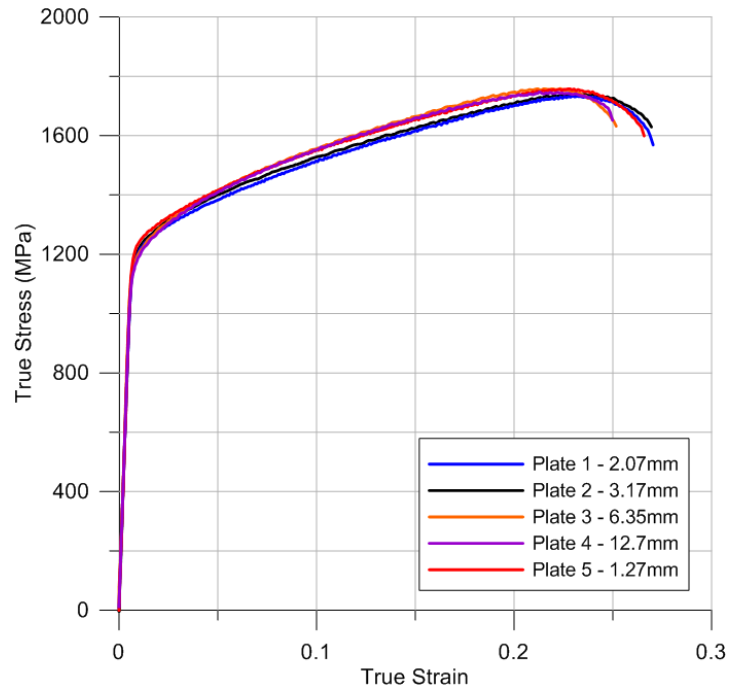


Figure 61. Representative true stress versus true strain curve for each plate conducted at a strain rate of 0.001 s⁻¹

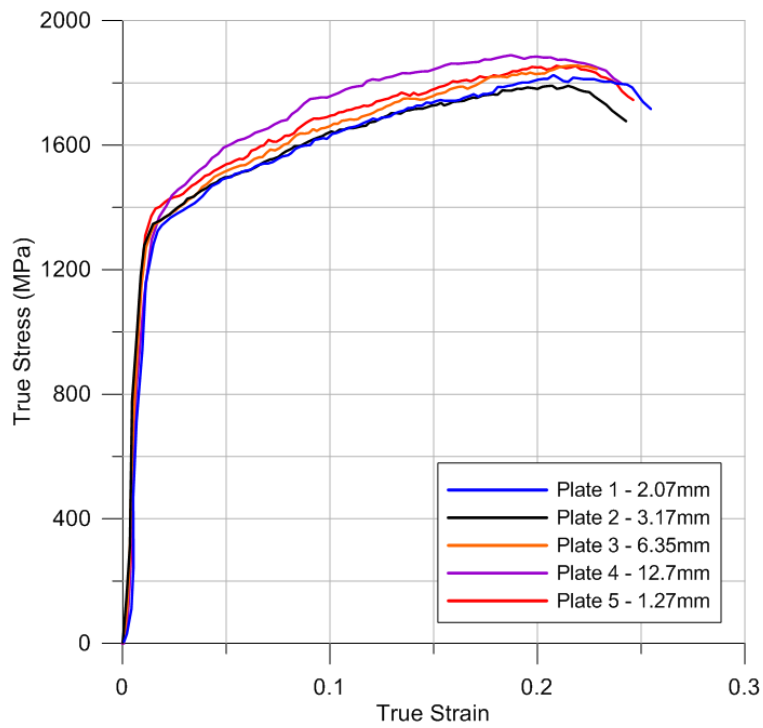


Figure 62. Representative true stress versus true strain curve for each plate conducted at a strain rate of 500 s⁻¹

All results for each plate at each strain rate are presented in Appendix 1)a)i)(1)(a)D. The results show a noticeable difference in the stress levels between the specimens from difference plates in both the static and dynamic cases. The ultimate stresses between the plates in the dynamic and static cases are presented in Figure 63, along with error bars representing the 95% confidence interval.

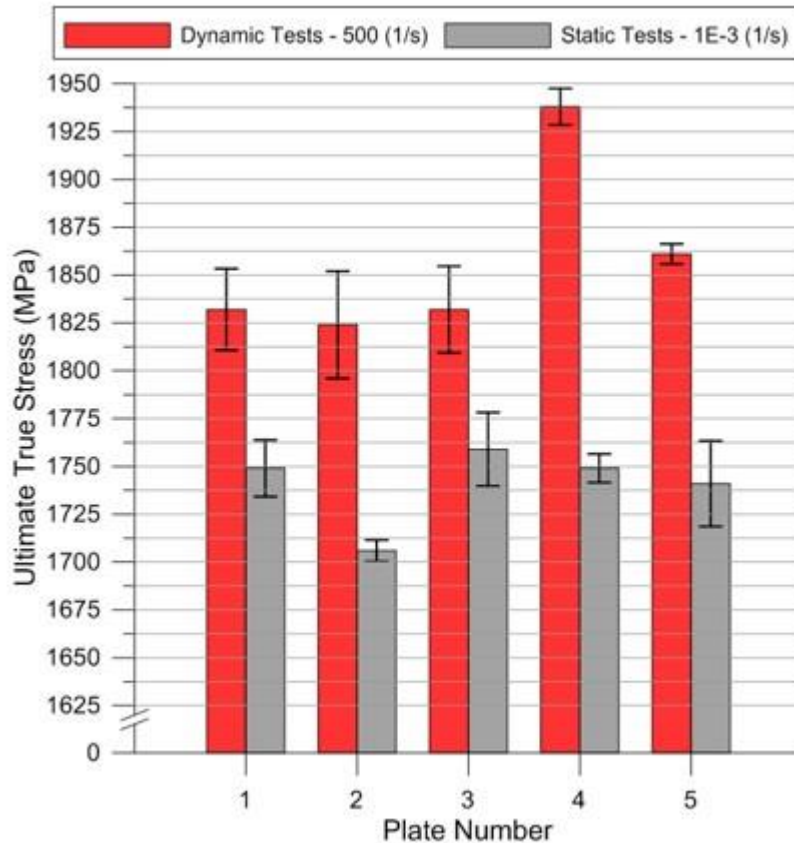


Figure 63. Average ultimate stress for each case in tension at both static and dynamic strain rates with error bars representing the 95th% confidence interval

The results show statistically significant ultimate strength sensitivity to the plate stock. The sensitivity is not directly related to thickness. In the static case, P2 has the lowest ultimate stress at 1706 MPa, 2.52% lower than the average of the four other plates. In the dynamic case, P4 also shows an ultimate stress of 1938 MPa, which is 95 MPa higher than in any of the other plates. P1, P2, P3, and P5 have an average of ultimate strength 1837 MPa and individual average ultimate strengths within their 95% confidence intervals. The failure strain for each plate at the dynamic and static rate is presented in Figure 64.

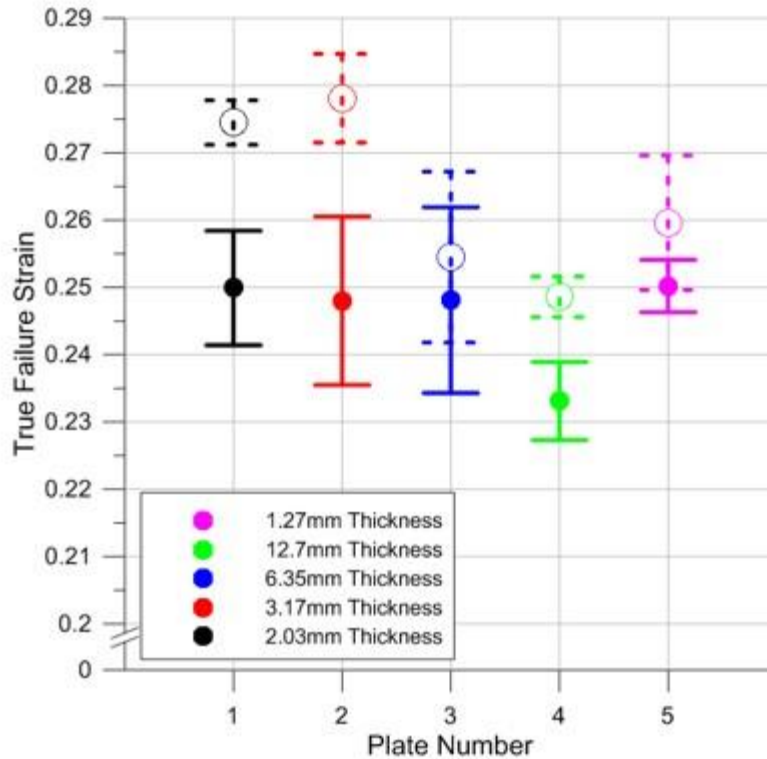


Figure 64. True failure strain from 4mm gage section extensometer for each plate at a strain rate of 0.001 s^{-1} (Solid Line) and 500 s^{-1} (Dotted Line)

In the static case, plates 1 and 2 show failure strains of 27.4% and 27.8%. P3 and P5 have lower failure strains at 25.4% and 25.9%, and P4 has the lowest average failure strain at 24.8%. In the dynamic case, P1, P2, P3, and P5 show similar failure strains around 25% while P4 has the lowest average failure strain, as in the static case, at 23.3%.

4.4.2 Compression experiments for various plate stock thickness

Compression experiments are conducted on specimens manufactured from plates P1, P2, P3, and P4. P5 is excluded due to specimen design limitations. The static and dynamic compression testing procedure is described in sections Section 3.3.2 and Section 3.5.2 respectively. In order to create a cylinder from each plate specimen dimensions and relative orientation in the material is changed. Due to the different specimen geometries, each plate is tested at a different dynamic rate. All plates were tested at a static rate of 0.001 s^{-1} . The specimen dimension, material orientation, dynamic rates are specified for each plate in Table 7 previously shown in Section 3.2.2.

The static and dynamic true stress-strain curves are presented in Figure 65 and Figure 66 respectively.

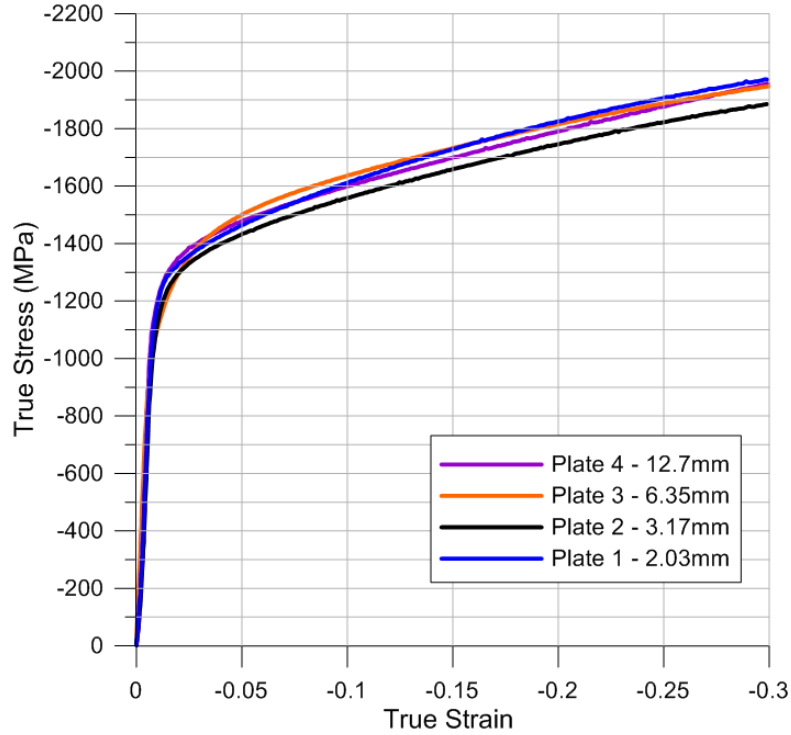


Figure 65. Representative true stress versus true strain curve for each plate in compression conducted at a strain rate of 0.001 s^{-1}

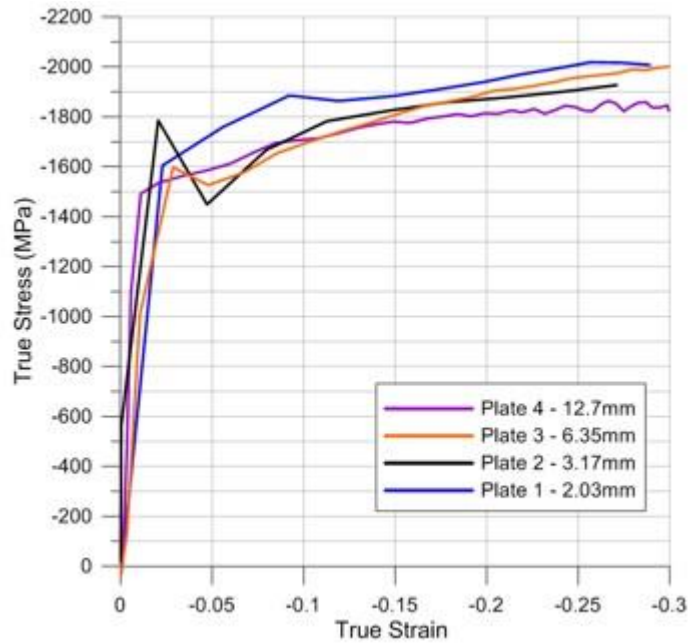


Figure 66. Representative true stress versus true strain curve for each plate in compression conducted at a strain rate of 500 s^{-1}

The true stress in each of the plates in the static rate at 5% true strain is shown in Figure 67. The results show P2 has a stress of 1434 MPa and is 4.68% and 2.9% less than the stress in P3 and P4 respectively. These results show the same trend as in the tension case, where P2 had the lowest ultimate strength. It is not possible to make a quantitative comparison between P1 and the other plates because of the material orientation.

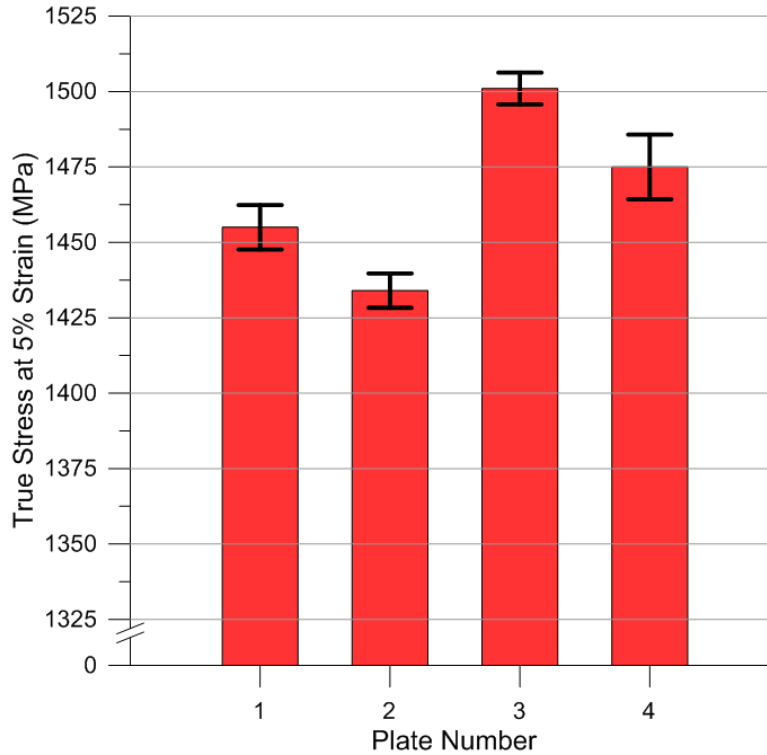


Figure 67. True stress at 5% true strain for each plate stock with error bars showing the 95th% confidence interval

4.5 Ductile fracture results

Low strain rate tests are performed to evaluate the material response up to the point of fracture with rates ranging from 0.0001 s^{-1} to 1.0 s^{-1} . The low rate tests cover a wide range of stress states induced by varying the specimen geometries. All low rate tests are performed on hydraulic load frames as described in Section 3.6. The results include tension experiments with plane stress, plane strain, and axisymmetric specimens with different notch dimensions. Results from combined loading experiments that are loaded with varying ratios of tension-torsion and compression-torsion are also presented.

4.5.1 Plane stress experiments

The four plane-stress specimen geometries with varying notch radii are shown in Table 8 in Section 3.6. They produce stress triaxialities between 0.355 and 0.574 with Lode parameters between 0.603 and 0.943. The tests are conducted at a strain rate of 0.001 s^{-1} .

The results for each specimen are plotted in Figure 68, which shows slight stress increases and large failure strain decreases as the notch radius decreases. The SG1 specimen with a smooth gage section with no notch has an ultimate stress of 1414 MPa and a failure strain of 0.28. The SG2 specimen with a 14.29 mm notch radius has a 3.6% higher ultimate stress and a 23% lower failure strain than the smooth specimen. Specimen SG3, which has a 4.76 mm notch radius, displays a small 4.9% increase in ultimate stress and a 47% lower failure strain than the smooth specimen. The SG4 specimen, which has a 0.4 mm notch radius, shows a 6.6% higher ultimate stress and a large 73% decrease in the failure strain from the smooth specimen.

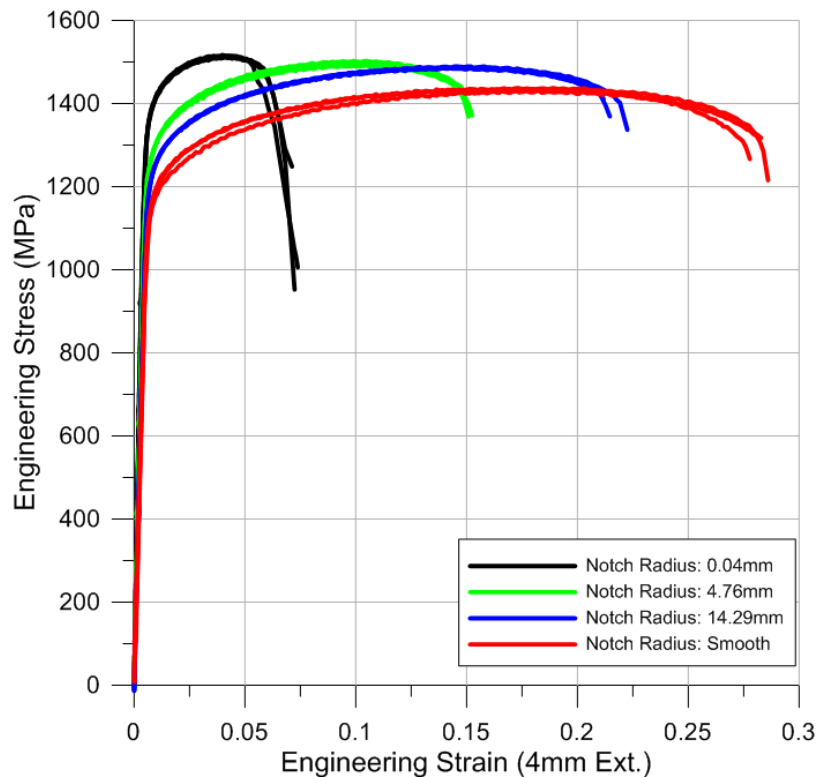


Figure 68. Engineering stress versus engineering strain for plane stress ductile fracture specimens

4.5.2 Axisymmetric experiments

Tension tests are conducted on the six notched axisymmetric specimen geometries as detailed in Table 10 presented in Section 3.6. The experiments are conducted at a nominal strain rate of 0.001 s^{-1} . All the specimens have a constant Lode parameter of 1, and stress triaxiality between 0.378 and 0.942. The results for the axisymmetric experiments are shown in Figure 69.

Figure 69 shows, as with the notched plane stress specimens, the ultimate stress increases and the failure strain decreases with decreasing notch radius. The axisymmetric test series shows a greater increase in ultimate stress than the plane stress specimens as the notch radius decreases. The ultimate stress of specimen SG10, which has the smallest 3.18 mm notch radius, is 27% higher than the smooth gage section specimen. The failure strain of the 3.18 mm notch radius specimen decreased 67% from the smooth specimen. The ultimate stress and failure strain for each notch radius specimen is tabulated in Table 15.

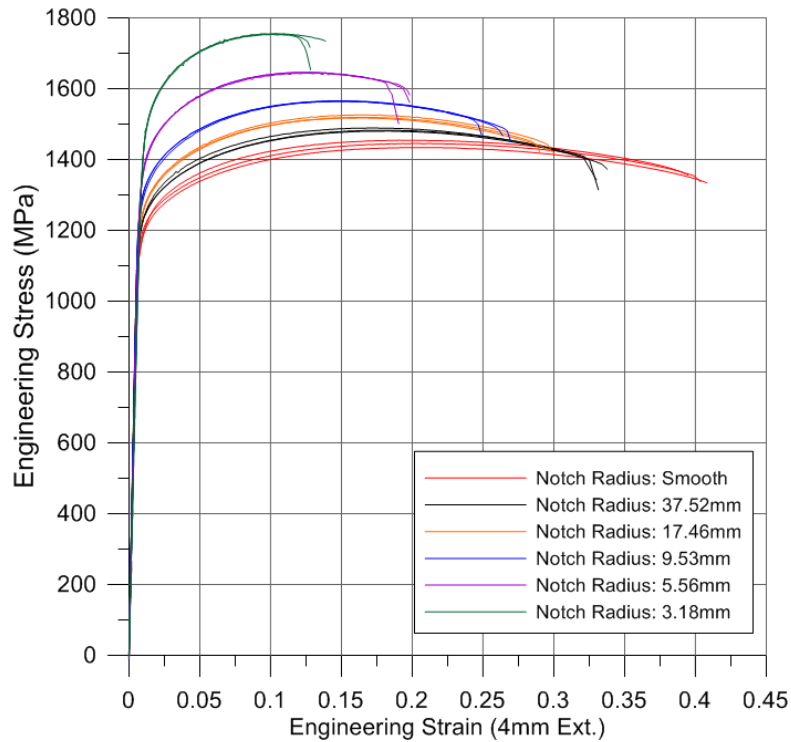


Figure 69. Engineering stress versus engineer strain measured from a 4mm extensometer for the various axisymmetric notched specimens

Table 15. Average ultimate stress and failure strain for each axisymmetric notched specimen

Specimen Number	Notch Radius (mm)	Ultimate Engineering Stress (MPa)	Engineering Failure Strain
SG5	0	1370	0.403
SG6	37.52	1415	0.333
SG7	17.46	1458	0.298
SG8	9.53	1513	0.262
SG9	5.56	1617	0.196
SG10	3.18	1743	0.133

4.5.3 Plane strain experiments

Plane strain experiments were conducted with three different specimens shown in Table 9. The test setup and procedure is described in Section 3.6. The stress-strain curves are presented in Figure 70 and show, as with the plane stress and axisymmetric specimens, the ultimate stress increases and the failure strain decreases with decreasing notch radius. The smooth plane strain specimen (SG11) has an ultimate stress of 1466 MPa and a failure strain 20%. The 12.7 mm notch radius specimen (SG12) has a 3.89% increase in ultimate stress and a 24% decrease in failure strain from the smooth specimen. The 4.76 mm notch radius specimen (SG13) has a 10% increase in ultimate stress and 41% decrease in failure strain compared to the smooth section specimen.

4.5.4 Combined loading experiments

Combined loading mode experiments are conducted in tension-torsion and compression torsion. The testing procedure is discussed in Section 3.6.2 and the specimen geometry is detailed in Table 11. The experiments are conducted with a load control method such that the axial to shear stress ratio remains constant with a nominal axial strain rate of 0.001 s^{-1} . Results showing the force-displacement and torque-rotation curves for each stress ratio are presented in Figure 71.

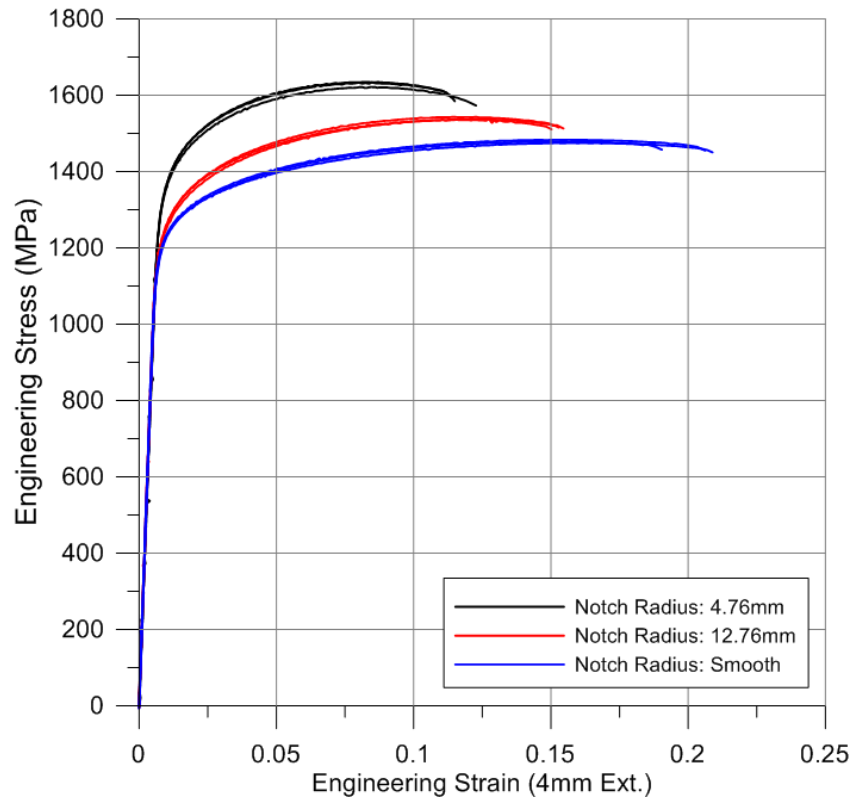


Figure 70. Engineering stress versus engineering strain for various notched radius plane specimens

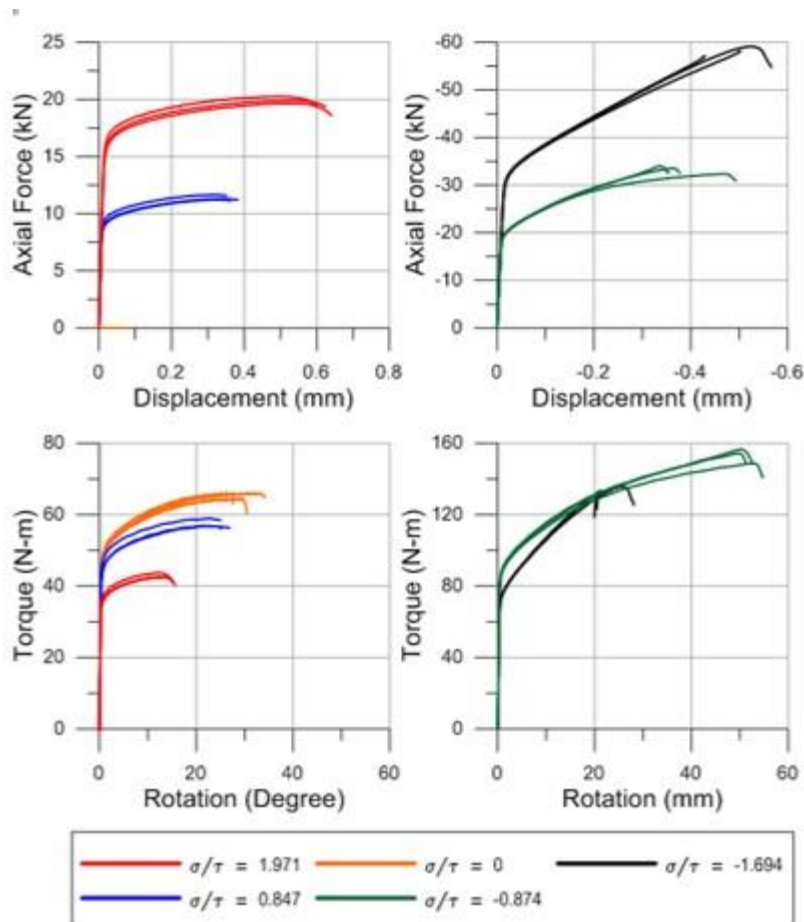


Figure 71. (Top left) Axial force versus displacement for tension-torsion experiments (Top right) Axial force versus displacement for compression-torsion experiments (Bottom left) Torque versus rotation for tension-torsion experiments (Bottom right) Torque versus rotation for compression-torsion experiments

4.5.5 Ductile fracture discussion

A comparison is made between all the ductile fracture tests by using the equivalent plastic strain. The equivalent plastic failure strain is calculated from the principal strains measured at the failure point with DIC in the Equation 47, where ε_1 and ε_2 are the first and second principal strains measured directly from the DIC.

$$\bar{\varepsilon}_p = \sqrt{\frac{2}{3} (\varepsilon_1^2 + \varepsilon_2^2 + \varepsilon_3^2)} \quad 47$$

The third principal strain, ε_3 , is found using the assumption that the material is incompressible after the yield point and is calculated directly from first and second principal plastic strain as shown in Equation 48.

$$\varepsilon_3 = -(\varepsilon_1 + \varepsilon_2)$$

The average equivalent plastic strain at failure for each of the ductile fracture specimens is presented as a function of stress triaxiality and Lode parameter in Figure 72 and Figure 73. For both figures, error bars are shown for 95% confidence margin for each case.

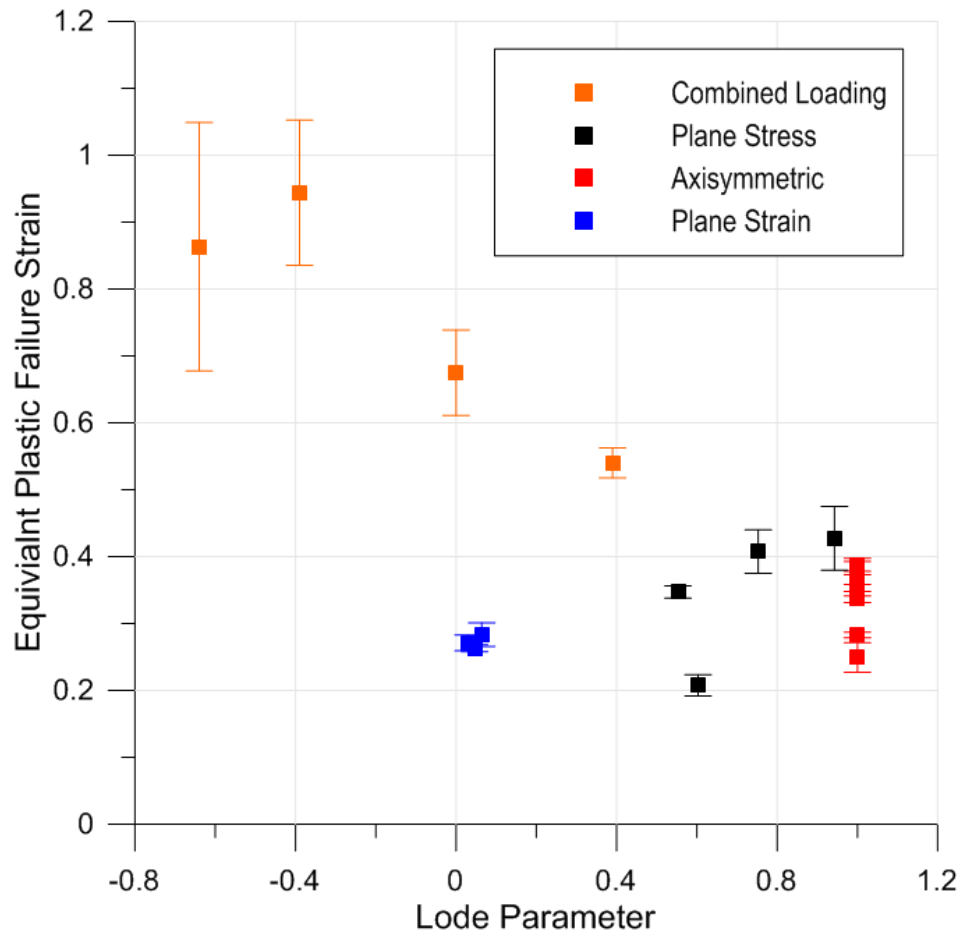


Figure 72. Equivalent plastic failure strain versus Lode. Lode parameter for each ductile fracture case.

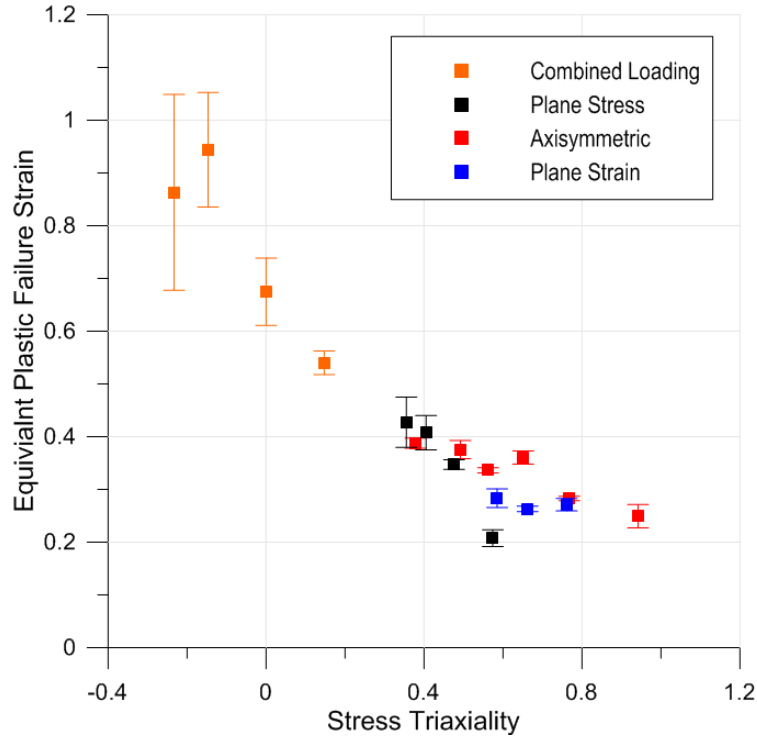


Figure 73. Equivalent plastic failure strain versus stress triaxiality for each ductile fracture case.

Figure 73 shows a general relationship of increasing equivalent failure strain and decreasing (more compressive) stress triaxiality. This trend is consistent between all four test series. The results show that plane stress, plane strain, and axisymmetric specimens tested at similar stress triaxialities between 0.562 and 0.585, have varying equivalent failure strain between 0.207 and 0.271. This suggests that stress triaxiality is not solely enough to predict ductile fracture. Figure 72 shows no obvious relationship between Lode parameter and equivalent failure strain.

4.6 Punch experiments

Punch tests are conducted on thin Inconel specimens machined from plate P4 at quasi-static and dynamic strain rates. These experiments provide useful data for construction and validation of the ductile fracture locus in the tabulated Johnson-cook material model. Three different punch geometries are used including a blunt, sharp radius (6.35 mm) and hemispherical-shaped punch. The entire test procedure and exact punch and specimen geometries are discussed in Section 3.6.3.

The quasi-static and dynamic punch test results are presented for the blunt, sharp, and hemispherical geometries in Figure 74, Figure 75, and Figure 76 respectively. The punch velocity in the quasi-static test is 0.0189 mm/s. In the dynamic experiments, the punch velocity is 9 m/s in the blunt case and 9.6 m/s in the sharp radius case. Not enough displacement can be achieved with the testing apparatus to fail the specimen with the hemispherical punch.

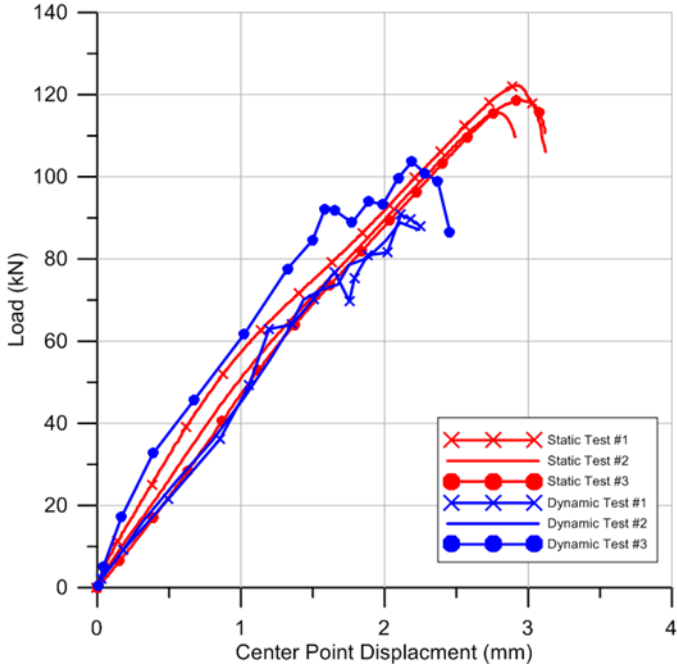


Figure 74. Blunt punch force versus specimen center point displacement for the dynamic (blue) and static (red) experiments

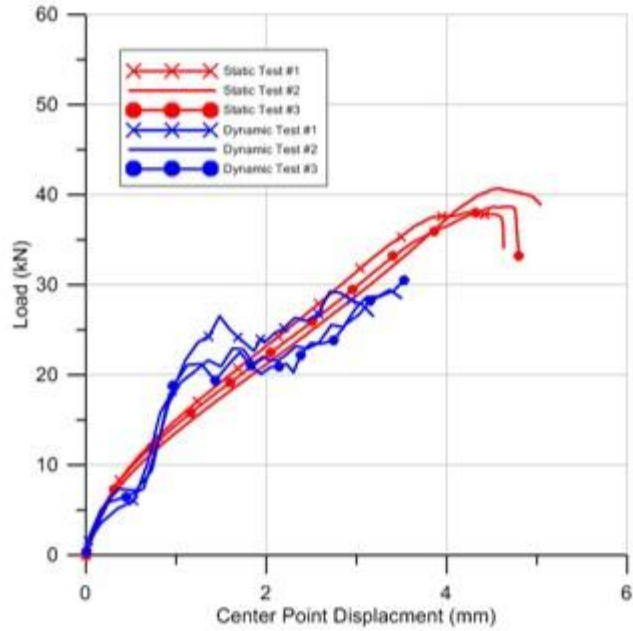


Figure 75. Sharp (6.35mm radius) punch force versus specimen center point displacement for the dynamic (blue) and static (red) experiments

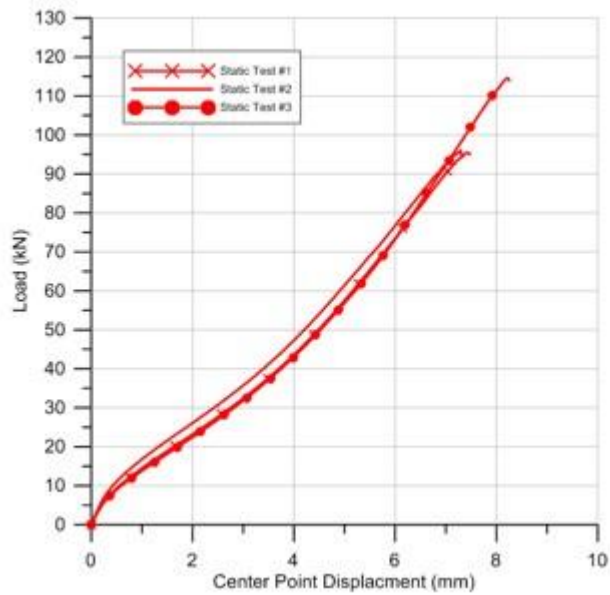


Figure 76. Hemispherical punch force versus specimen center point displacement for the static (red) experiments

The quasi-static blunt punch test has a failure force of 118.9 kN and a max center point displacement of 2.88 mm. The blunt punch dynamic case has a similar force displacement relationship but fails at a load 94.4 kN, a 20.5% decrease. The center point displacement at failure also decreases to 2.13 mm. The quasi-static sharp radius punch experiments show a failure force of 39.167 kN and a center point displacement of 4.51 mm. The dynamic sharp radius punch experiments show an average max force of 29.72 kN and 3.2 mm displacement at failure. As in the blunt punch experiments, the force displacement relationship in the dynamic case is similar to that of the quasi-static case but fails at a reduced load and displacement. The quasi-static hemispherical punch geometry has the highest failure displacement at 7.65 mm and a failure force of 102 kN. The results also show the equivalent failure strain at the failure point in the quasi-static experiments decreases with increased punch radius. At failure, the equivalent failure strain in the blunt, sharp, and hemispherical punch geometries is 0.534, 0.497, and 0.393 respectively. The first principal strain histories are for all three quasi-static punches in Figure 77.

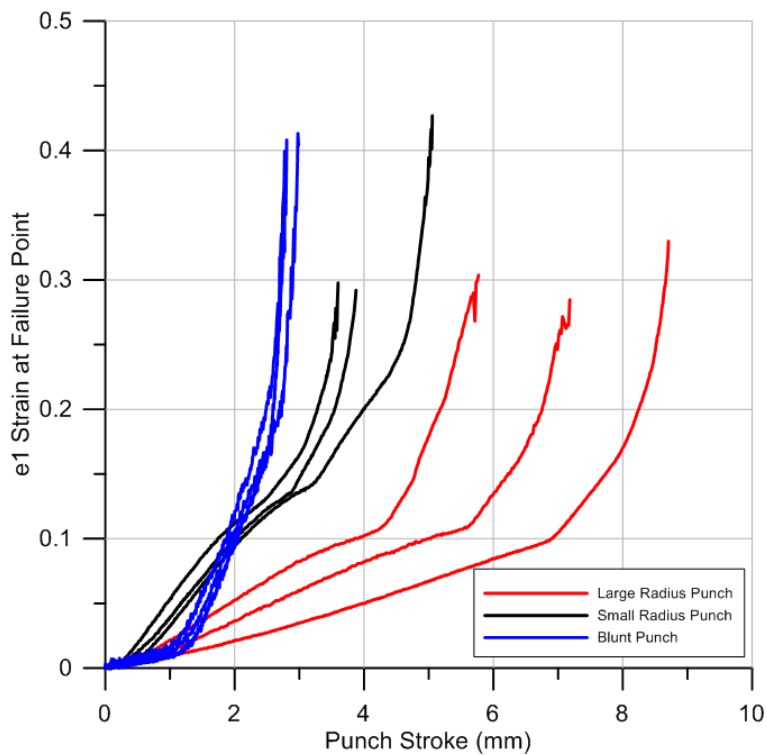


Figure 77. First principal strain at the failure point versus the punch stroke displacement for the quasi-static -blunt, sharp radius, and hemispherical punch

5 Summary and conclusions

The plastic deformation and fracture of precipitation hardened Inconel 718 is studied in tension, compression, and torsion and tension at different strain rates and temperatures. Ductile fracture is studied using a variety of specimen designs cut from a 12.7 mm thick plate (P4) to obtain failure data over a wide range of stress states. The ductile fracture test series include plane stress, plane strain, and axisymmetric samples with various notch geometries subjected to tension. Combined loading fracture tests with constant tension-torsion and compression-torsion stress ratios are conducted on hollow samples. A series of punch tests at quasi-static and dynamic rates are performed using three different punch geometries. Anisotropy is measured by performing experiments in tension and compression on specimens cut from different orientations with respect to the plate rolling direction. The effect of plate thickness is examined by comparing results for five different thickness plate stocks in tension and compression. Low strain rate tests below 1.0 s^{-1} are performed using a servohydraulic load frame. High strain rate tests are performed using tension, compression, and torsion SHB test setups. DIC is used to accurate full field strain measurements.

Strain rate sensitivity is apparent in tension and compression for Inconel 718. However, in torsion the material exhibits no significant rate sensitivity up to a strain rate of 2000 s^{-1} in torsion. Large rate sensitivity increases in compression are seen at strain rates above 1000 s^{-1} .

Temperature dependence experiments show large decreases in strength with increasing temperature. Complex changes in ductility are also observed. The strength dramatically decreases in all three loading modes at $800 \text{ }^{\circ}\text{C}$.

Strong sensitivity to stress triaxiality and mild sensitivity to the Lode parameter is observed in the ductile fracture experiments. Decreasing notch radius in the plane stress, plane strain, and axisymmetric experiments show increasing effective stress and decreasing equivalent strain at failure. A wide range of equivalent failure strains is observed, ranging from 0.20 in the plane strain experiments to 0.94 in the combined loading experiments.

Quasi-static and dynamic punch tests are conducted for use in the material model validation. The results show increasing punch displacement to failure with increasing sharpness of punch. The dynamic force displacement curve exhibits a similar force-displacement relationship but fails at 20-25% lower force in both the dynamic blunt and sharp radius punch experiments.

Anisotropy tests show lower stress in the $\pm 45^{\circ}$ directions and greater stress in the transverse direction when compared to the rolling direction. These results are statistically significant.

Compression and tension experiments show strength differences between the plate stocks but are not directly related to plate thickness. The static experiments in compression and tension both show P1 (2.07 mm thick) to be on average 5% weaker than the other plates while P4 (12.7 mm thick) is shown to be slightly stronger. P4 also exhibits the lowest failure strain in both the static and dynamic tension tests. The dynamic compression experiments are conducted at different rates and a direct comparison is not conducted.

The experimental data from specimen tests conducted at the OSU DMML contained in this report will serve as input data for creation of a precipitation hardened Inconel 718 material input deck for use with the tabulated Johnson Cook material model MAT_224 in LS-DYNA for dynamic impact applications. Additional tests performed on Inconel 718 material at OSU DMML include new small diameter punch tests (Spulak, 2022), as well as high rate tension tests with thermal imaging (Smith, 2020) to examine plastic heating and are published as separate FAA reports. Material data certification sheets are also published as part of a separate report detailing ballistic impact tests conducted using the same Inconel 718 plate stocks by NASA Glenn Research Center (Pereira, Revilock, & Ruggeri, 2020).

6 References

- Ansys. (2021). LS-DYNA keyword user's manual, Volume II material models. Livermore, CA: Ansys.
- Bao, Y., & Wierzbicki, T. (2004). On fracture locus in the equivalent strain and stress triaxiality space. *International Journal of Mechanical Sciences*, 46(1), 81-98.
- Barsoum, I., & Faleskog, J. (2007). Rupture mechanisms in combined tension and shear—Experiments. *International Journal of Solids and Structures*, 44(6), 1768-1786.
- Booker, M. K., & Booker, B. L. (1980). *Elevated-temperature tensile properties of three heats of commercially heat-treated Alloy 718 (No. ORNL-TM-7174)*. . Oak Ridge, TN, USA: Oak Ridge National Lab.
- Bridgman, P. W. (1964). *Studies in large plastic flow and fracture: with special emphasis on the effects of hydrostatic pressure*. Harvard University Press.
- Buyuk, M. (2014). *Development of a new metal material model in LS-DYNA, part 2: Development of a tabulated thermo-viscoplastic material model with regularized failure for dynamic ductile failure prediction of structures under impact loading*. Final Report, Federal Aviation Administration, U.S. Department of Transportation. Retrieved from <https://www.tc.faa.gov/its/worldpac/techrpt/tc13-25p2.pdf>
- Carney, K., Bois, P. D., Sengoz, K., Wang, L., & Kan, C.-D. (2020). *Development of a generalized yield surface for isotropic, pressure-insensitive metal plasticity with differing tension, compression, and shear yield strengths*. Final Report, Federal Aviation Administration, U.S. Department of Transportation. Retrieved from <https://www.tc.faa.gov/its/worldpac/techrpt/tc19-42.pdf>
- Chen, W., & Chaturvedi, M. (1997). On the mechanism of serrated deformation in aged Inconel 718 . *Materials Science and Engineerin(A229)*, 163-168.
- Correlated Solutions Inc. (2014, March). *Non-contacting measurement*. Retrieved from <http://www.correlatedsolutions.com>
- Dabboussi, W., & Nemes, J. (2005). Modeling of ductile fracture using the dynamic punch test. *International Journal of Mechanical Sciences*, 47(8), 1282-1299.
- DaMange, J., Prakash, V., & Pereira, J. (2009). Effects of material microstructure on blunt projectile penetration of a nickel-based super alloy. 36(8), 1027-1043.

- Dowling, A., Harding, J., & Campbell, J. (1970). The dynamic punching of metals. *Journal of the Institute of Metals*(98), 217-224.
- Ezugwu, E. (2005). Key improvements in the machining of difficult-to-cut aerospace superalloys. *International Journal of Machine Tools and Manufacture*, 45(12-13), 1353-1367.
- Garat, V., Cloue, J.-M., Poquillon, D., & Andrieu, E. (2008). Influence of Portevin–Le Chatelier effect on rupture mode of alloy 718 specimens. *Journal of Nuclear Materials*, 375(1), 95-101.
- Gilat, A. (2000). Torsional kolsky bar testing. In *ASM Handbook 8* (pp. 505-515).
- Goijaerts, A., Govaert, L., & Baaijens, F. (2001). Evaluation of ductile fracture models for different metals in blanking. *Journal of Materials Processing Technology*(110), 312-323.
- Gudruru, R., Darling, K., Kishore, R., Scattergood, R., Kock, C., & Murty, K. (2005). Evaluation of mechanical properties using shear–punch testing. *Materials Science and Engineering*(395), 307-314.
- Hammer, J. T. (2014). *Plastic deformation and ductile fracture of Ti-6Al-4V under various loading conditions*. DOT/FAA/TC-TT14/2. Retrieved from <https://www.tc.faa.gov/its/worldpac/techrpt/tctt14-2.pdf>
- Jafarian, F., Ciaran, M., Umbrello, P., Arrazola, P., Filice, L., & Amirabadi, H. (2014). Finite element simulation of machining Inconel 718 alloy including microstructure changes. *International Journal of Mechanical Sciences*(88), 110-121.
- Johnson, G. R., & Cook, W. (1983). A constitutive model and data for metals subjected to large strains, high strain rates and high temperatures. (pp. 541-547). The Hague, Netherlands: Proceedings of the 7th International Symposium on Ballistics.
- Johnson, G. R., & Cook, W. H. (1985). Fracture characteristics of three metals subjected to various strains, strain rates, temperatures and pressures. *Engineering fracture mechanics*, 21(1), 31-48.
- Kobayashi, T., Simons, J., Brown, C., & Shockey, D. (2008). Plastic flow behavior of Inconel 718 under dynamic shear loads. *International Journal of Impact Engineering*, 35(5), 389-396.
- Liutkus, T. (2014). *Digital image correlation in dynamic punch testing and plastic deformation behavior of Inconel 718*, Master Thesis. Columbus, OH: The Ohio State University.

- McLouth, T. D., Witkin, D. B., Lohser, J. R., Sitzman, S. D., Adams, P. M., Lingley, Z. R., . . . Zaldivar, R. J. (2021). Temperature and strain-rate dependence of the elevated temperature ductility of Inconel 718 prepared by selective laser melting. *Materials Science and Engineering: A*, 824, 141814.
- Paulonis, D. F., & Schirra, J. J. (2001). Alloy 718 at Pratt & Whitney—Historical perspective and future challenges. *Superalloys*, 718(625,706), 13-23.
- Pereira, J. M., & Lerch, B. A. (2001). Effects of heat treatment on the ballistic impact properties of Inconel 718 for jet engine fan containment applications. *International Journal of Impact Engineering*, 25(8), 715-733.
- Pereira, J. M., Revilock, D. M., & Ruggeri, C. R. (2020). *Impact Testing of Inconel 718 for material impact model development*, NASA/TM-2020-220451, DOT/FAA/TC-19/40. Cleveland, Ohio: National Aeronautics and Space Administration Glenn Research Center (NASA-GRC), Federal Aviation Administration (FAA). Retrieved from <https://www.tc.faa.gov/its/worldpac/techrpt/tc19-40.pdf>
- Prasad, K., Sarkar, R., Kumar, V., & Ghosal, P. (2010). Tensile deformation behaviour of forged disc of IN 718 superalloy at 650 °C. *Materials & Design*, 31(9), 4502-4507.
- Ressa, A. M. (2015). *Plastic deformation and ductile fracture behavior of Inconel 718*, Master Thesis. Columbus, OH: The Ohio State University.
- Schafrik, R. E., Ward, D. D., & Groh, J. R. (2001). Application of alloy 718 in GE aircraft engines: past, present and next five years. *Superalloys*, 718(625), 1-11.
- Sciuva, M. D., Frola, C., & Salvano, S. (2003). Low and high velocity impact on Inconel 718 casting plates:. *International Journal of Impact Engineering*(28), 849-876.
- Seidt, J. D. (2014). *Development of a new metal material model in LS-DYNA, part 3: Plastic deformation and ductile fracture of 2024 aluminum under various loading conditions*. Final Report, Federal Aviation Administration, U.S. Department of Transportation. Retrieved from <https://www.tc.faa.gov/its/worldpac/techrpt/tc13-25-p3.pdf>
- Smith, J. (2020). *Full-field measurement of the Taylor-Quinney coefficient in tension tests of Ti-6Al-4V, aluminum 2024-T351, and Inconel 718 at various strain rates [DOT/FAA/TT-20/40]*. Federal Aviation Administration. Retrieved from <http://www.tc.faa.gov/its/worldpac/techrpt/tc20-40.pdf>

- Spulak, N. (2022). *Investigations into ductile fracture and deformation of metals under combined quasi-static loading and under extremely high-rate compressive impact loading [DOT/FAA/TCTT22-33]*. Federal Aviation Administration.
doi:<https://doi.org/10.21949/1524507>
- Staab, G. H., & Gilat, A. (1991). A direction-tension split Hopkinson bar for high strain-rate testing. *Experimental Mechanics*, *31*, 232-235.
- Sutton, M. A. (2009). *Image correlation for shape, motion and deformation measurements: basic concepts, theory and applications*. New York: Springer Science & Business Media.
- Thomas, A., El-Wahabi, M., Cabrera, J., & Prado, J. (2006). High temperature deformation of Inconel 718. *Journal of Materials Processing Technology*(177), 469-472.
- Xue, H., Lijun, W., Runguang, L., Shaogang, W., & Zhonglin, C. (2003). Superplastic properties of Inconel 718. *Journal of Materials Processing Technology*, *137*(1-3), 17-20.
- Xue, L. (2007). Damage accumulation and fracture initiation in uncracked ductile solids subject to triaxial loading. *International Journal of Solids and Structures*, *44*(16), 5163-5181.
- Zhang, B., Mynors, D., Mugarra, A., & Ostolaza, K. (2004). Representing the superplasticity of Inconel 718. *Journal of Materials Processing Technology*, *153*, 694-698.
- Zhang, S. H., Zhang, H. Y., & Cheng, M. (2011). Tensile deformation and fracture characteristics of delta-processed Inconel 718 alloy at elevated temperature. *Materials Science and Engineering: A*, *528*(19-20), 6253-6258.
- Zhou, L. X. (1994). Effects of strain rate and temperature on deformation behaviour of IN 718 during high temperature deformation. *Materials Science and Engineering*, *177*(1-2), 1-9.

A Strain rate sensitivity test results

The following figures display temperature-sensitivity test results for tension, compression, and torsion.

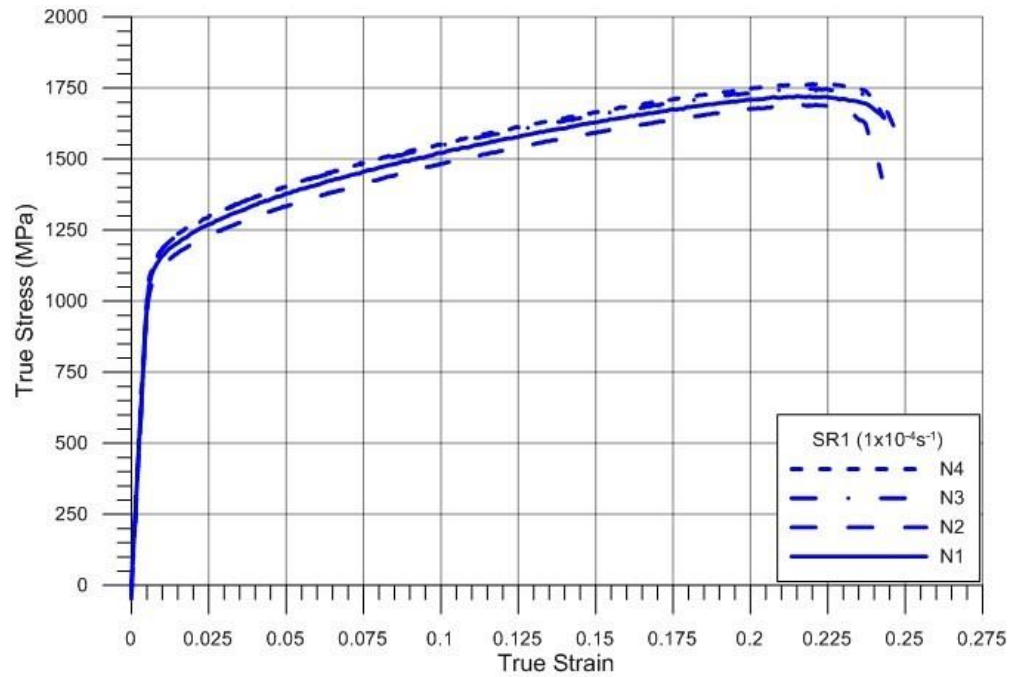


Figure A- 1. True stress vs true strain for tension experiments conducted at 0.0001 s^{-1}

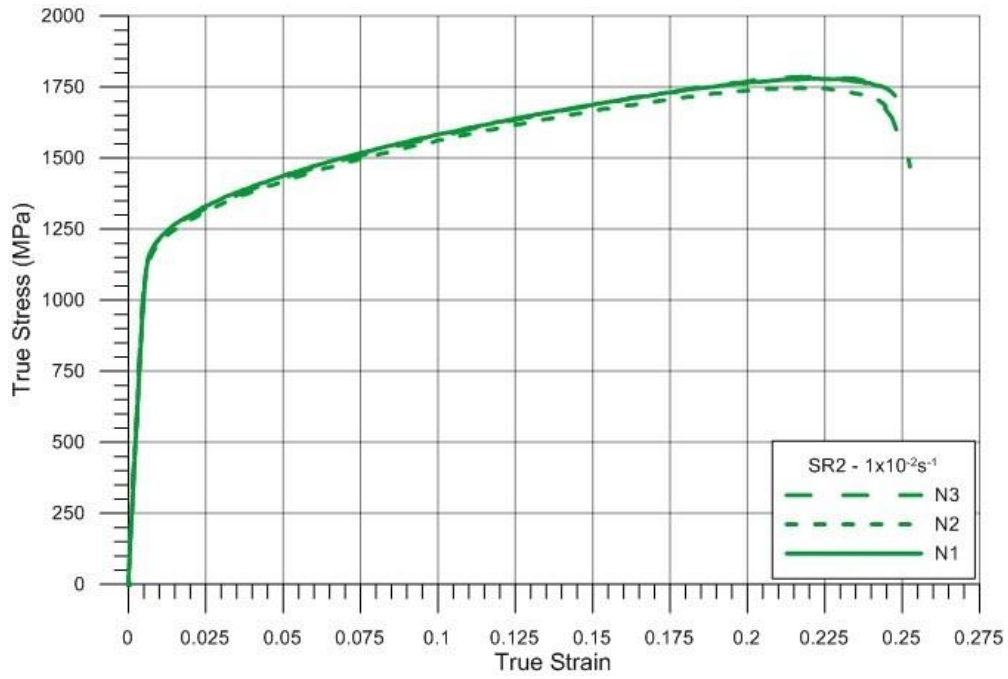


Figure A- 2. True stress vs true strain for tension experiments conducted at 0.01 s^{-1}

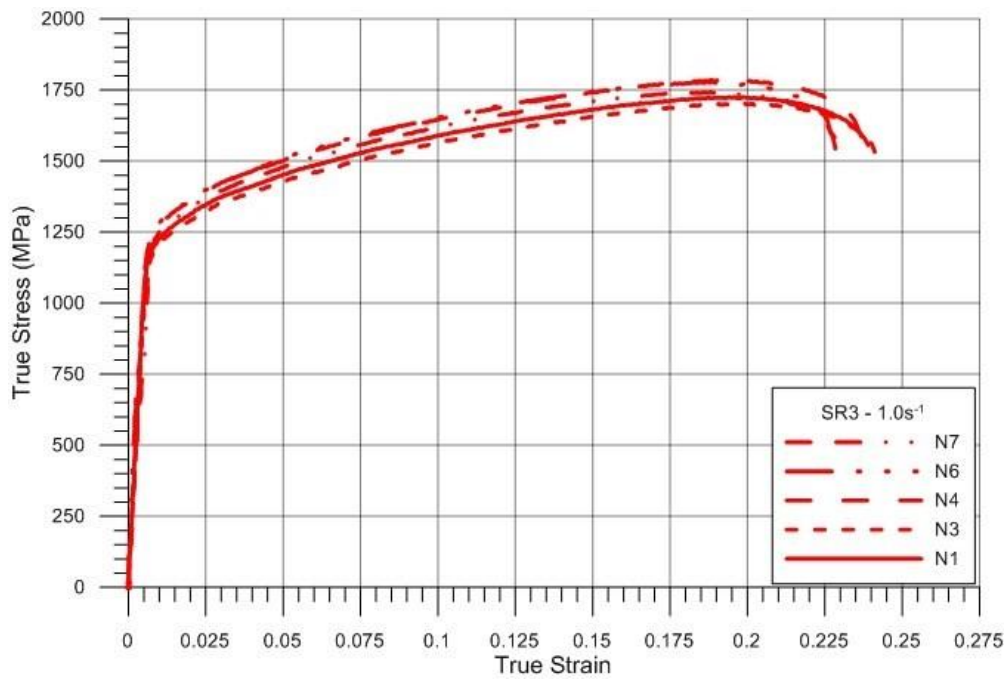


Figure A- 3. True stress vs true strain for tension experiments conducted at 1.0 s^{-1}

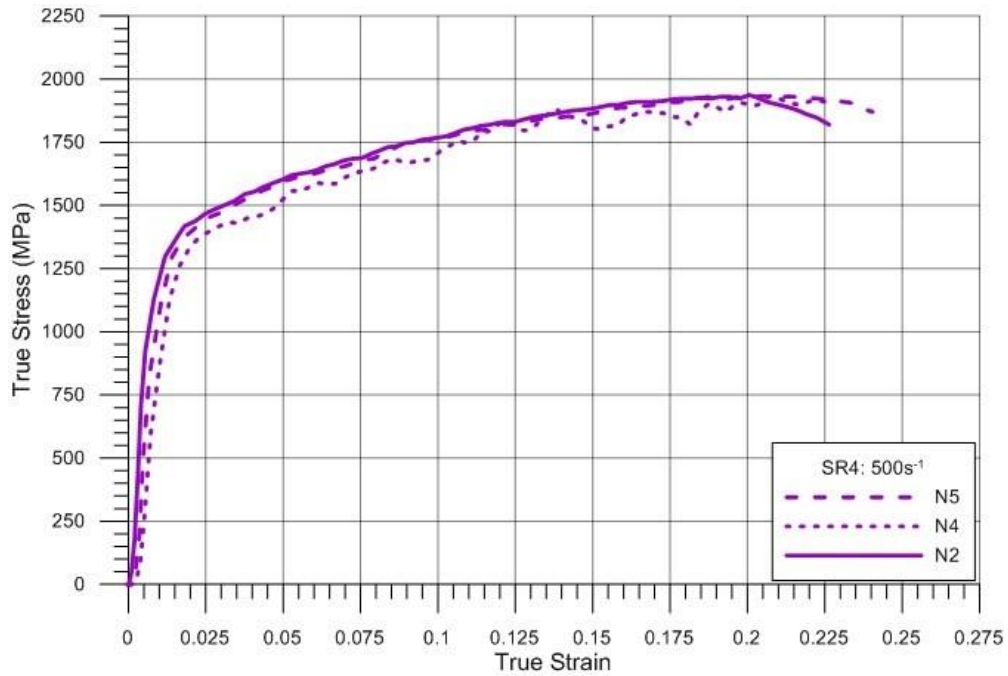


Figure A- 4. True stress vs true strain for tension experiments conducted at 500 s⁻¹

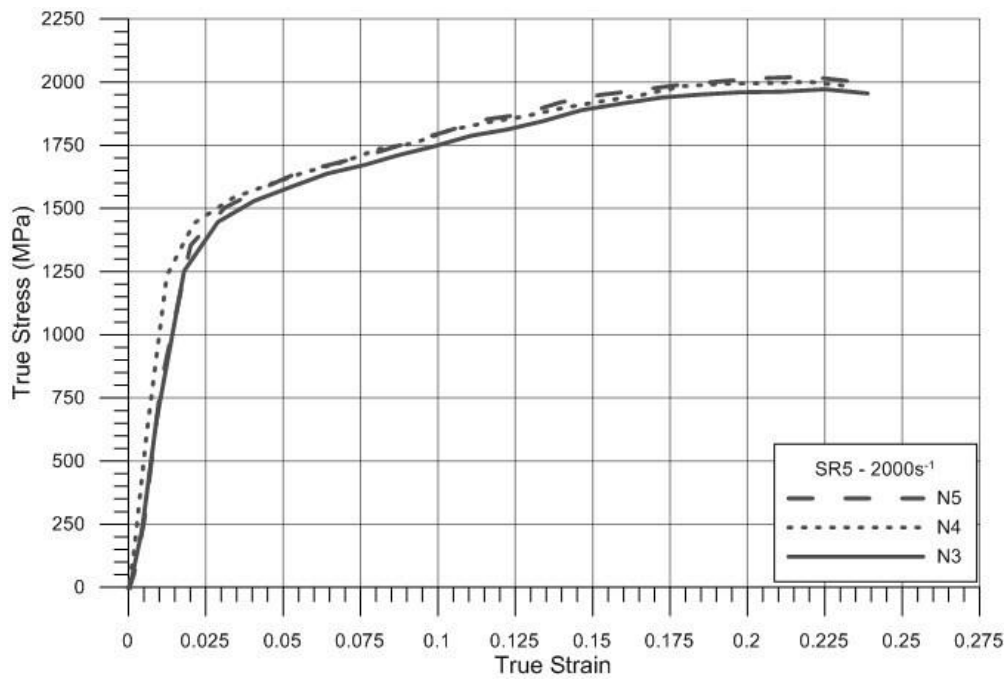


Figure A- 5. True stress vs true strain for tension experiments conducted at 2000 s⁻¹

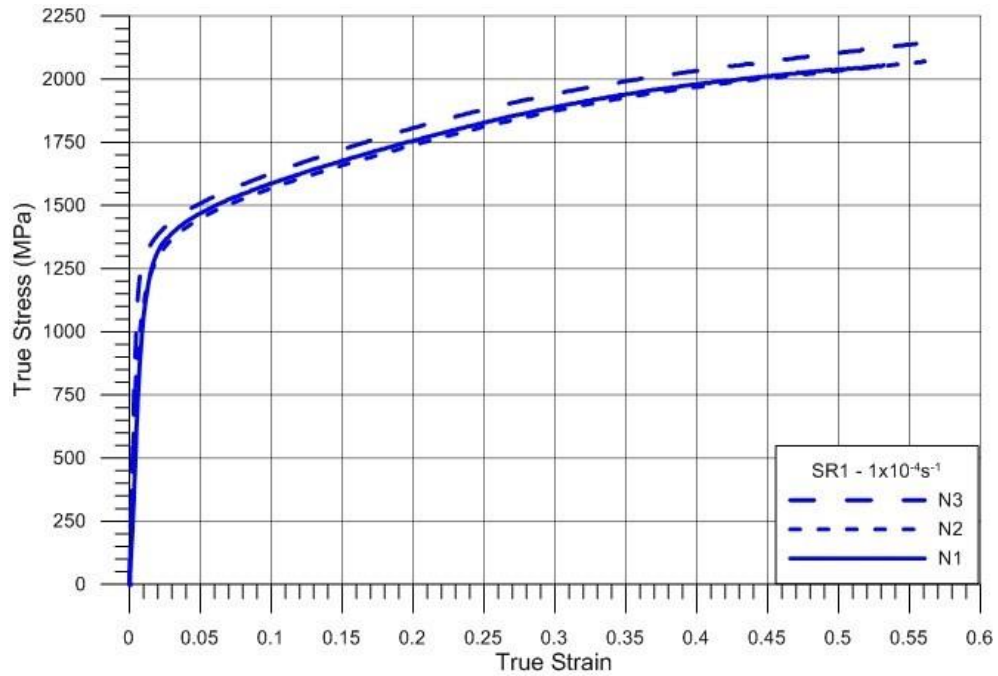


Figure A- 6. True stress vs true strain for compression experiments conducted at 0.0001 s^{-1}

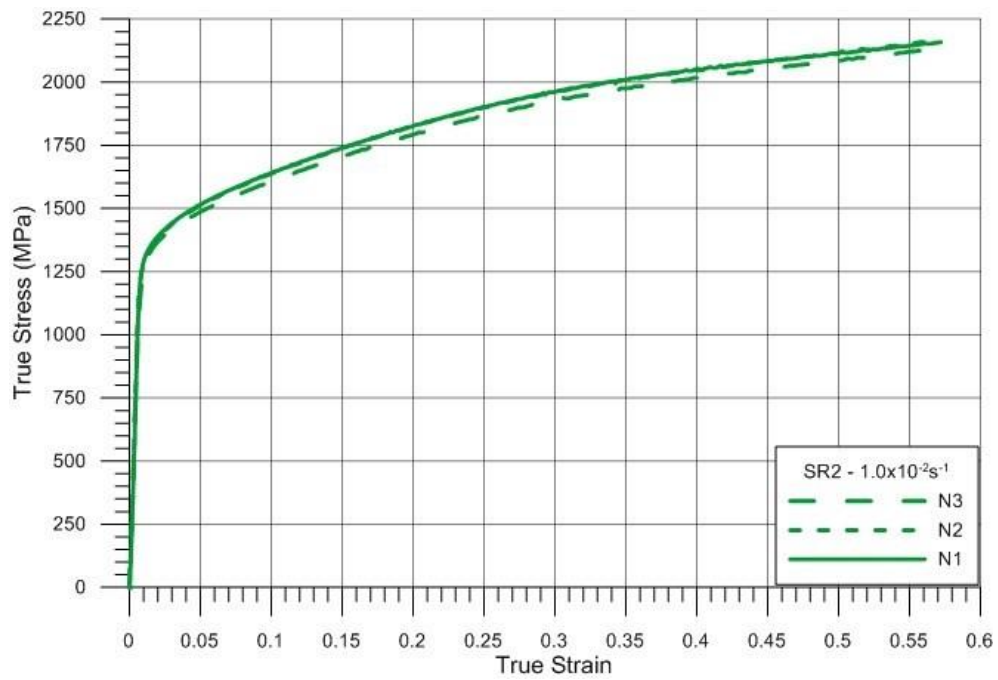


Figure A- 7. True stress vs true strain for compression experiments conducted at 0.01 s^{-1}

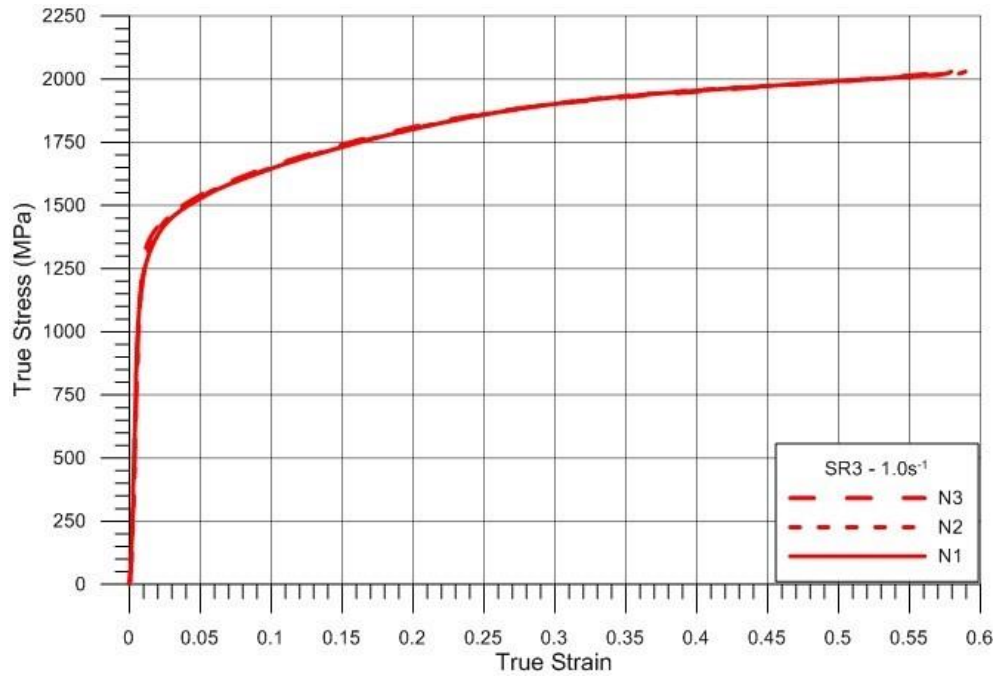


Figure A- 8. True stress vs true strain for compression experiments conducted at 1.0 s^{-1}

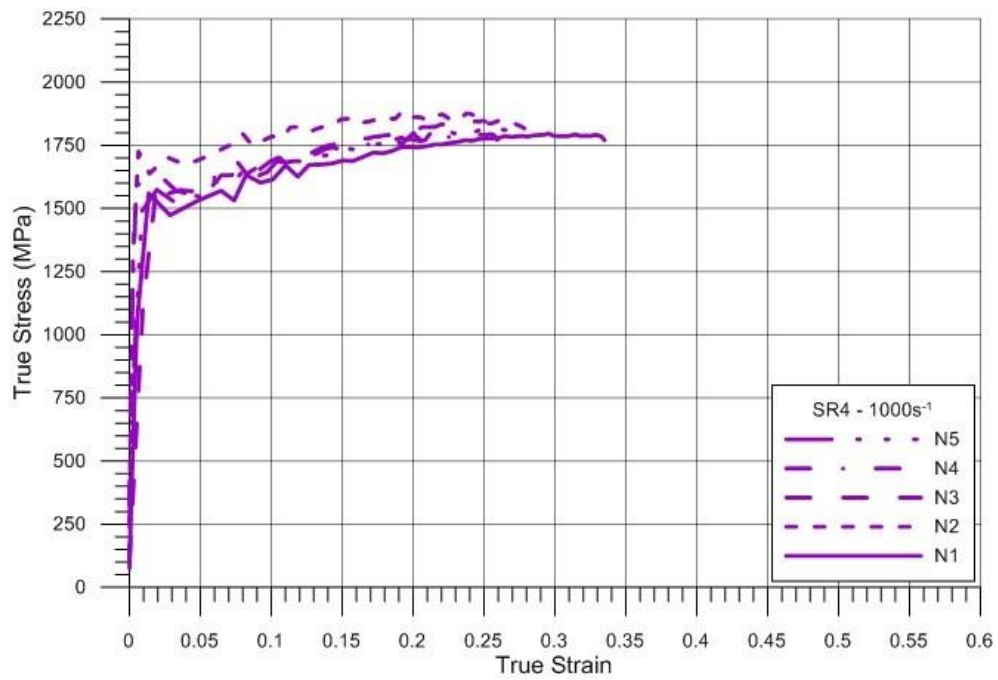


Figure A- 9. True stress vs true strain for compression experiments conducted at 1000 s^{-1}

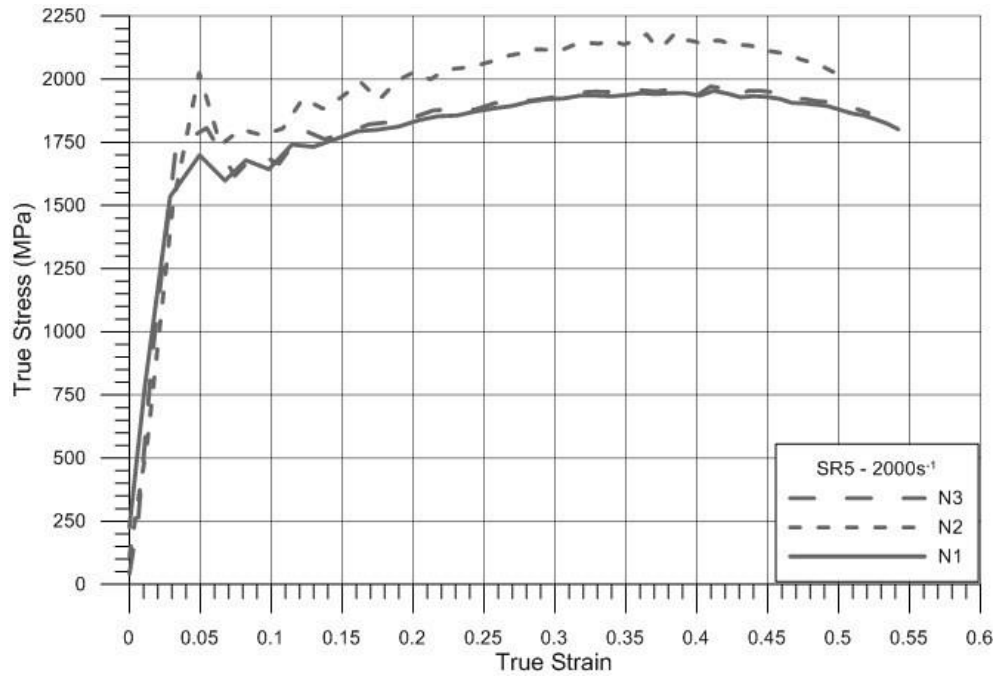


Figure A- 10. True stress vs true strain for compression experiments conducted at 2000 s⁻¹

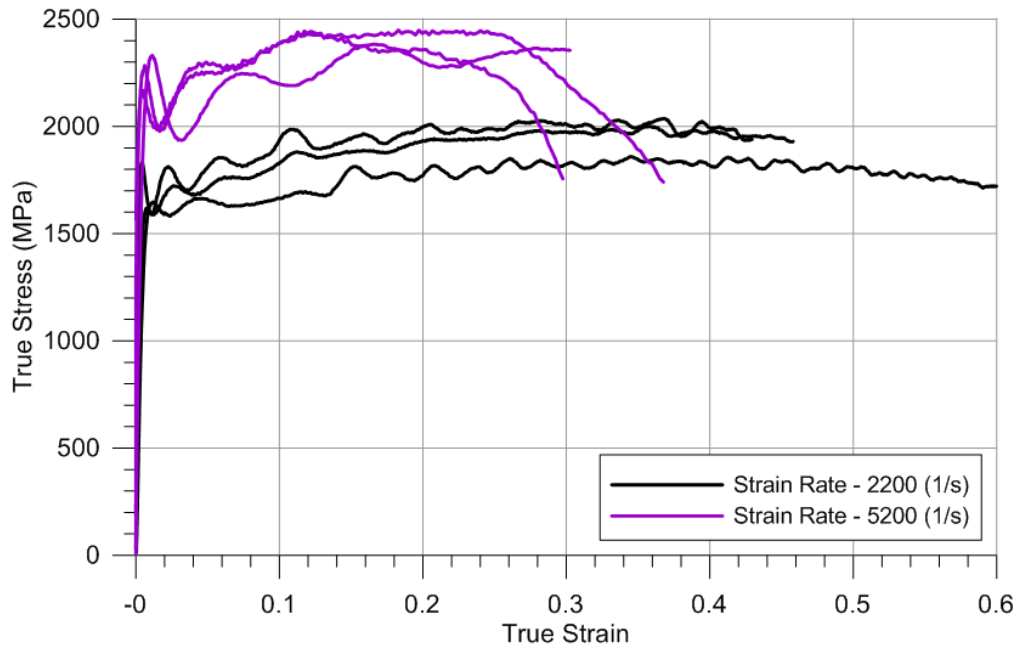


Figure A- 11. True stress vs true strain for compression experiments conducted at 2200 and 5200 s⁻¹

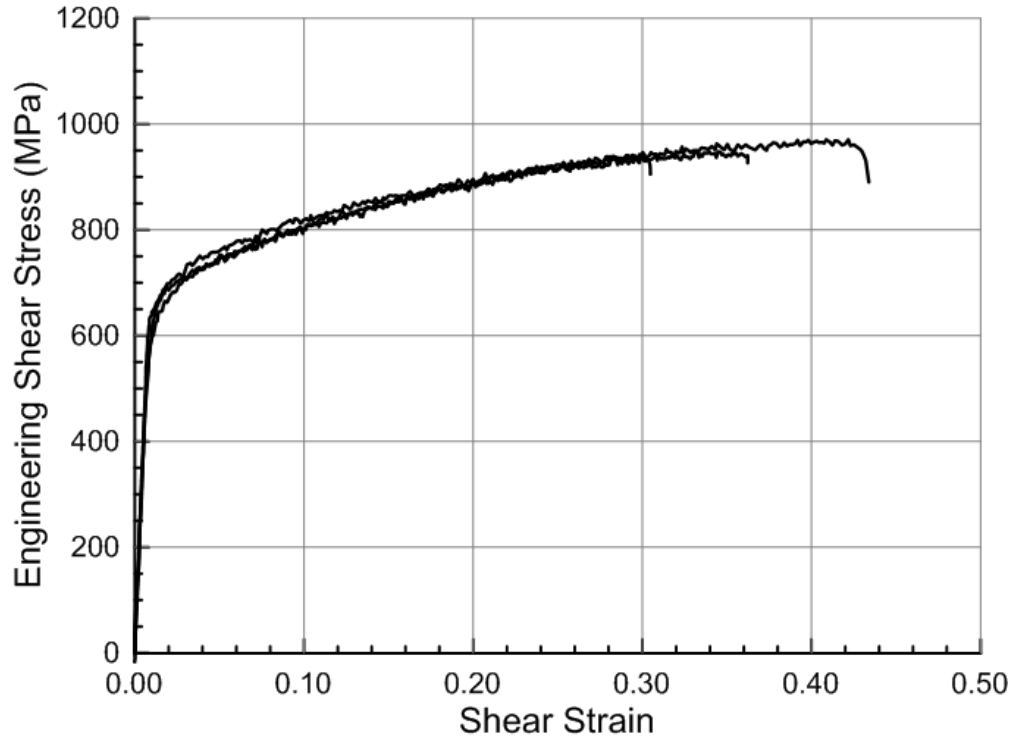


Figure A- 12. Engineering shear stress versus DIC shear strain for all torsion tests at a strain rate of 0.0001 s^{-1}

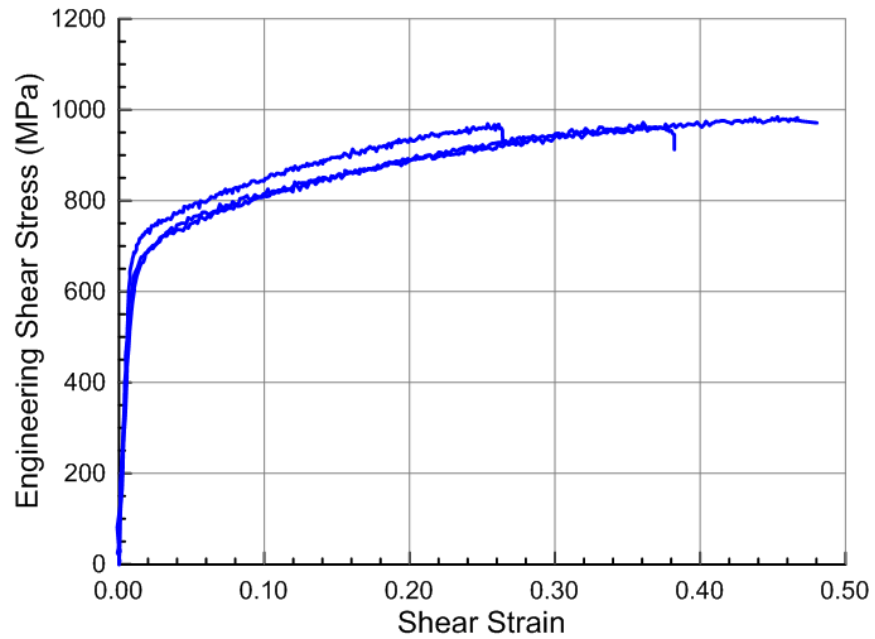


Figure A- 13. Engineering shear stress versus DIC shear strain for all torsion tests at a strain rate of 0.01 s^{-1}

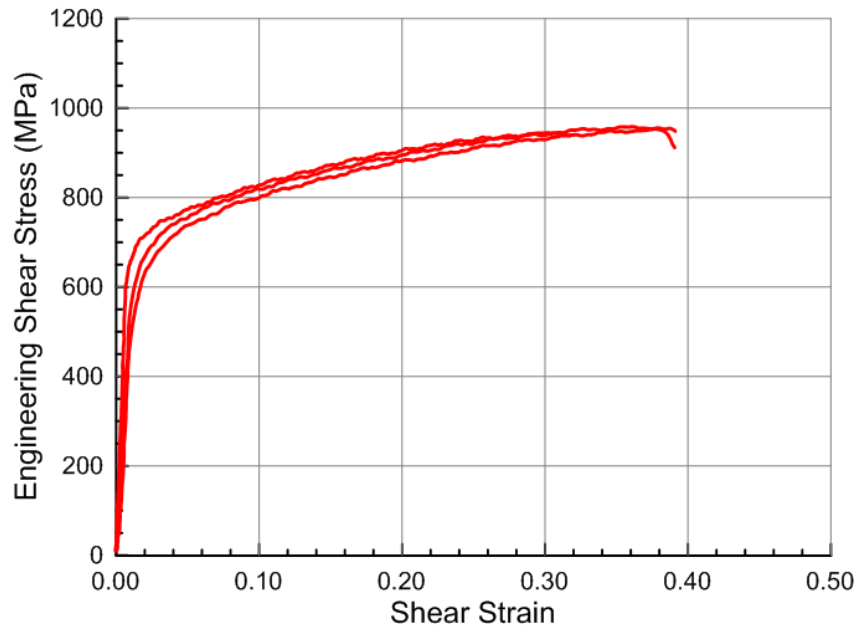


Figure A- 14. Engineering shear stress versus DIC shear strain for all torsion tests at a strain rate of 0.01 s⁻¹

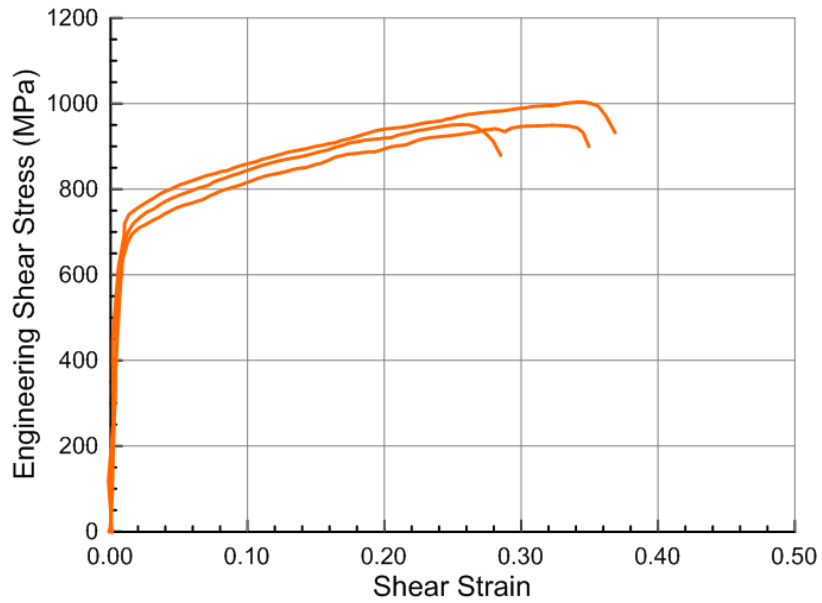


Figure A- 15. Engineering shear stress versus DIC shear strain for all torsion tests at a strain rate of 500 s⁻¹

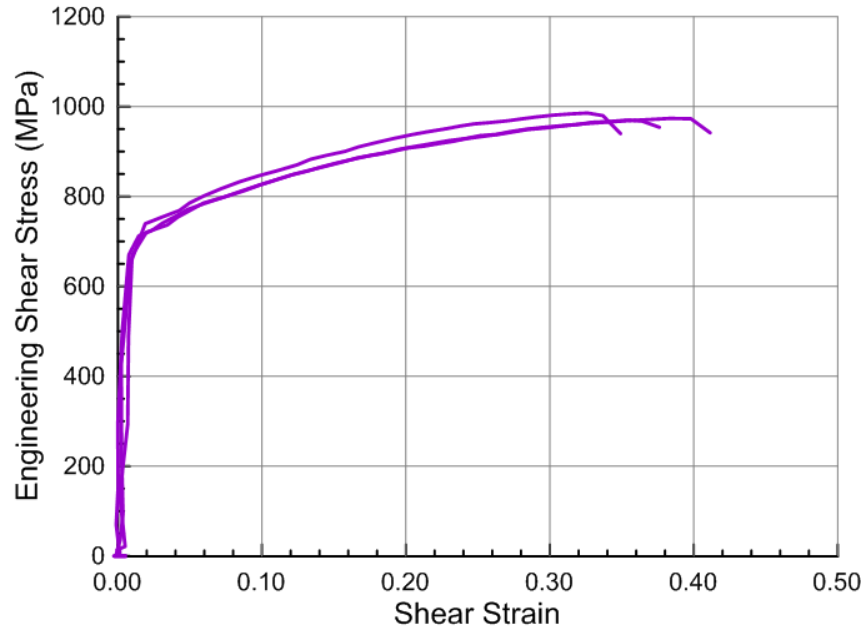


Figure A- 16. Engineering shear stress versus DIC shear strain for all torsion tests at a strain rate of 2000 s⁻¹

B Temperature sensitivity test results

Temperature-sensitivity test results are shown for compression tests at all temperatures conducted at a strain rate of 0.001 s^{-1} .

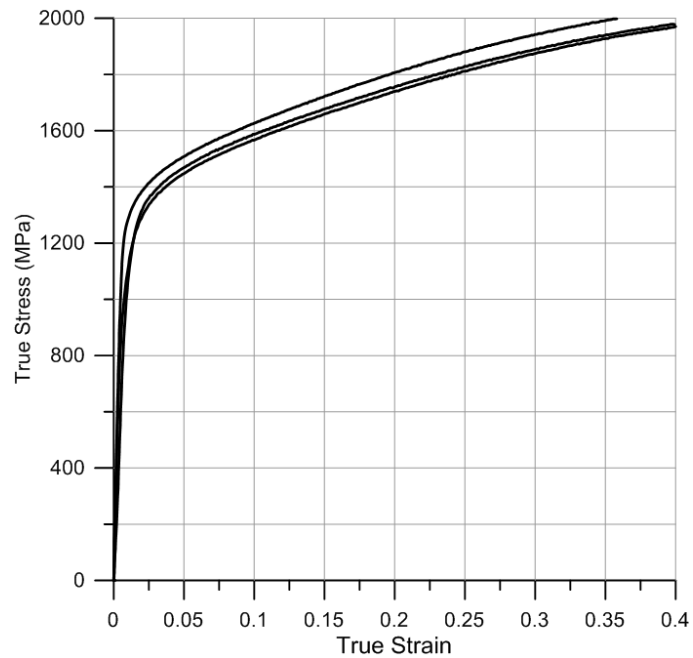


Figure B- 1. True stress versus true strain for compression experiments at 23 °C

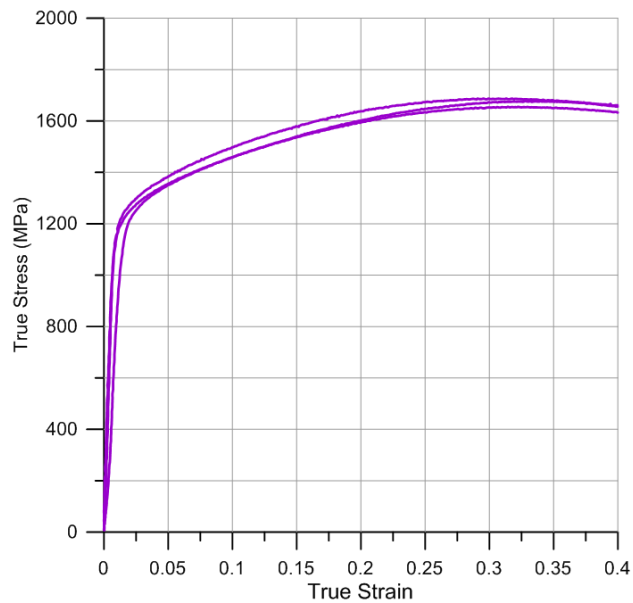


Figure B- 2. True stress versus true strain for compression experiments at 200 °C

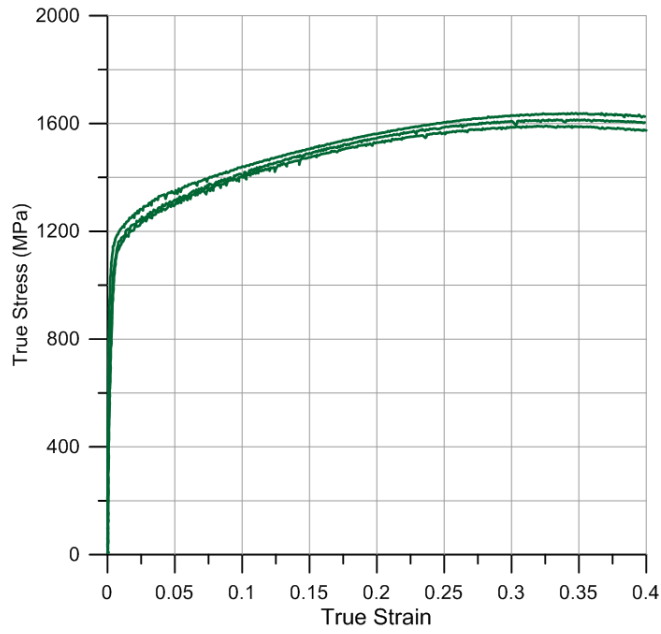


Figure B- 3. True stress versus true strain for compression experiments at 400 °C

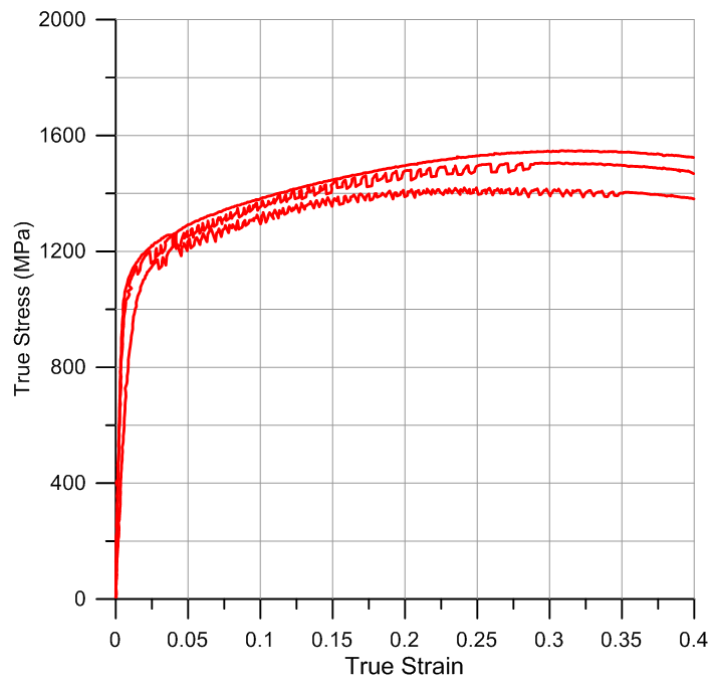


Figure B- 4. True stress versus true strain for compression experiments at 600 °C

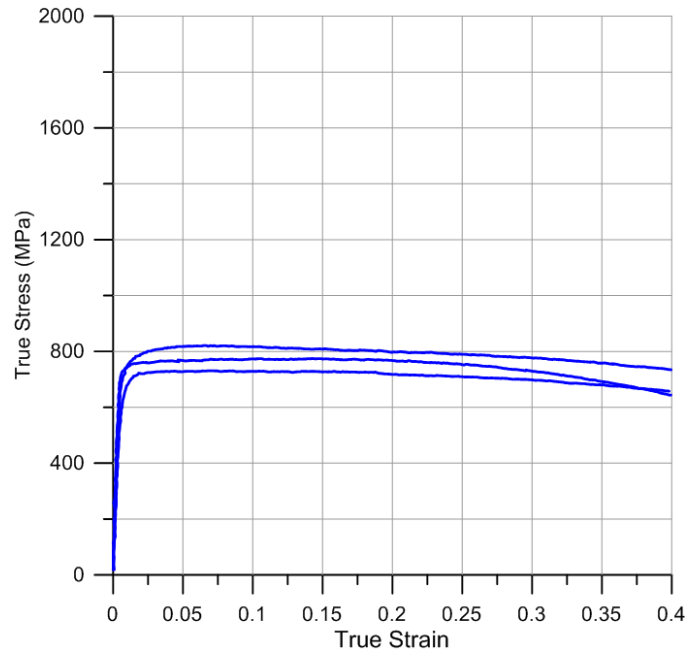


Figure B- 5. True stress versus true strain for compression experiments at 800 °C

C Anisotropy test results

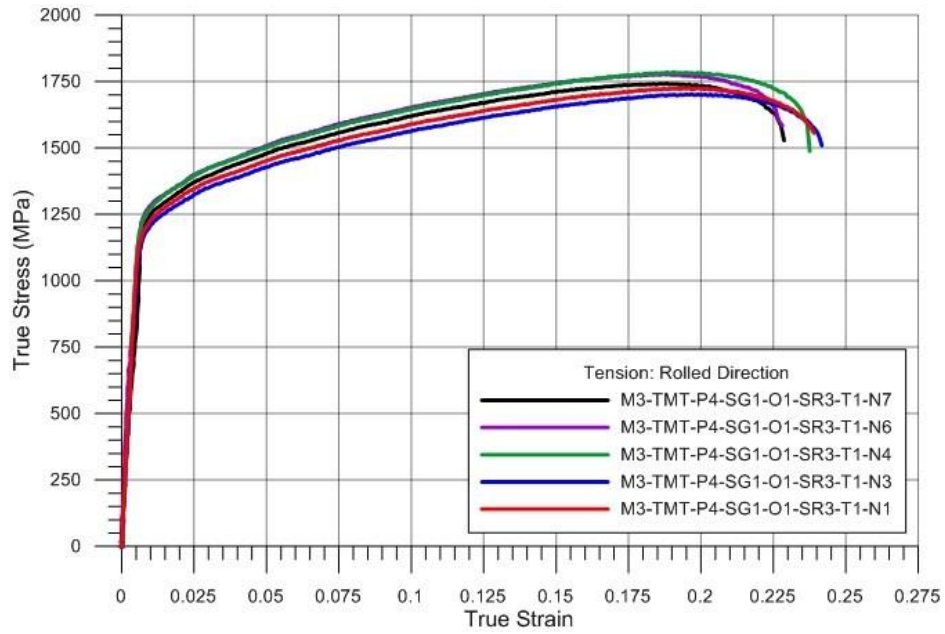


Figure C- 1. True stress vs true strain for tension experiments conducted at 1.0 s^{-1} in the rolled direction

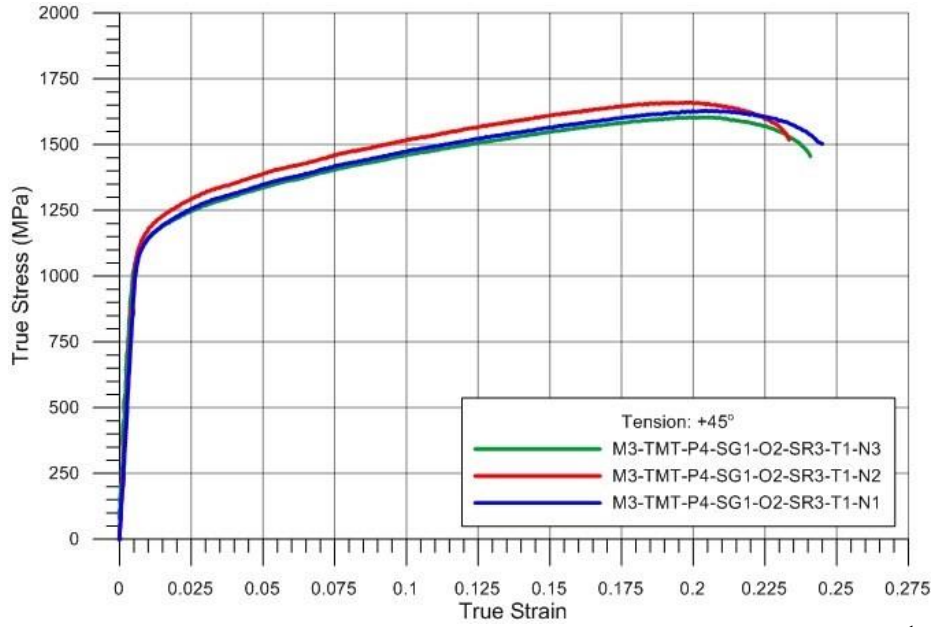


Figure C- 2. True stress vs true strain for tension experiments conducted at 1.0 s^{-1} in the $+45^\circ$ direction

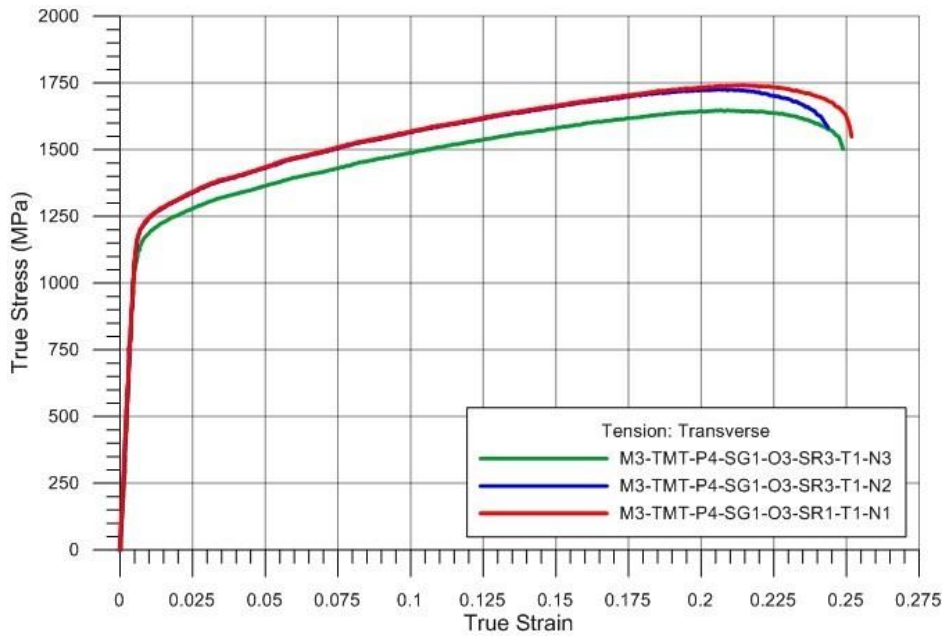


Figure C- 3. True stress vs true strain for tension experiments conducted at 1.0 s^{-1} in the transverse (90°) direction

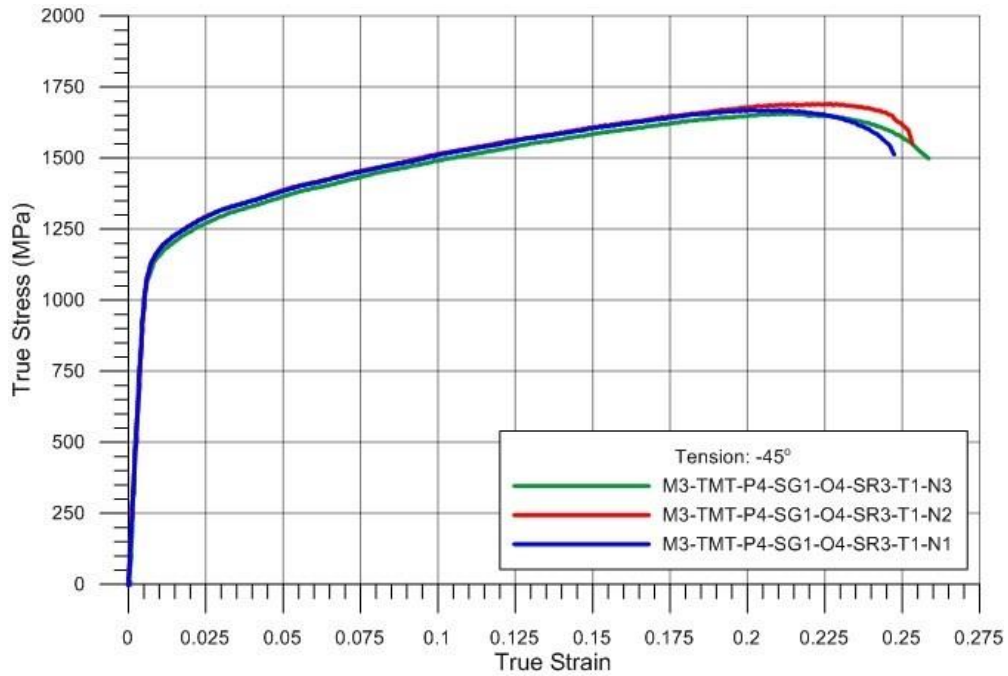


Figure C- 4. True stress vs true strain for tension experiments conducted at 1.0 s^{-1} in the -45° direction

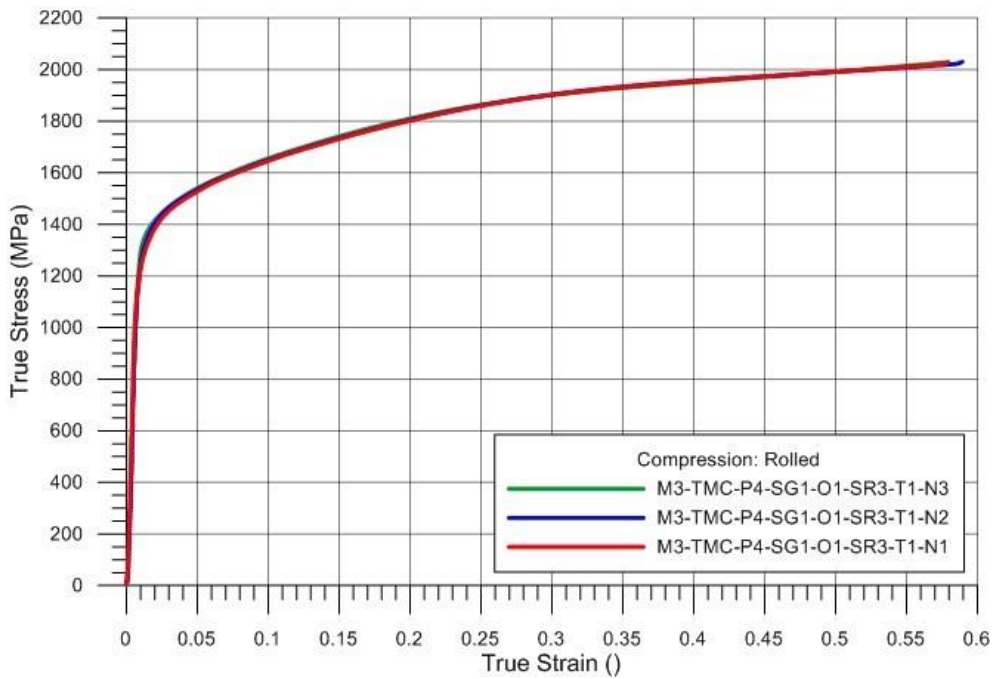


Figure C- 5. True stress vs true strain for compression experiments conducted at 1.0 s^{-1} in the rolled (0°) direction

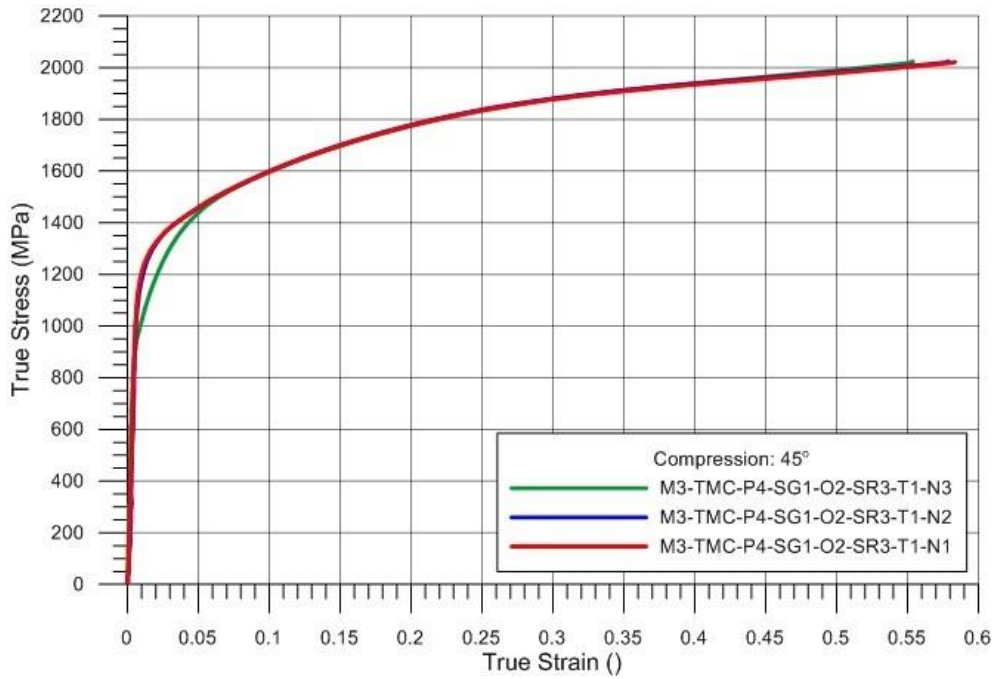


Figure C- 6. True stress vs true strain for compression experiments conducted at 1.0 s^{-1} in the $+45^\circ$ direction

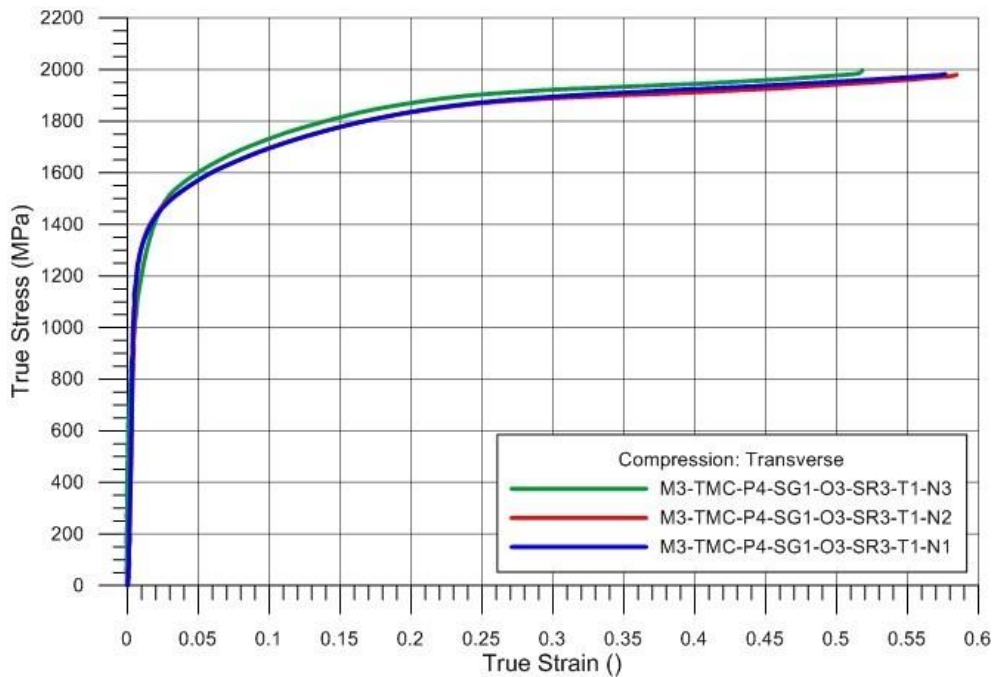


Figure C- 7. True stress vs true strain for compression experiments conducted at 1.0 s^{-1} in the transverse (90°) direction

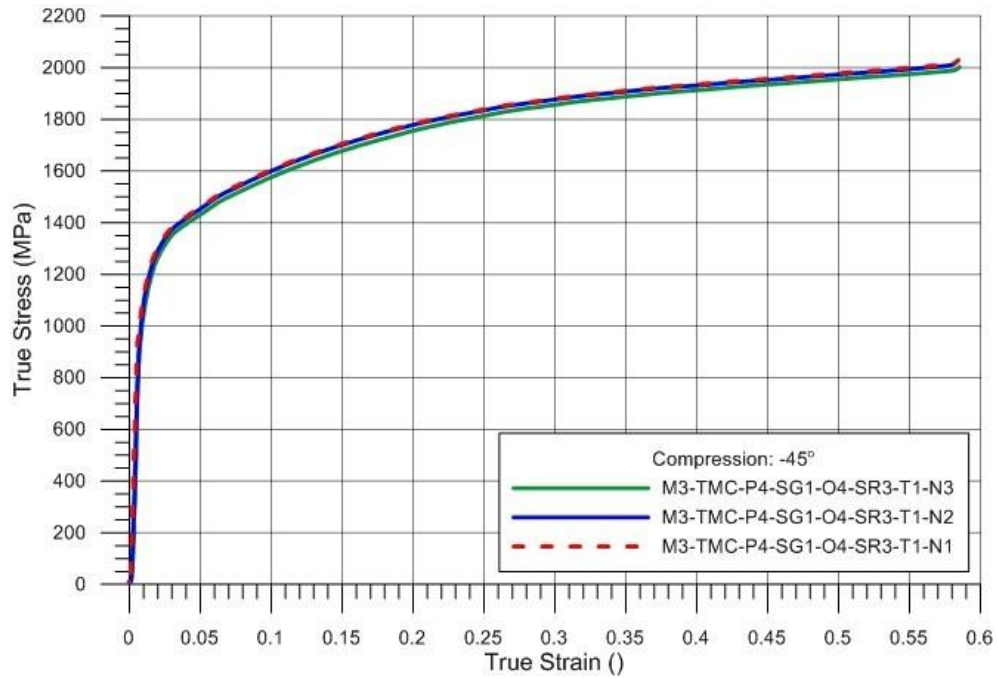


Figure C- 8. True stress vs true strain for compression experiments conducted at 1.0 s^{-1} in the -45° direction

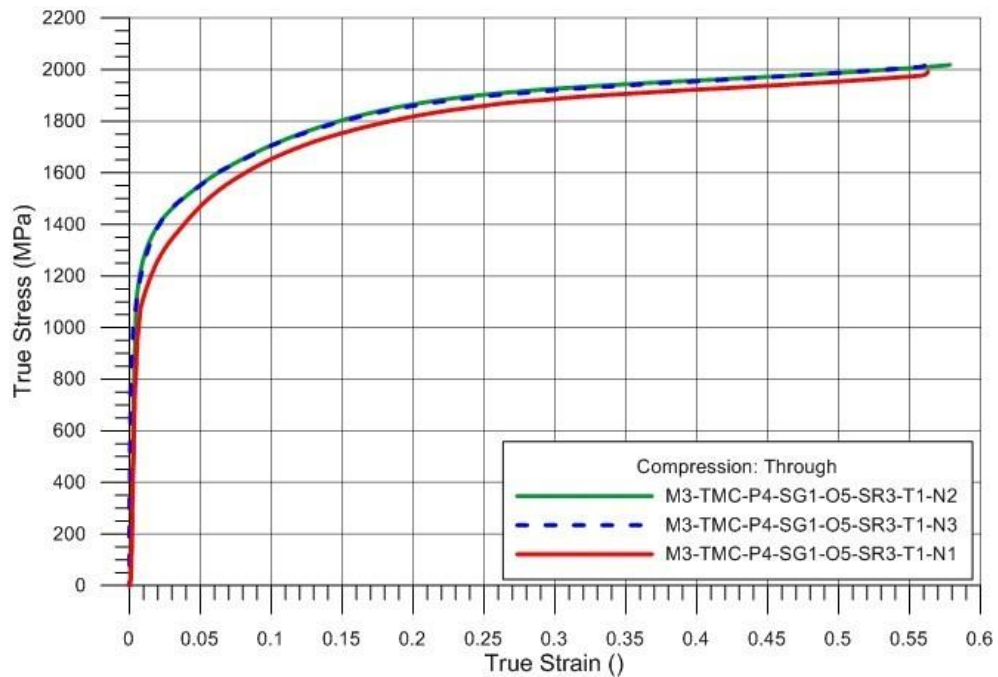


Figure C- 9. True stress vs true strain for compression experiments conducted at 1.0 s^{-1} in the through thickness direction

D Plate thickness test results

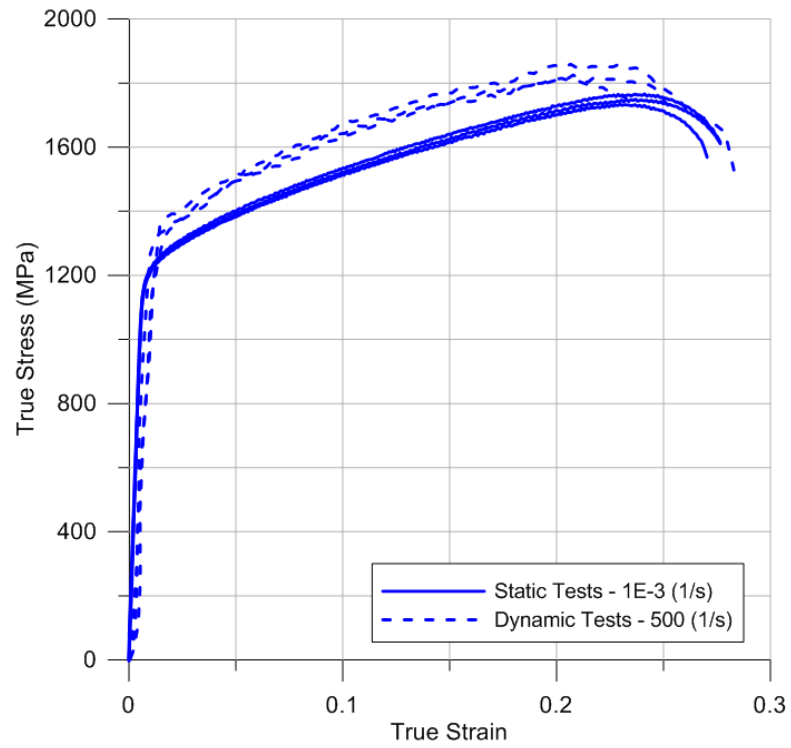


Figure D- 1. True stress versus true strain for plate P1 tension specimens tested at strain rates of 0.001 and 500 s⁻¹

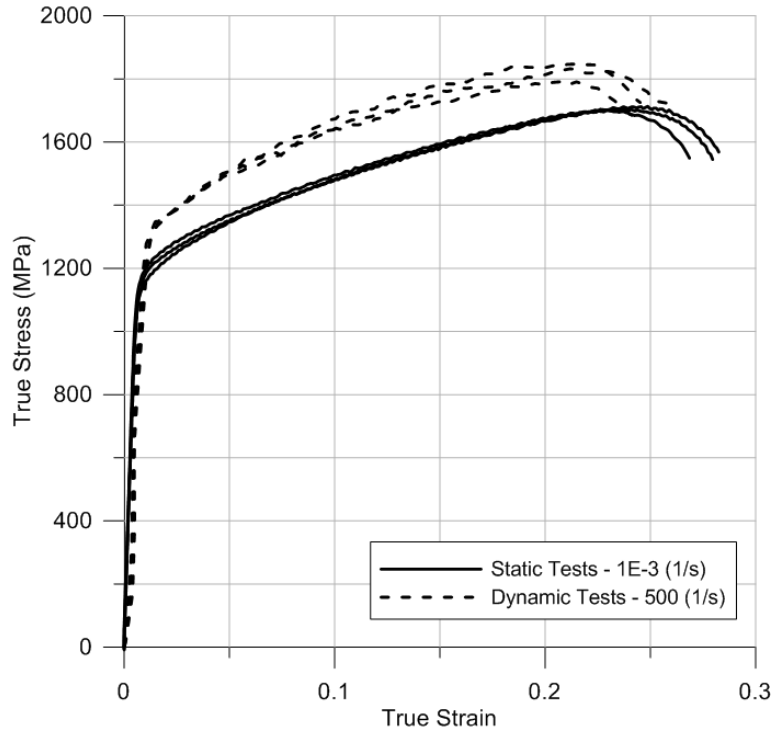


Figure D- 2. True stress versus true strain for plate P2 tension specimens tested at strain rates of 0.001 and 500 s⁻¹

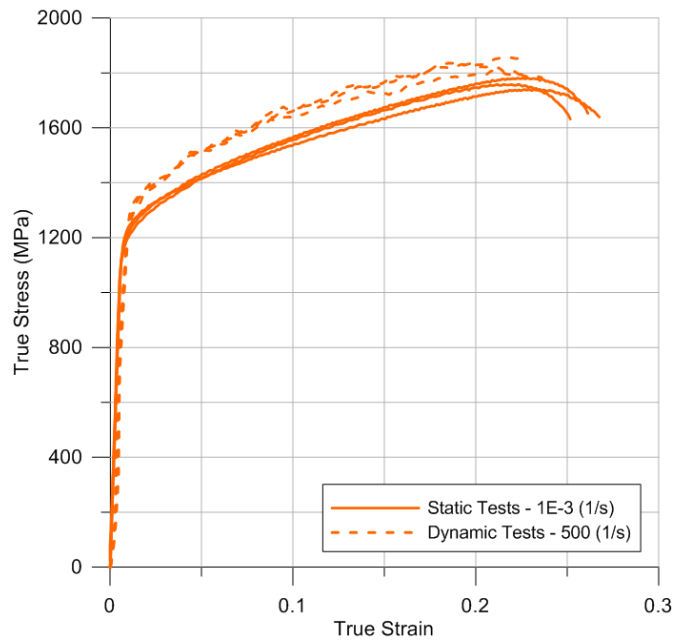


Figure D- 3. True stress versus true strain for plate P3 tension specimens tested at strain rates of 0.001 and 500 s⁻¹

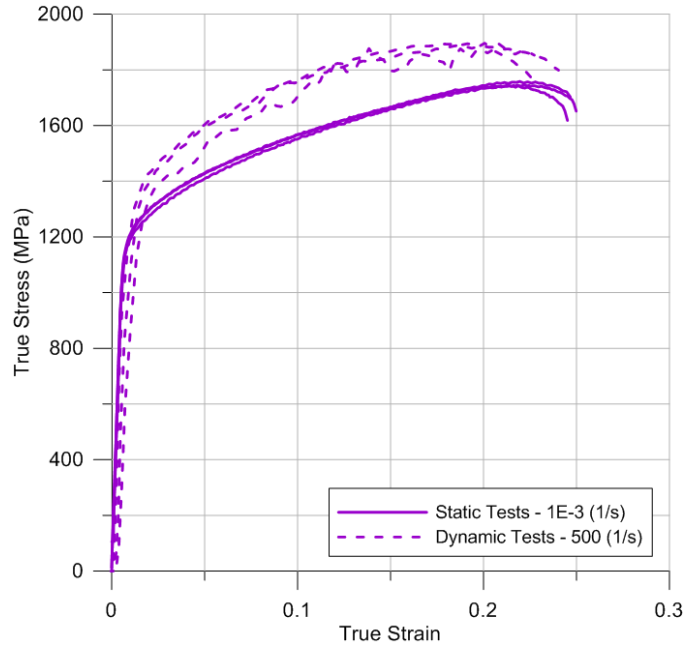


Figure D- 4. True stress versus true strain for plate P4 tension specimens tested at strain rates of 0.001 and 500 s⁻¹

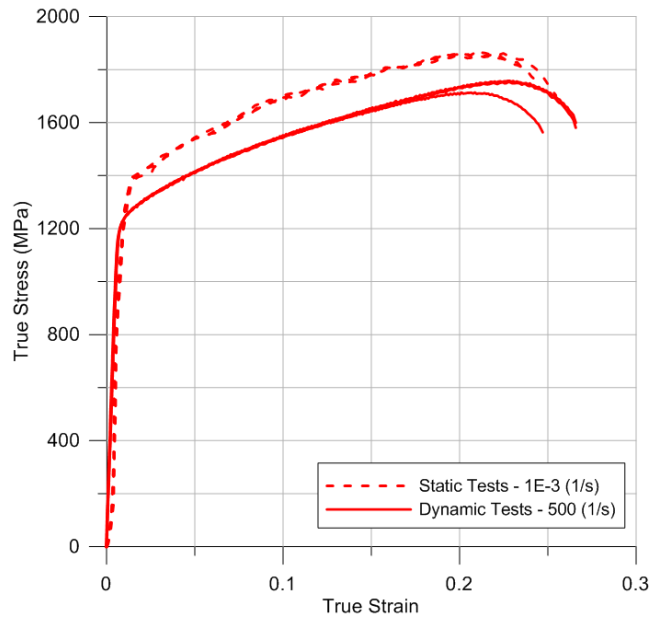


Figure D- 5. True stress versus true strain for plate P5 tension specimens tested at strain rates of 0.001 and 500

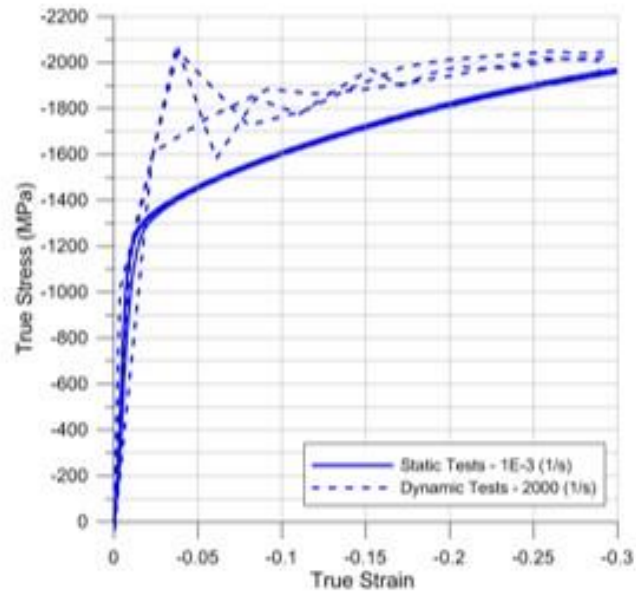


Figure D- 6. True stress versus true strain for plate P1 compression specimens tested at strain rates of 0.001 and 2000 s^{-1}

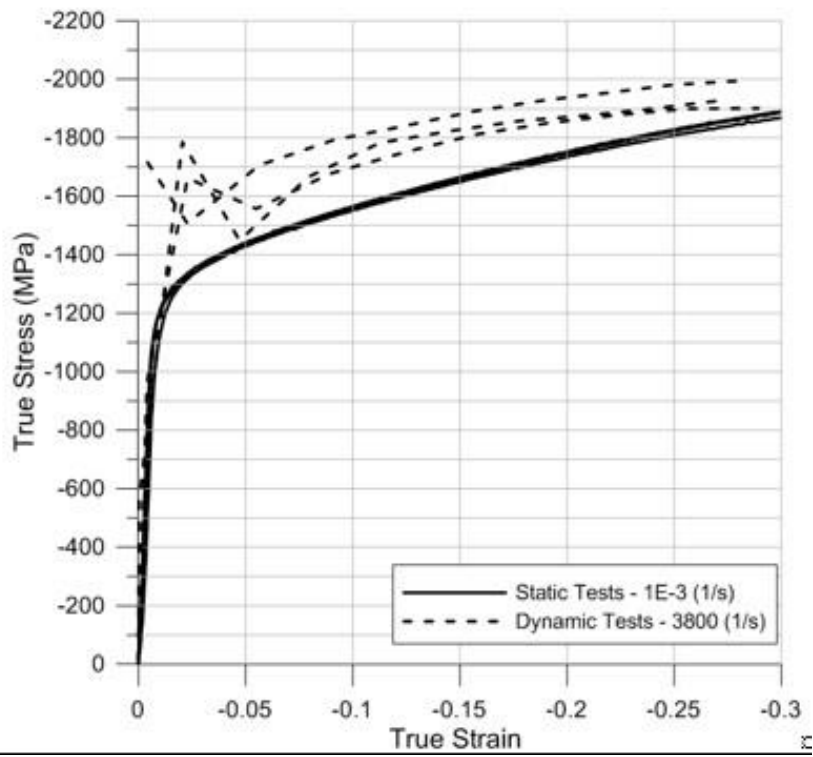


Figure D- 7. True stress versus true strain for plate P2 compression specimens tested at strain rates of 0.001 and 3800 s⁻¹

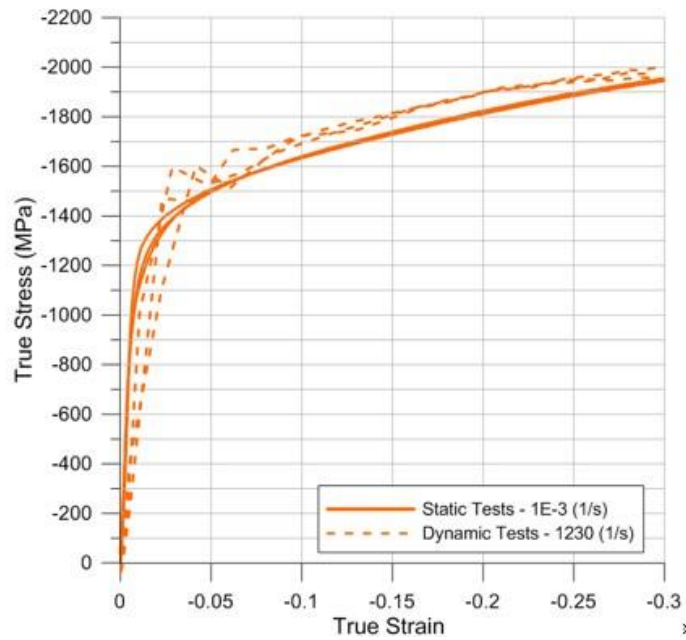


Figure D- 8. True stress versus true strain for plate P3 compression specimens tested at strain rates of 0.001 and 1230 s^{-1}

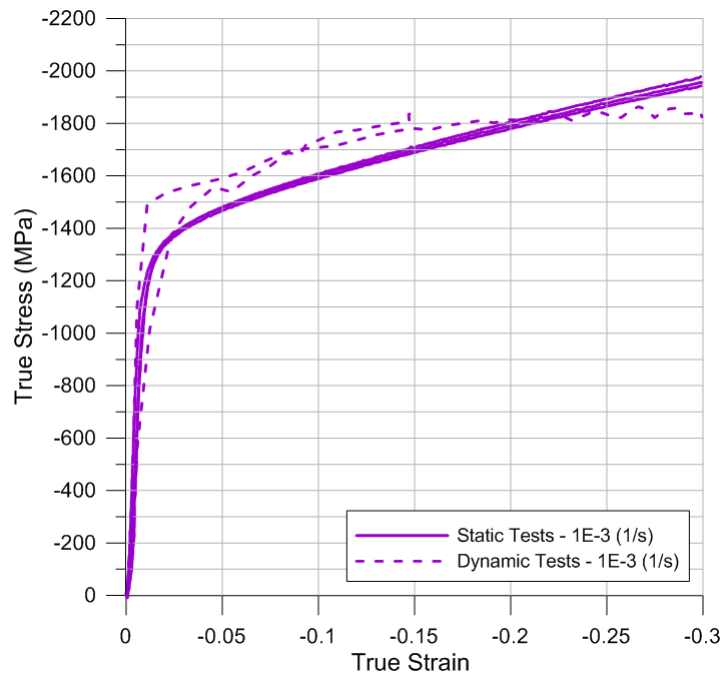
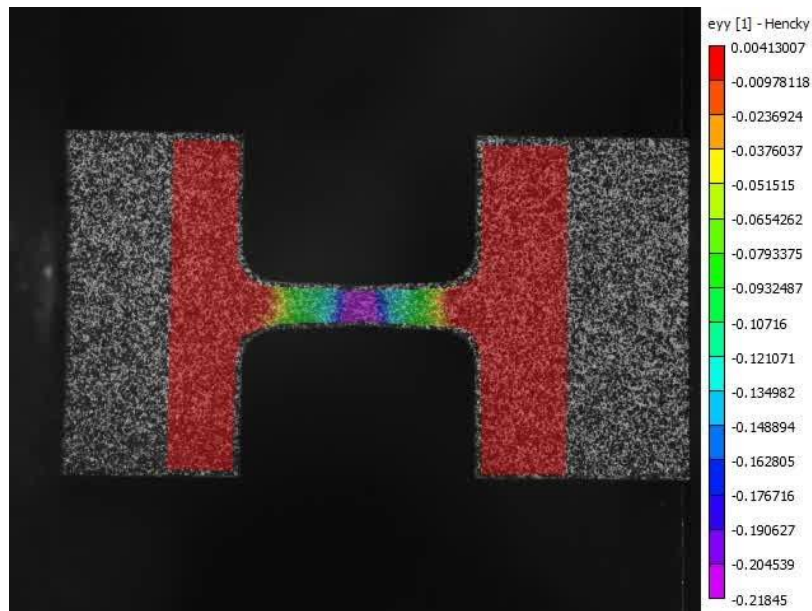
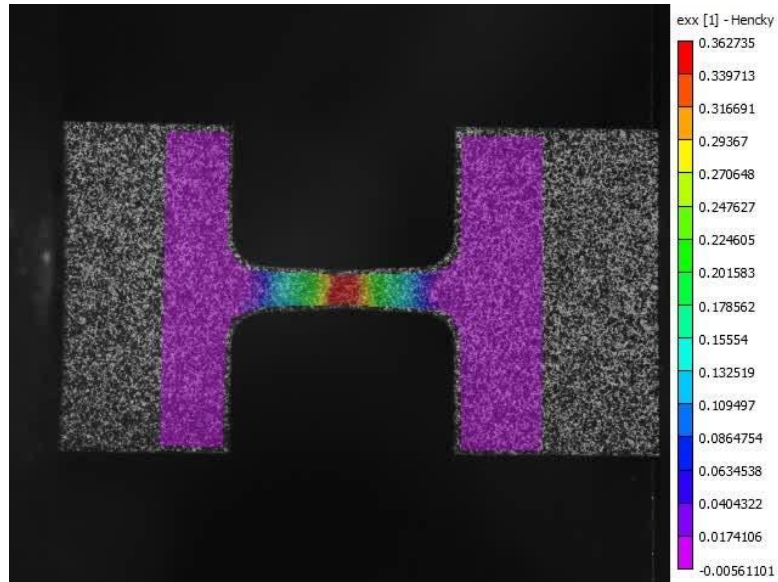


Figure D- 9. True stress versus true strain for plate P4 compression specimens tested at strain rates of 0.001 and 1000 s^{-1}

E DIC strain field immediately prior to fracture



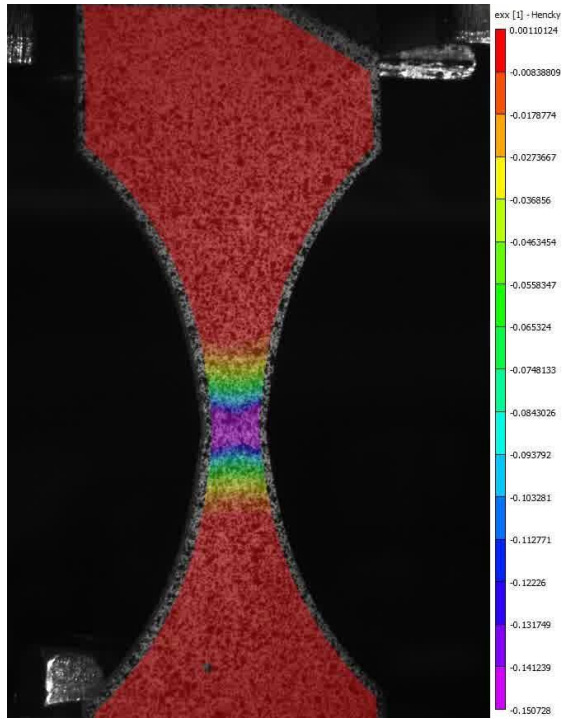


Figure E- 3. M3-TMT-P4-SG2-O1-SR6-T1-N1 ϵ_{xx}

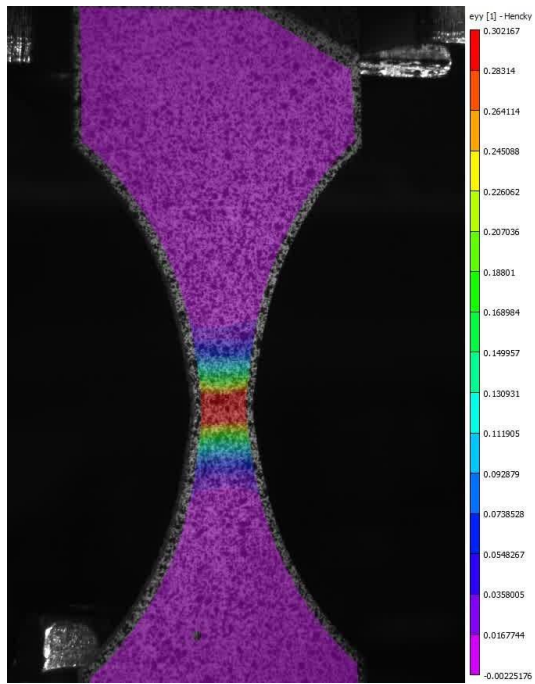


Figure E- 4. M3-TMT-P4-SG2-O1-SR6-T1-N1 ϵ_{yy}

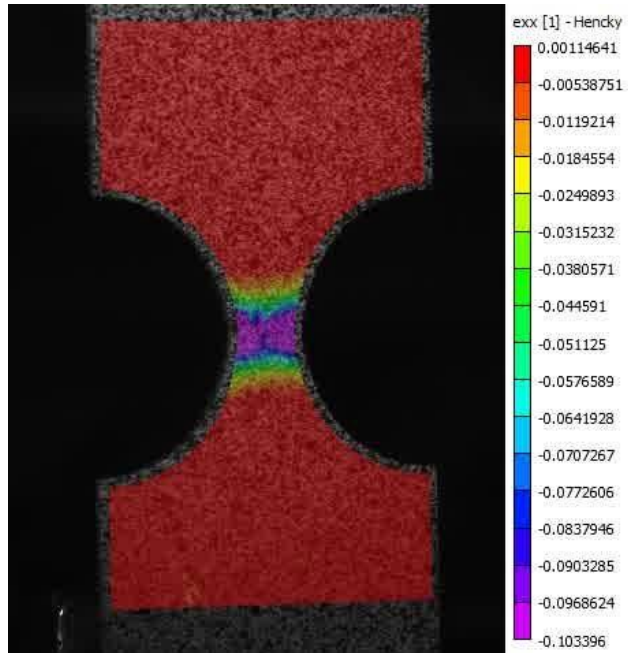


Figure E- 5. M3-TMT-P4-SG3-O1-SR6-T1-N1 ϵ_{xx}

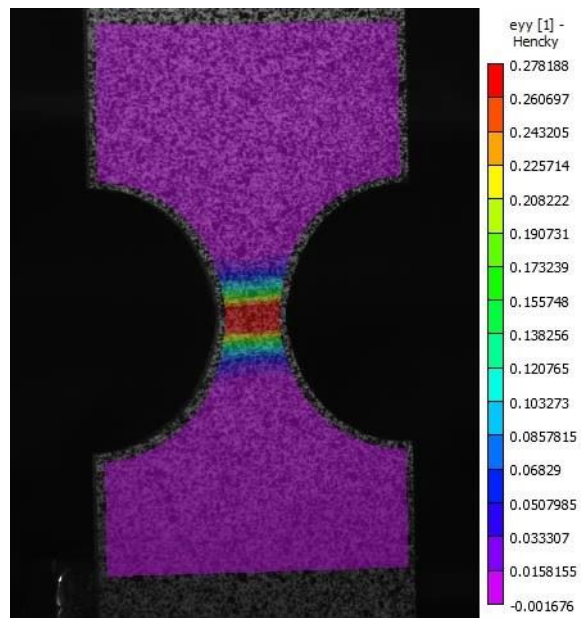


Figure E- 6. M3-TMT-P4-SG3-O1-SR6-T1-N1 ϵ_{yy}

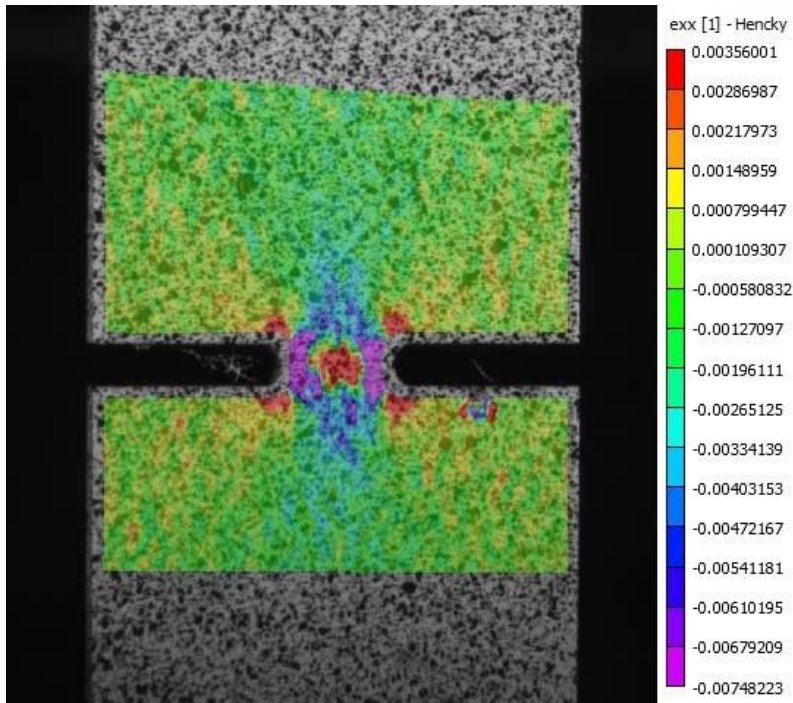


Figure E- 7. M3-TMT-P4-SG3-O1-SR6-T1-N1 ϵ_{xx}

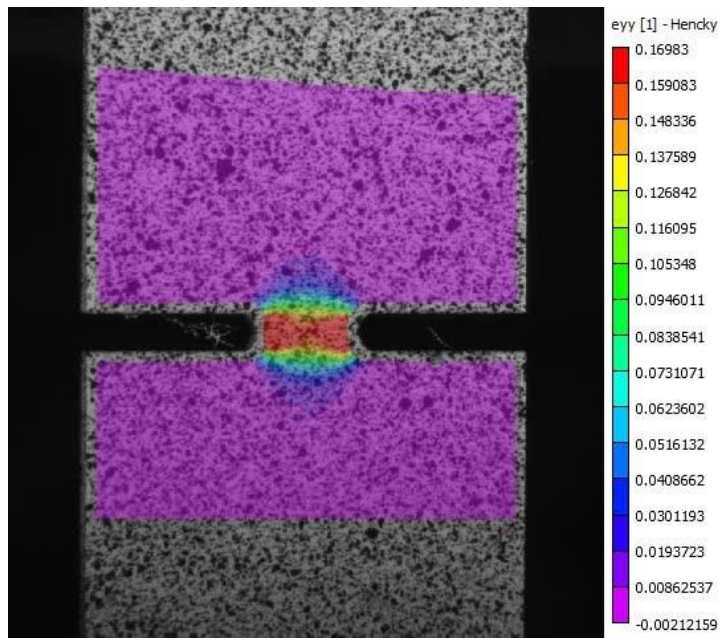


Figure E- 8. M3-TMT-P4-SG4-O1-SR6-T1-N1 ϵ_{yy}

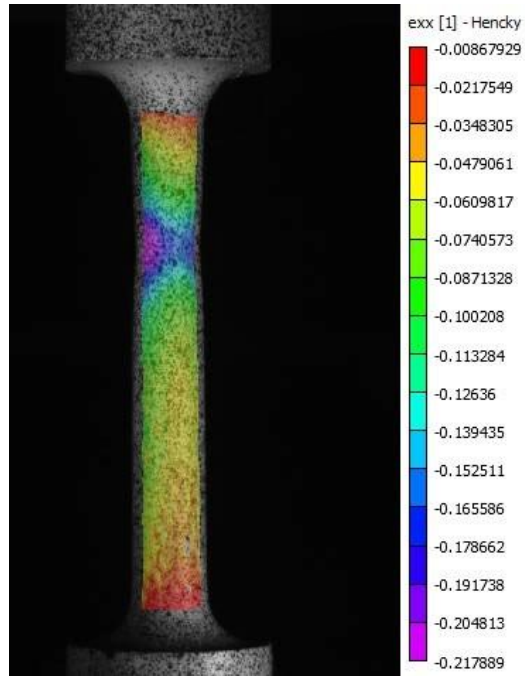


Figure E- 9. M3-TMT-P4-SG5-O1-SR6-T1-N2 ϵ_{xx}

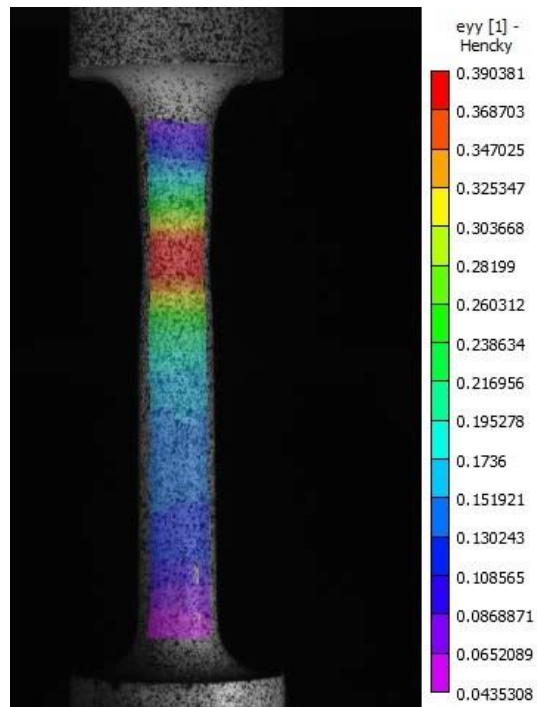


Figure E- 10. M3-TMT-P4-SG5-O1-SR6-T1-N2 ϵ_{yy}

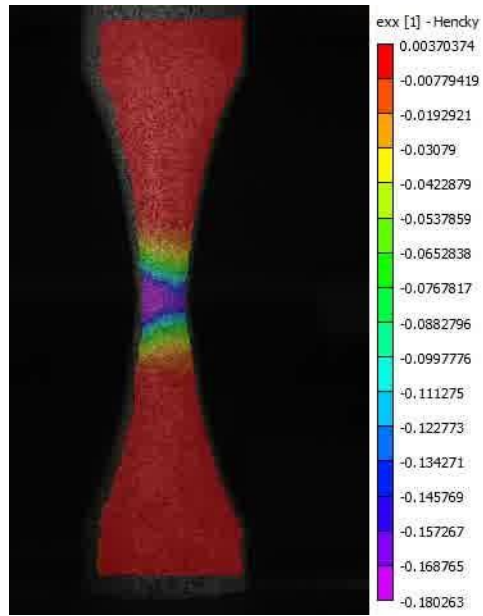


Figure E- 11. M3-TMT-P4-SG6-O1-SR6-T1-N1 ϵ_{xx}

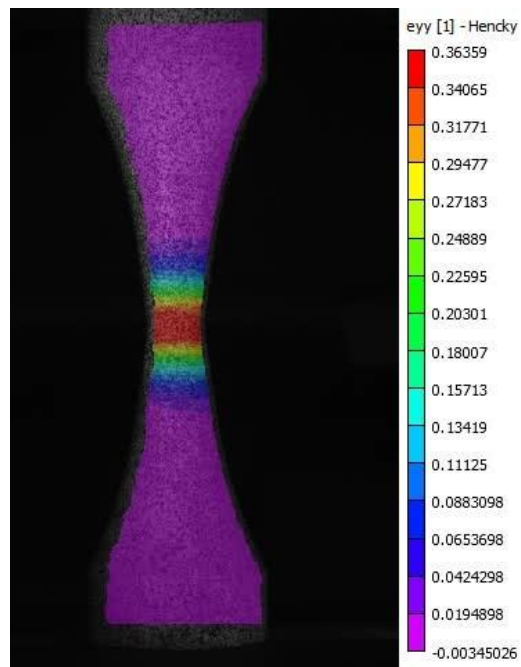


Figure E- 12. M3-TMT-P4-SG6-O1-SR6-T1-N1 ϵ_{yy}

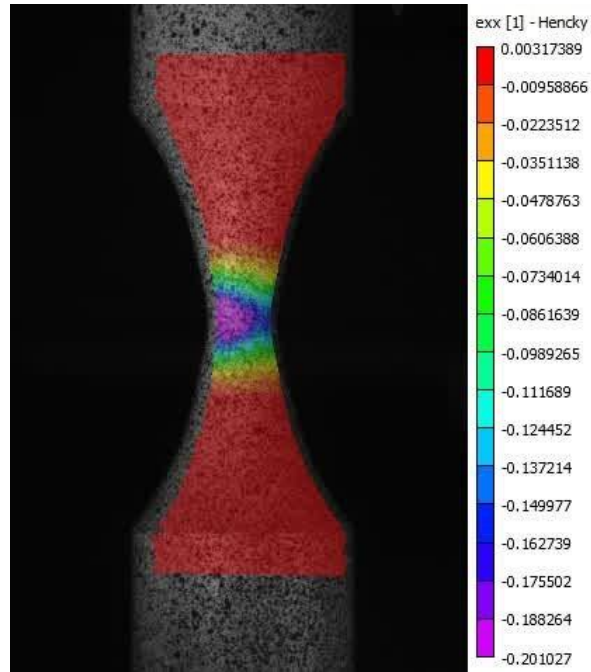


Figure E- 13. M3-TMT-P4-SG7-O1-SR6-T1-N1 ϵ_{xx}

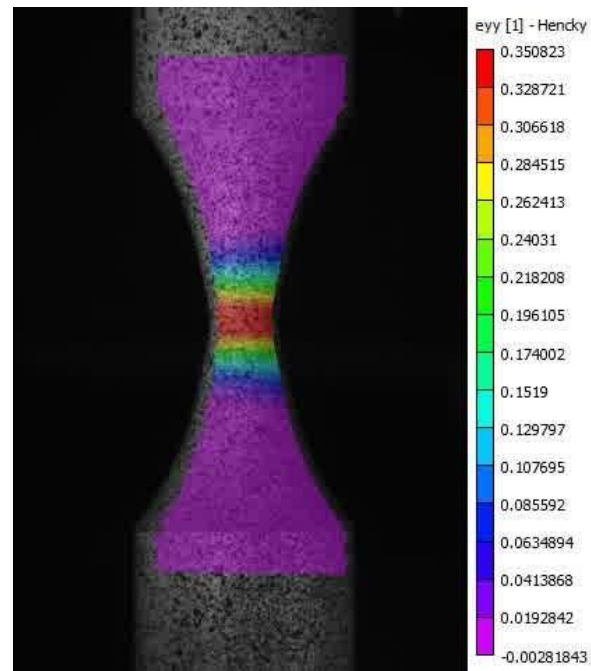


Figure E- 14. M3-TMT-P4-SG7-O1-SR6-T1-N1 ϵ_{yy}

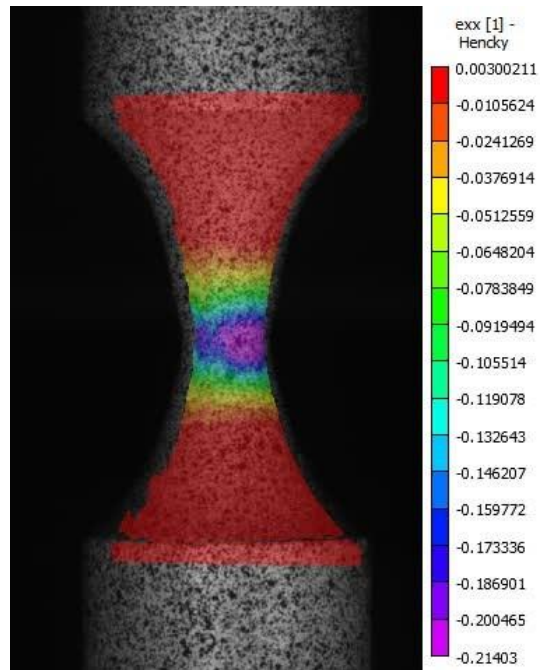


Figure E- 15. M3-TMT-P4-SG8-O1-SR6-T1-N1 ϵ_{xx}

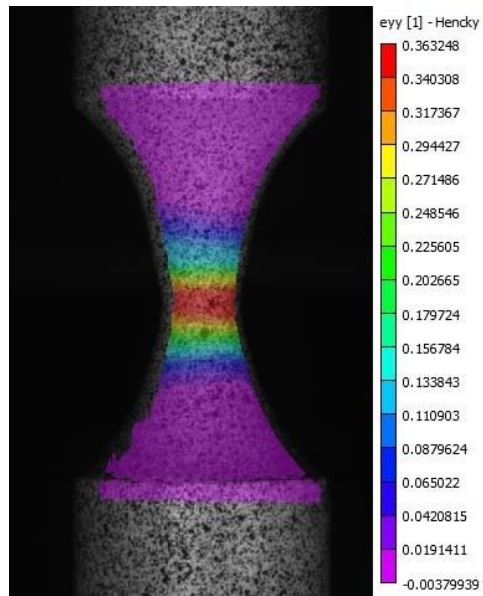


Figure E- 16. M3-TMT-P4-SG8-O1-SR6-T1-N1 ϵ_{yy}

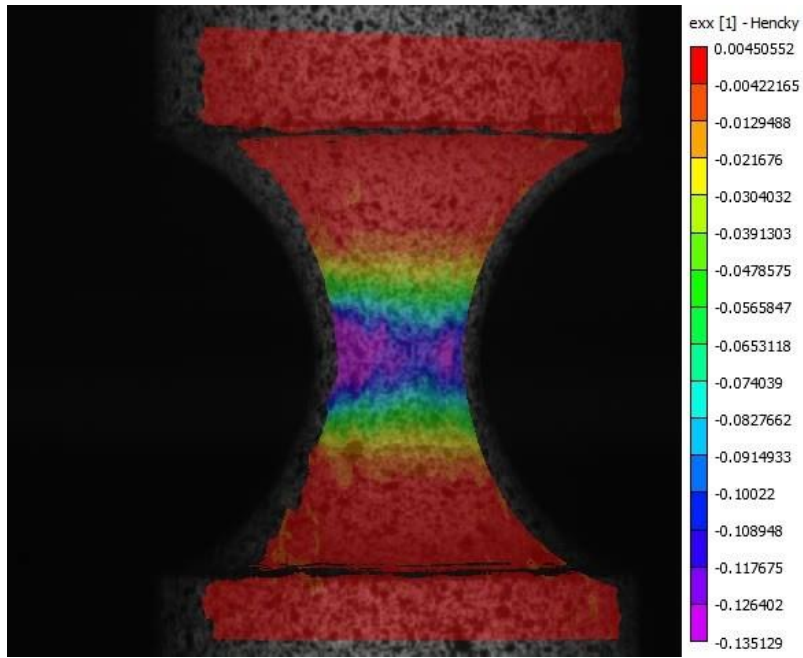


Figure E- 17. M3-TMT-P4-SG9-O1-SR6-T1-N1 ϵ_{xx}

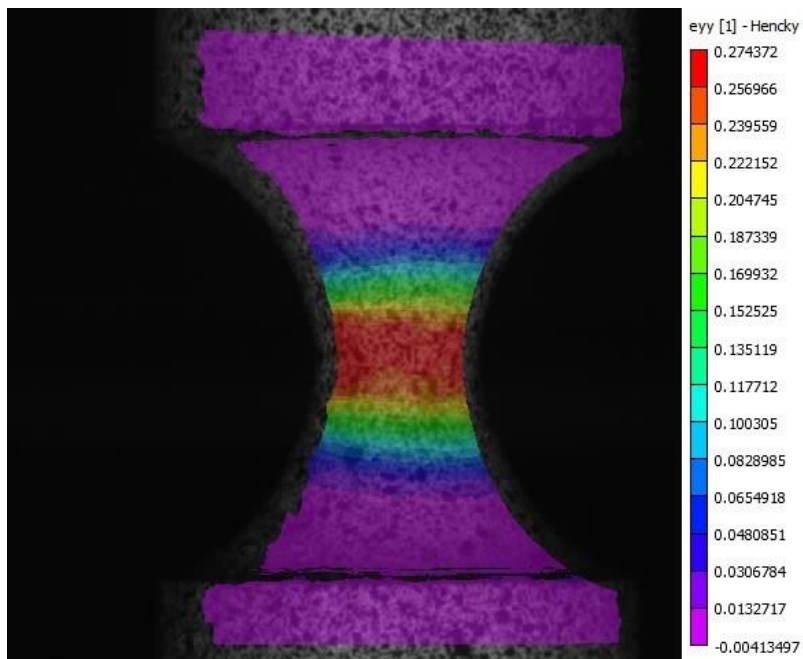


Figure E- 18. M3-TMT-P4-SG9-O1-SR6-T1-N1 ϵ_{yy}

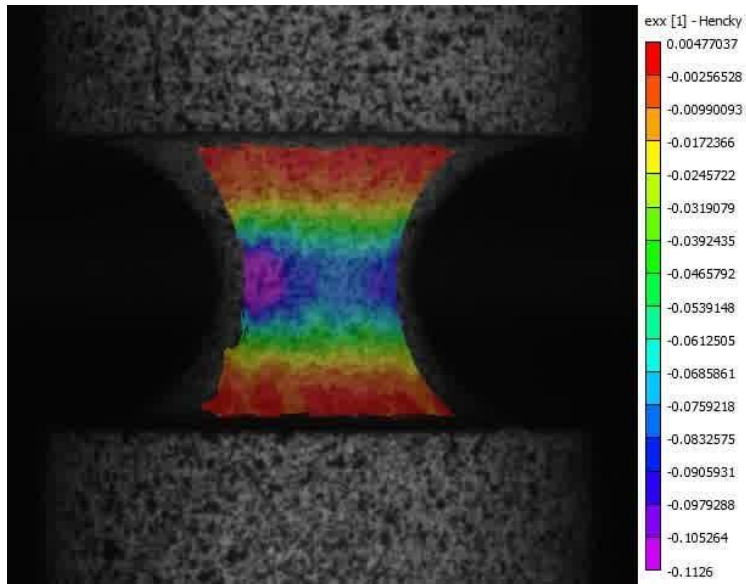


Figure E- 19. M3-TMT-P4-SG10-O1-SR6-T1-N1 ϵ_{xx}

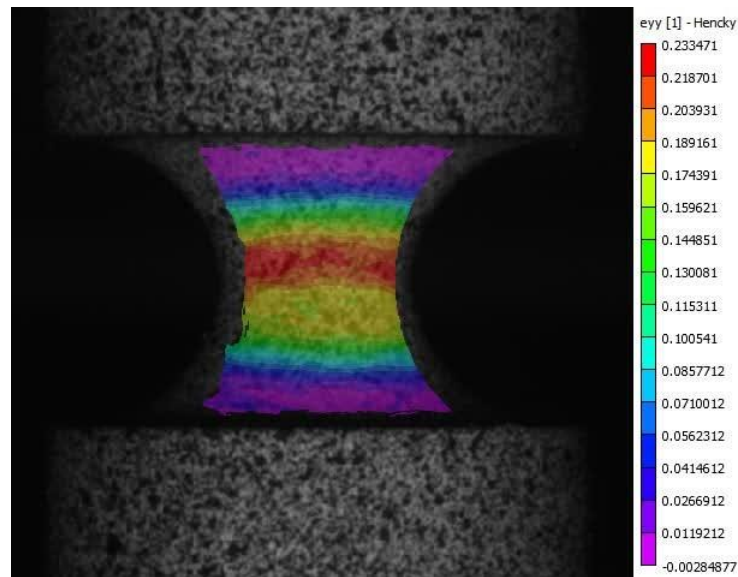


Figure E- 20. M3-TMT-P4-SG10-O1-SR6-T1-N1 ϵ_{yy}

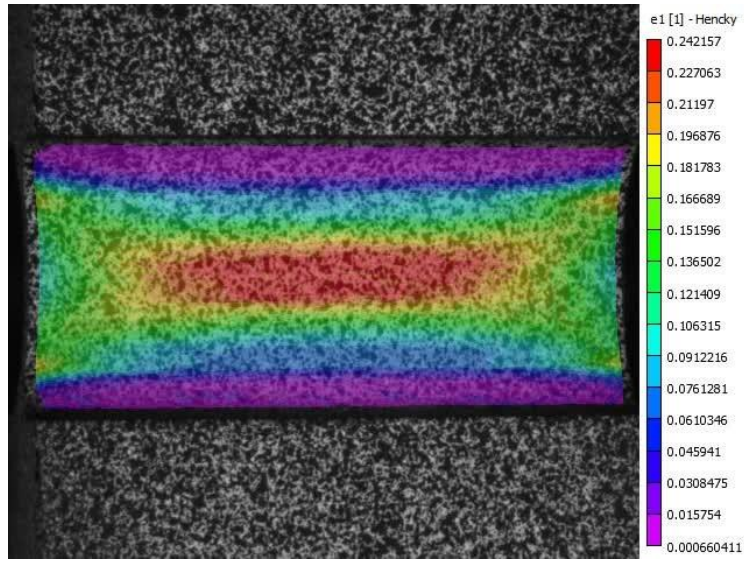


Figure E- 21. M3-TMT-P4-SG11-O1-SR6-T1-N2 ε_1

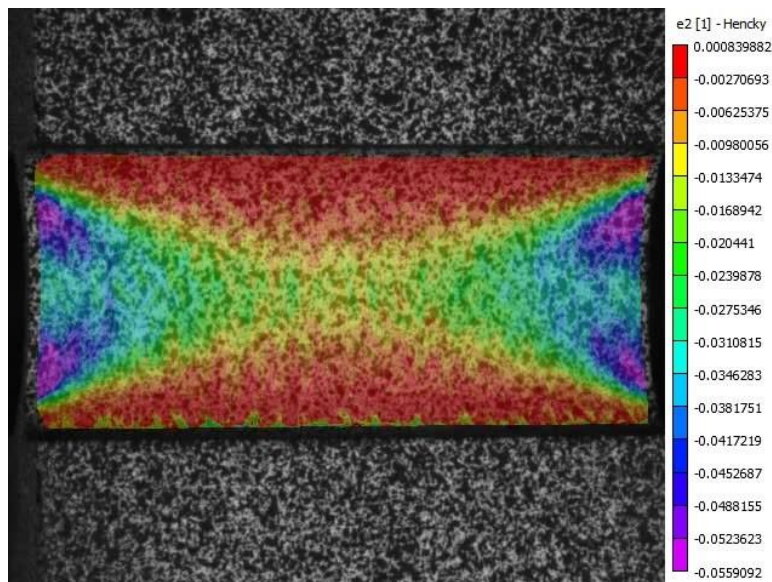


Figure E- 22. M3-TMT-P4-SG11-O1-SR6-T1-N2 ε_2

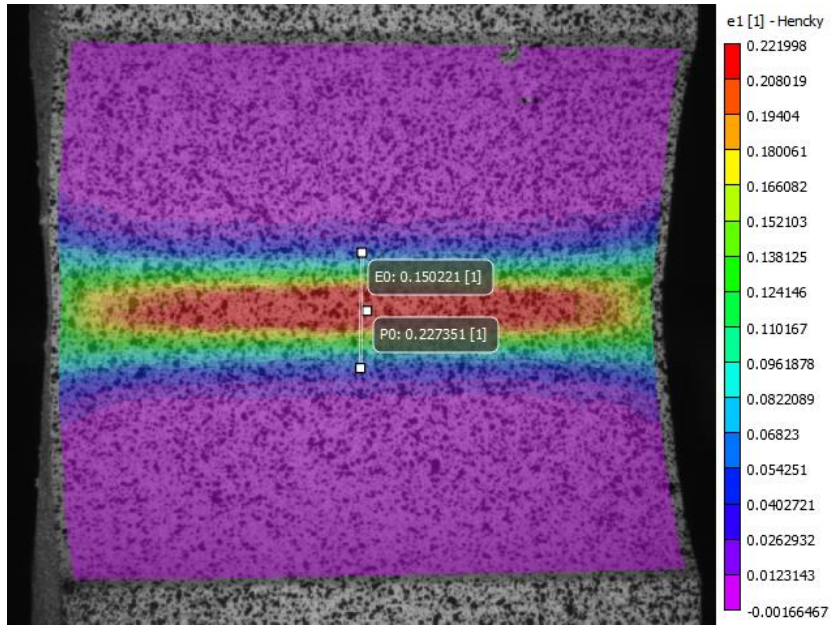


Figure E- 23. M3-TMT-P4-SG12-O1-SR6-T1-N1 ϵ_1

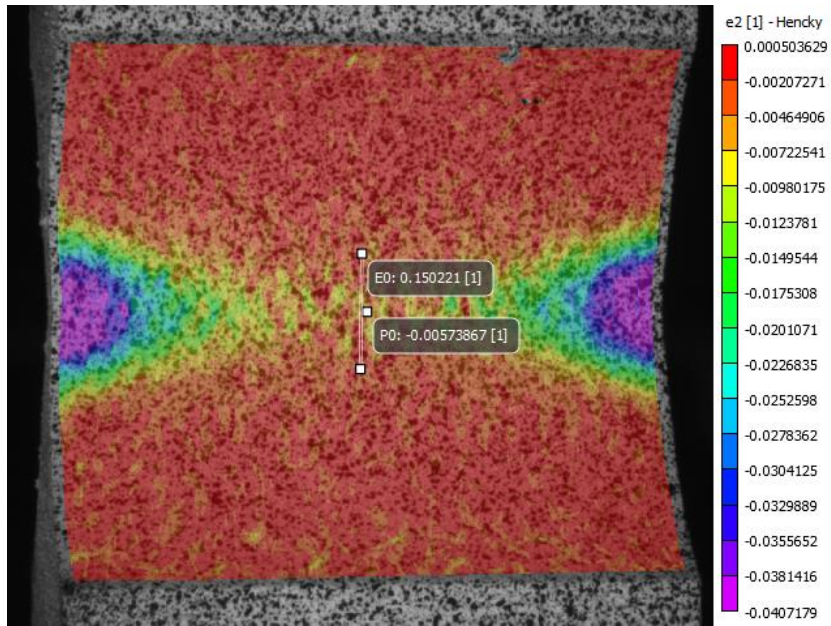


Figure E- 24. M3-TMT-P4-SG12-O1-SR6-T1-N2 ϵ_2

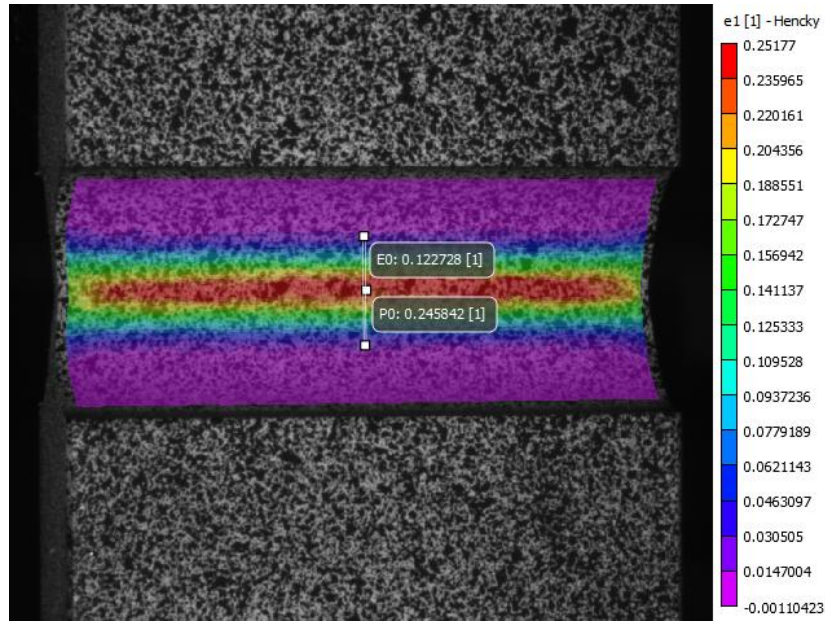


Figure E- 25. M3-TMT-P4-SG13-O1-SR6-T1-N1 ϵ_1

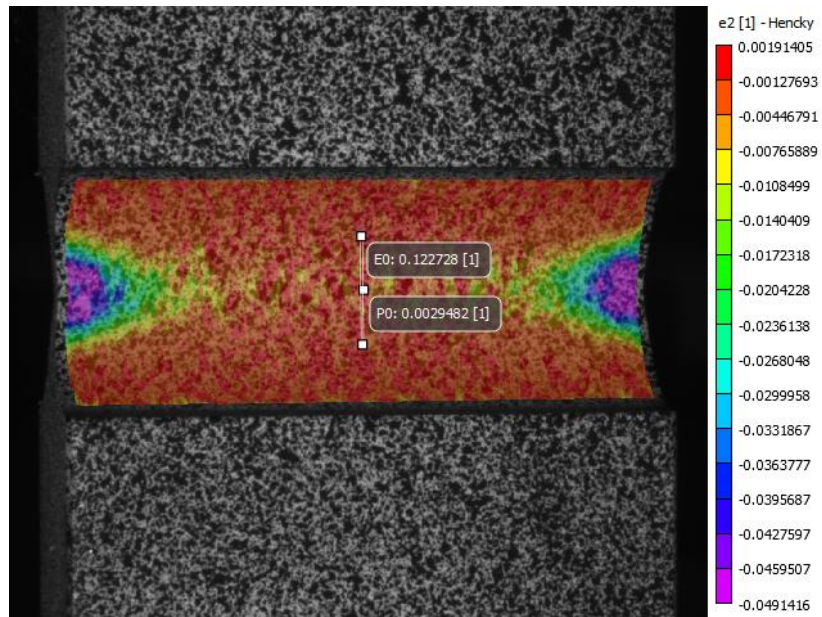


Figure E- 26. M3-TMT-P4-SG13-O1-SR6-T1-N1 ϵ_2

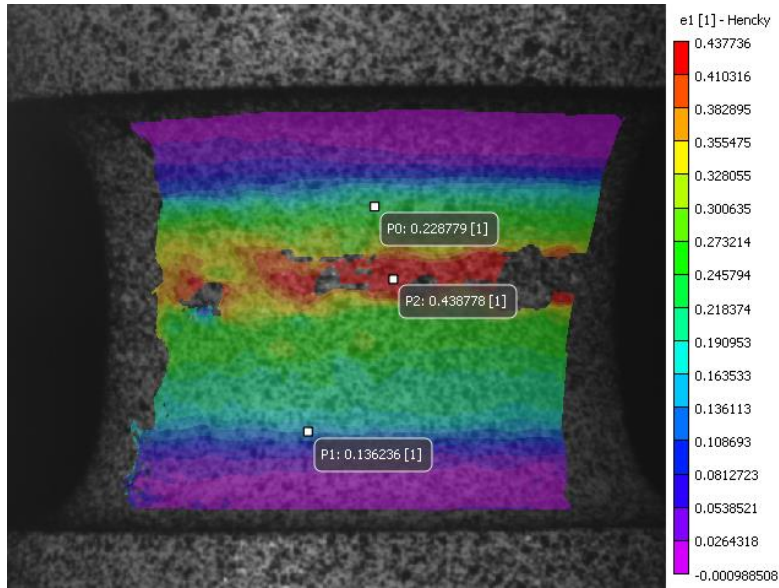


Figure E- 27. M3-TMCL-LR1-P4-SR6-T1-N4 ϵ_1

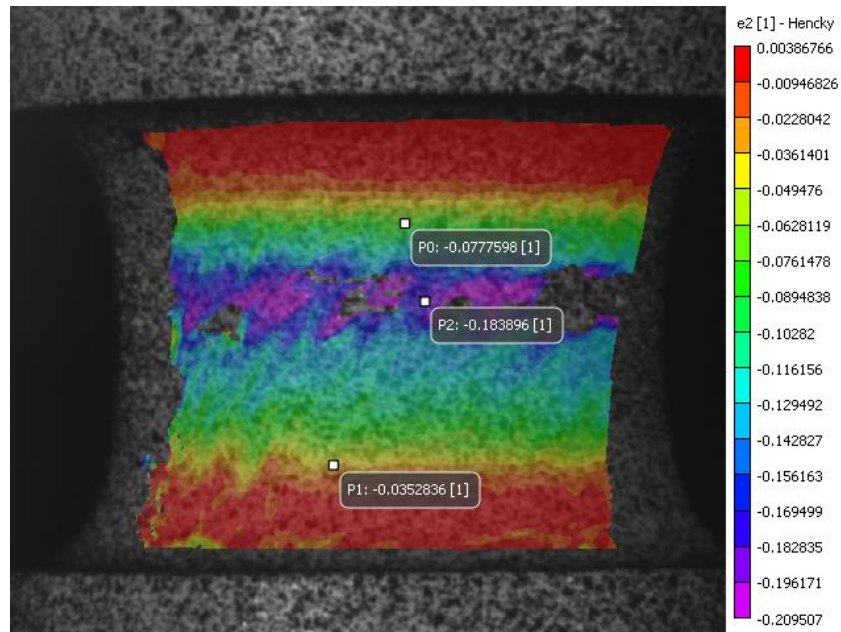


Figure E- 28. M3-TMCL-LR1-P4-SR6-T1-N4 ϵ_2

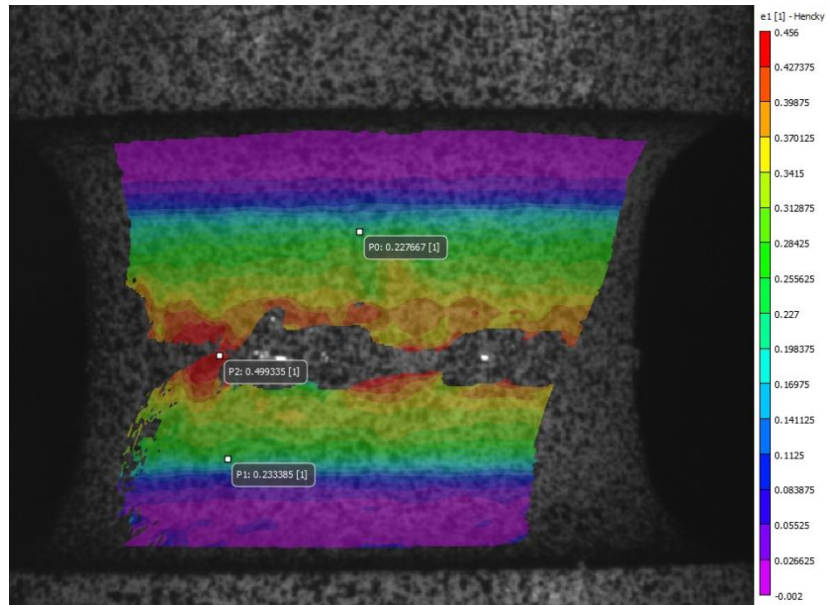


Figure E- 29. M3-TMCL-LR2-P4-SR6-T1-N1 ϵ_1

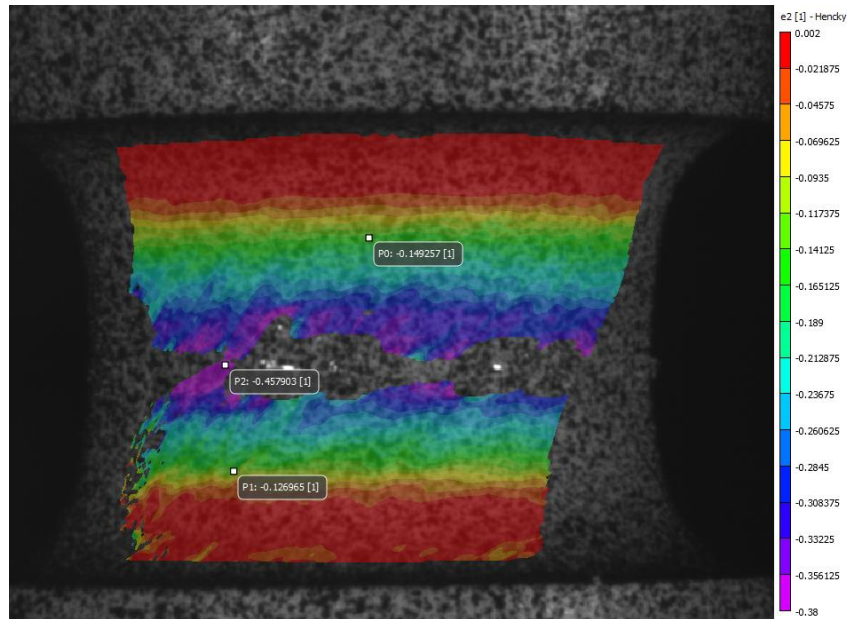


Figure E- 30. M3-TMCL-LR2-P4-SR6-T1-N1 ϵ_2

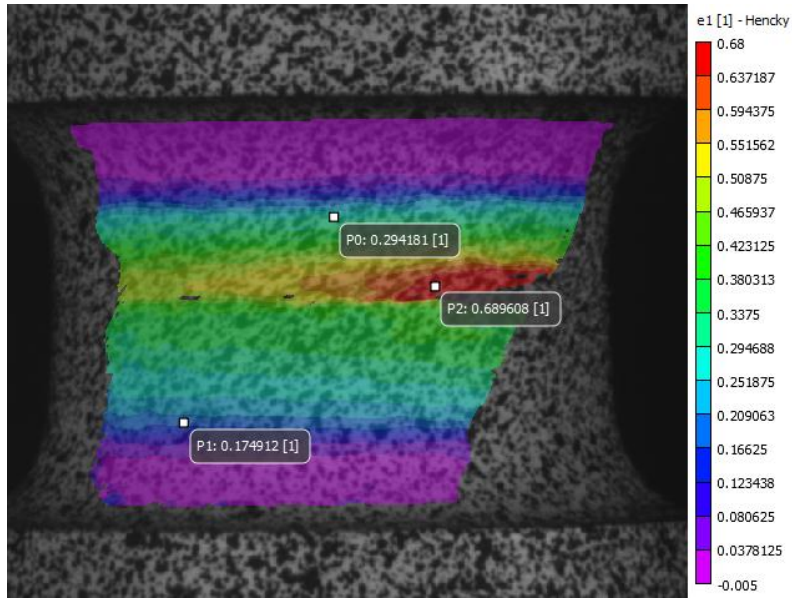


Figure E- 31. M3-TMCL-LR3-P4-SR6-T1-N3 ϵ_1

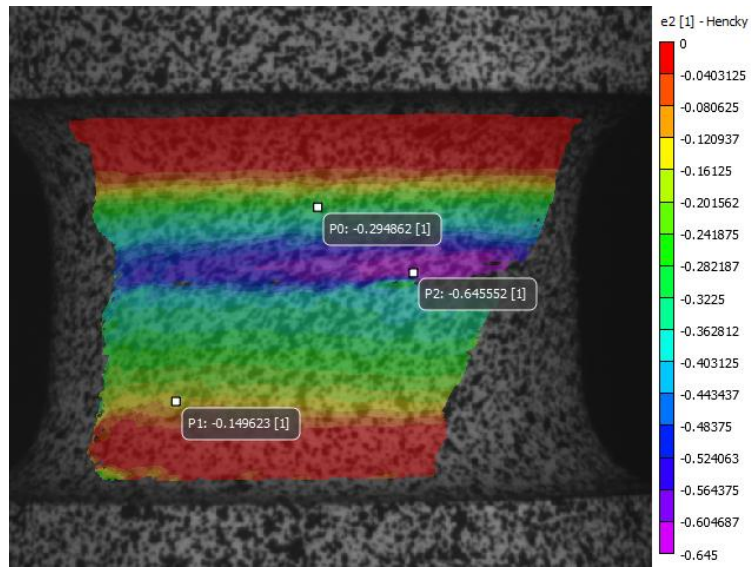


Figure E- 32. M3-TMCL-LR3-P4-SR6-T1-N3 ϵ_2

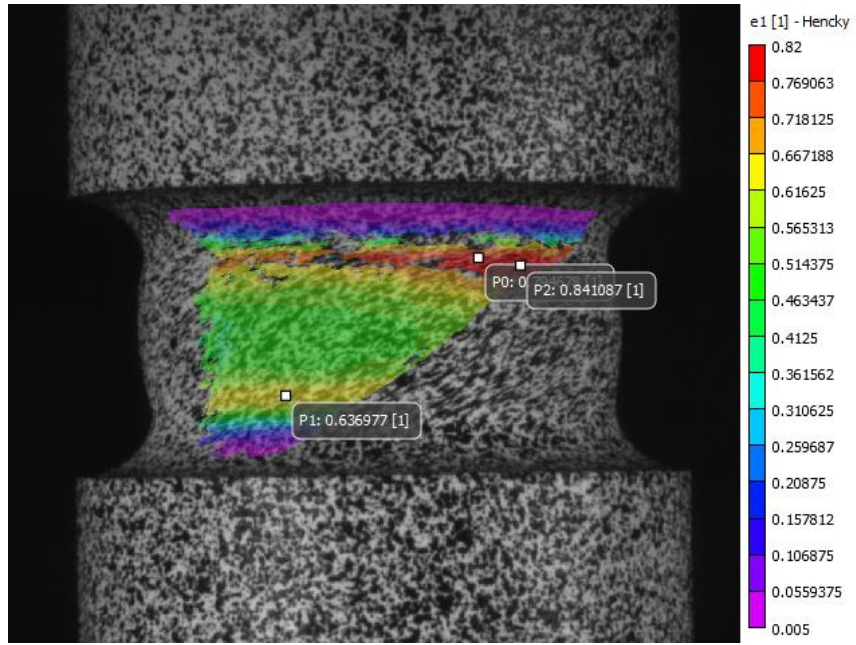


Figure E- 33. M3-TMCL-LR4-P4-SR6-T1-N5 ϵ_1

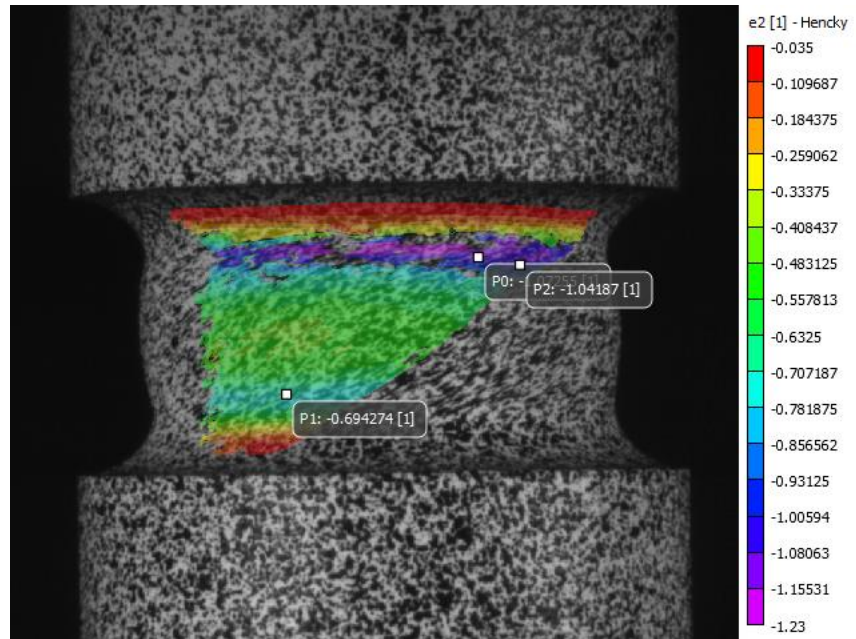


Figure E- 34. M3-TMCL-LR4-P4-SR6-T1-N5 ϵ_2

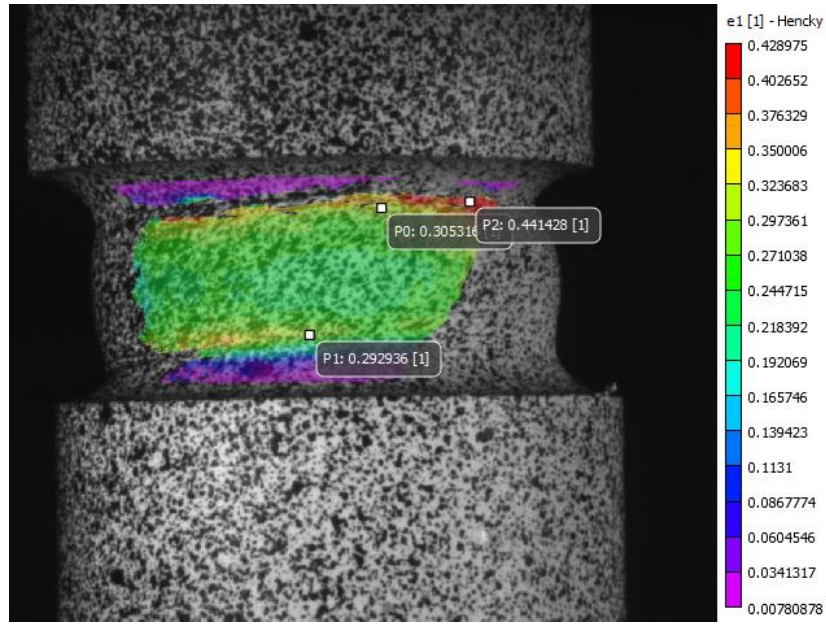


Figure E- 35. M3-TMCL-LR5-P4-SR6-T1-N1 ϵ_1

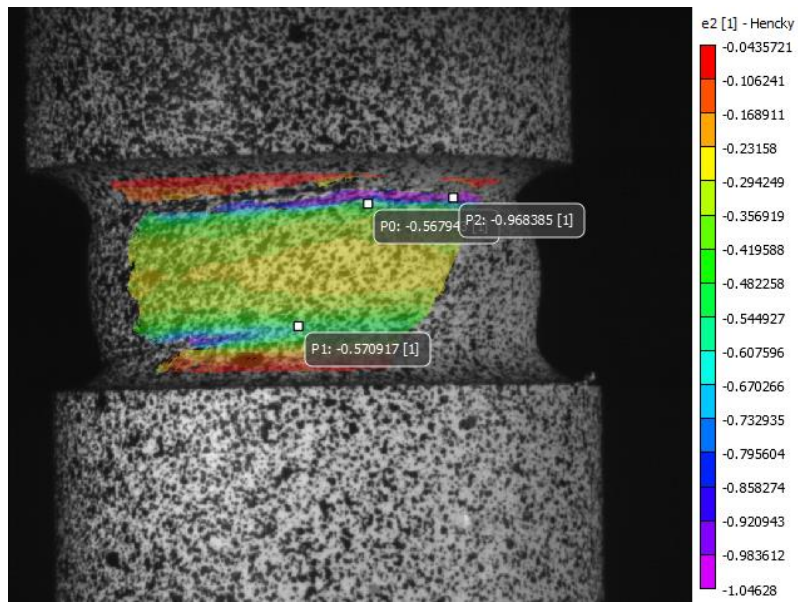


Figure E- 36. M3-TMCL-LR5-P4-SR6-T1-N1 ϵ_2

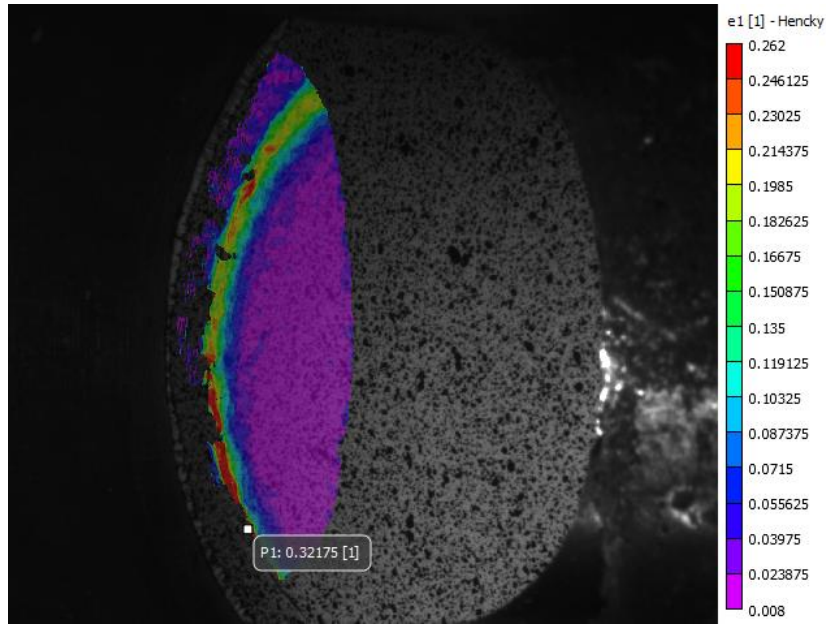


Figure E- 37. M3-TMP1-P4-SR6-T1-N1 ϵ_1

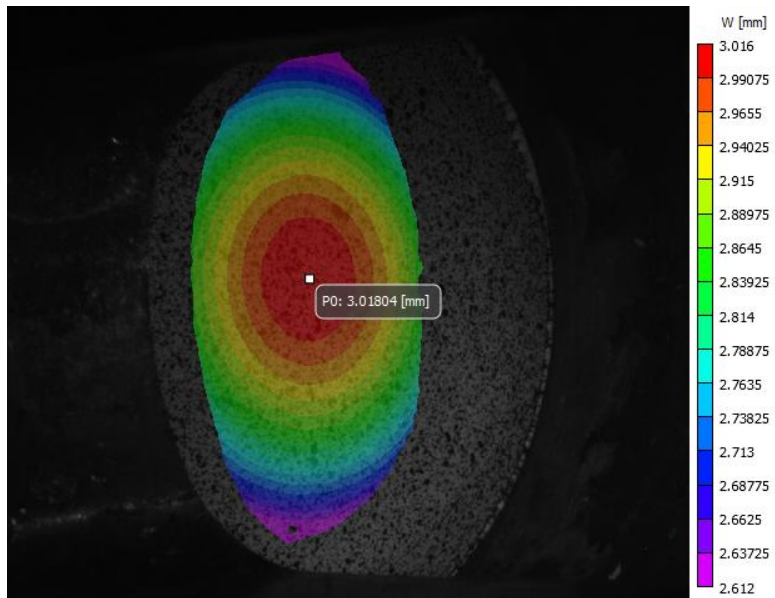


Figure E- 38. M3-TMP1-P4-SR6-T1-N1 with displacement

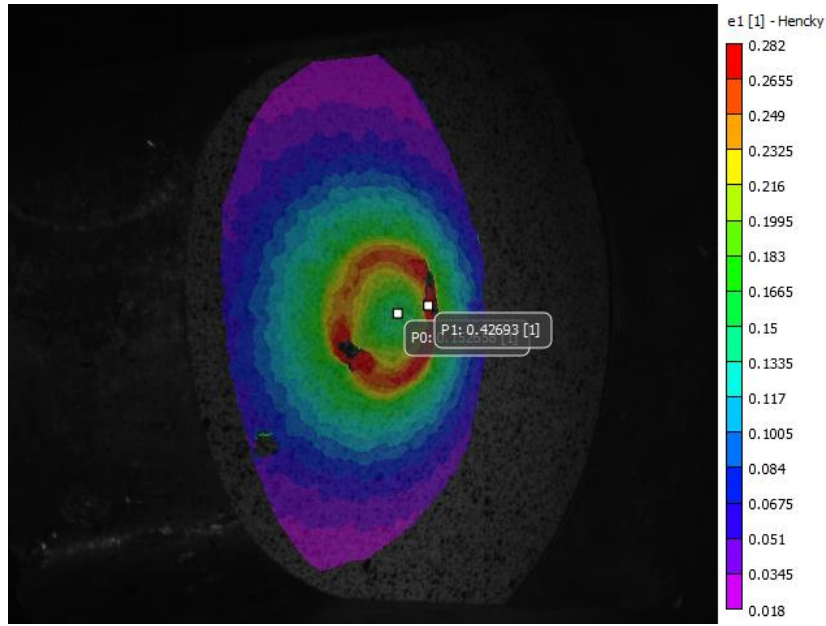


Figure E- 39. M3-TMP4-P4-SR6-T1-N5 ϵ_1

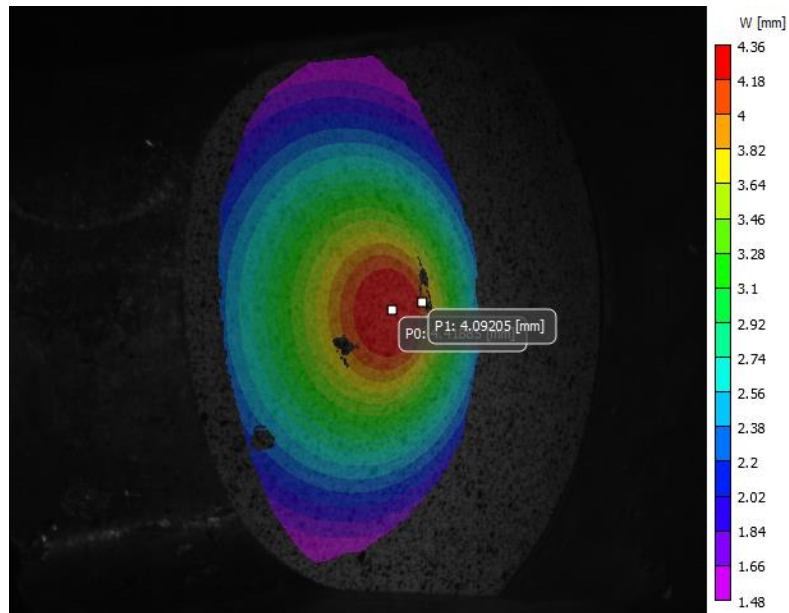


Figure E- 40. M3-TMP4-P4-SR6-T1-N5 with displacement

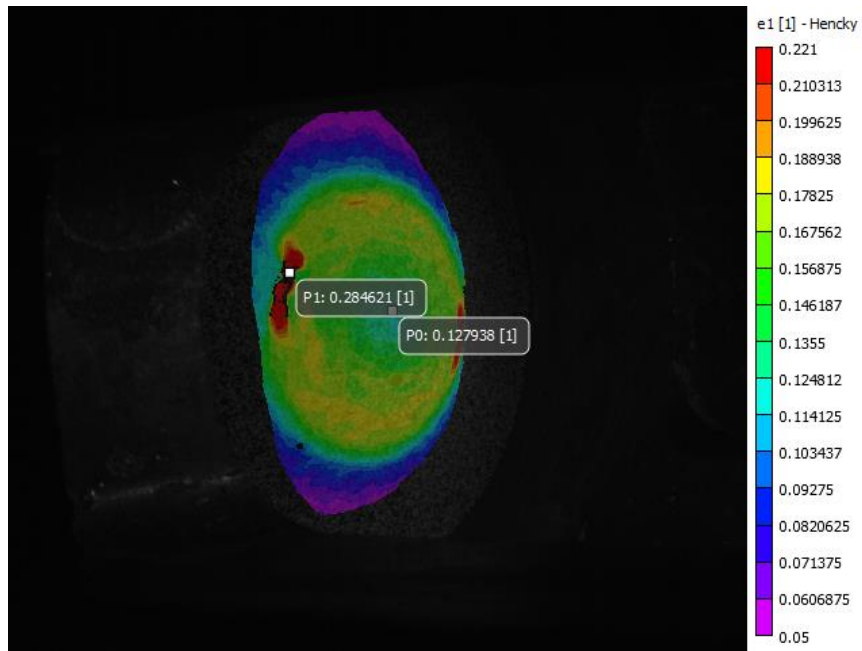


Figure E- 41. M3-TMP6-P4-SR6-T1-N3 ϵ_1

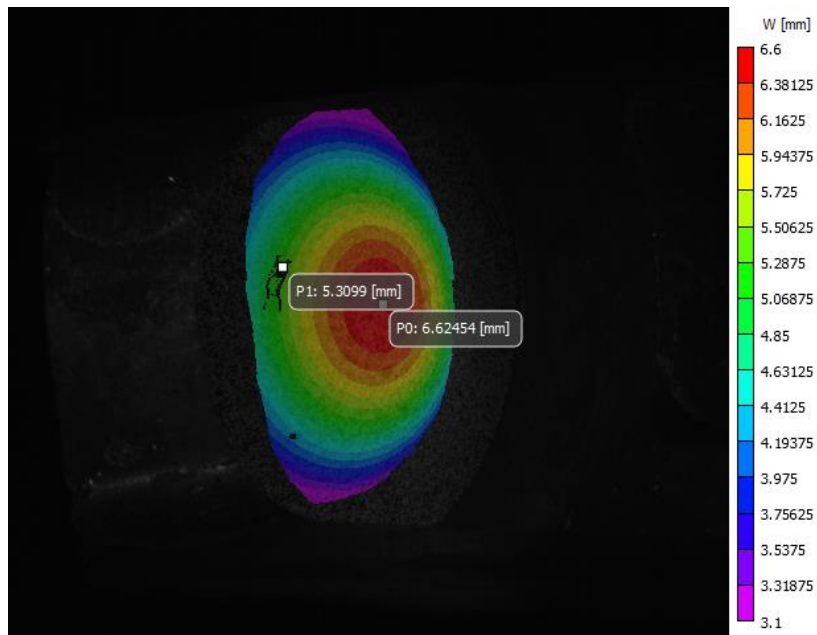


Figure E- 42. M3-TMP6-P4-SR6-T1-N3 with displacement